Fermi level engineering of solution-processed amorphous ultra-wide bandgap semiconductor towards transparent thin-film transistors

(透明薄膜トランジスタに向けた溶液プロセスアモルファスウルトラワイドバンドギャップ半導体のフェルミ準位エンジニアリング)

August 2022

DIKI PURNAWATI

Division of Materials Science
Graduate School of Science and Technology
Nara Institute of Science and Technology

To The Almighty, Allah SWT

Abstract

In the 5.0 society era where human and electronics has become indivisible component, technological breakthroughs for enabling future electronic devices are unceasingly demanding for innovation. In line with innovation, the future electronic trends require highly transparent, cost-effective, large-area scalability, and harsh-environment-resistant material. With the recent paradigm shift from wide bandgap (E_g > 3.0 eV) into ultra-wide bandgap material (E_g > 4.0 eV), ultra-wide bandgap materials become a promising candidate for future technologies. However, the challenge is to improve the performance of those materials to be suitable with the current advance technology.

Thin-film transistors (TFTs) are considered a basic building block of the current electronic devices. To realize the future electronic trend, ultra-wide bandgap material TFT, such as amorphous Gallium Oxide (a-Ga_2O_x) TFT is gaining a huge research interest for the past few years. In particular, solution-processed a-Ga_2O_x has been attracting great attention due to large-scale production, high breakdown voltage, device design flexibility, and excellent optical quality (E_g > 4.8 eV). Nonetheless, obtaining electrical conduction on as-deposited solution-processed a-Ga_2O_x is quite challenging. This is mainly cause by numerous impurities-related issues of solution deposition technique, and the combination of ultra-wide bandgap and an amorphous structure which hinder electron mobility. Therefore, developing semiconducting solution-processed a-Ga_2O_x will be a superb research achievement. In this dissertation, Fermi level engineering of ultra-wide bandgap amorphous oxide semiconductor (UWB-AOS) film is proposed by modifying the a-Ga_2O_x film properties. The first demonstration on utilization of solution-processed a-Ga_2O_x for TFT device via experimental and machine learning approach will be elucidated.

Chapter 1 provide a brief introduction on the fundamentals of TFTs, ultra-wide bandgap material trends, and specifically oxide material used in this work. The advanced material design method for accelerating material design and device fabrication was also introduced.

Chapter 2 starts with an overview of other report strategies for material properties modification of oxide TFTs. To achieve semiconducting behavior of solution-processed a-Ga_2O_x, the strategy is to shift the Fermi level position closer to the conduction band. By utilizing Fermi level engineering, insulating a-Ga_2O_x has been successfully conversed into its semiconducting state. Fermi level engineering is a technique for material design which rely on

the Fermi level shifting phenomena. For n-type semiconductor such as a-Ga_2O_x, the E_F shifting phenomenon implies an increase in the electron carrier concentration which further improve the film conductivity and the TFT device as well. By varying experimental condition including: annealing ambient gases and temperature, E_F-CBM distances were minimized. Interestingly, semiconducting a-Ga_2O_x were successfully obtained as shown by TFT switching behavior (μ_{sat} = 10^{-2} cm^2/Vs) which was achieved by performing annealing under 4% hydrogen ambient. E_F estimation via UV-Visible spectra and XPS reveal the Fermi level shifting phenomena which is mainly affected by the hydrogen doping. Secondary ion mass spectrometry confirmed the H-incorporation which further act as a shallow donor. The H-incorporated occupy donor state near conduction band and contributed excess electron carrier concentration which represent as an increase in the carrier density by 1 order magnitude.

Chapter 3 starts with a critical point of solution deposition technique and current strategies to address those issues. To achieve semiconducting behavior of as-deposited a-Ga_2O_x, the strategy is by controlling the precursor aging time and relative humidity during film deposition. It was found the device performance was deteriorated as the precursor aging time increased. The optimum precursor aging for as-deposited a-Ga_2O_x film is 0 week. Furthermore, by monitoring and controlling relative humidity during thin film deposition, decent performance of as-deposited a-Ga_2O_x TFTs were achieved (μ_{sat} = 10^{-2} cm^2/Vs). Aside from the water vapor, the result also showed that the hydrogen annealing tends to enhance the device performances in selected cases. Finally, the result showed that hydrogen doping which drive the electron doping, might have originated from either hydrogen annealing or water vapor (humidity). Those hydrogen doping are vital factors to achieve the semiconducting behavior of as-deposited a-Ga_2O_x TFTs.

Chapter 4 highlights the utilization of machine learning as an optimization method for accelerating material design and device fabrication. In particular, how this method is beneficial for developing novel materials with limited literature such as solution-processed a-Ga_2O_x. The strategy is by utilizing machine learning as an approach for predicting Fermi level of solution-processed a-Ga_2O_x. By using regression models, experimental data was used as an input to further train the algorithm. An excellent Fermi level prediction of 87% accuracy by Machine Learning method has been successfully achieved. Machine learning can easily identify optimized fabrication parameters to achieve the minimum Fermi level value. For instance, Fermi level value of 1.36 eV can be obtained by depositing 90 nm film at 425°C under 4% H_2 annealing. These approaches for estimating and predicting Fermi level of solution-processed ultra-wide bandgap semiconductors will be valuable and powerful in accelerating material design and device

fabrication. Moreover, it will be beneficial for rapid and cost-effective optimization of UWB material design for future electronic applications.

The dissertation is concluded in Chapter 5 by summarizing the findings and providing suggestion for future studies.

List of Abbreviations

Abbreviation	Description
β-Ga_2O_3	Crystalline Gallium Oxide at beta phase
μ_{sat}	Field-effect mobility in saturation region
ρ	Film density
a-IGZO	Amorphous InGaZnO
a-IZO	Amorphous InZnO
a-Ga_2O_x	Amorphous Gallium Oxide
c-Ga_2O_x	Crystalline Gallium Oxide
AOS	Amorphous oxide semiconductors
CBM	Conduction band minimum
C_{ox}	Gate insulator capacitance
E_u	Urbach energy
E_g	Optical bandgap energy
E_F	Fermi level energy
g_m	Transconductance
GI – XRD	Grazing incidence X-ray diffraction
I_{ds}	Drain current
I_{off}	Off-current
I_{on}	On-current
I_{on}/I_{off}	Current On/Off ratio
L	Channel length
Poly-Ga_2O_3	Polycrystalline Gallium Oxide
S/D	Source/drain electrode
SIMS	Secondary ion mass spectroscopy
SPM	Sulfuric-peroxide mixture
SS	Subthreshold swing
T	Optical transmittance
TFT	Thin-film transistor
UWB – AOS	Ultra-wide bandgap amorphous oxide semiconductor

VBM	Valence band maximum
V_{ds}	Drain voltage
V_{gs}	Gate voltage
V_{th}	Threshold voltage
W	Channel widts
WB – AOS	Wide bandgap amorphous oxide semiconductor
XPS	X-ray photoelectron spectroscopy
XRD	X-ray diffraction

Contents

Abstract ii

List of Abbreviations v

Contents vii

Chapter 1 Introduction 1

1.1 Background 1

1.2 Thin-film transistors (TFTs) 1

1.2.1.1 Basic principle of TFTs 1

1.2.1.2 Amorphous oxide TFTs 4

1.3 Paradigm shift from wide bandgap (WB) to ultra-wide bandgap (UWB) devices 5

1.4 Amorphous ultra-wide bandgap (UWB) materials 7

1.5 Deposition process for TFTs 9

1.6 Fermi level engineering 11

1.7 Objective and research outline 12

1.8 References 15

Chapter 2 Insulator-to-Semiconductor conversion of solution-processed UWB a-Ga2Ox film via Fermi level engineering 21

2.1 Introduction 21

2.2 Insulator-to-semiconductor conversion methods 22

2.3 Hydrogen-doping principles and challenges 24

2.3.1 Hydrogen-doping methods 25

2.3.2 Hydrogen annealing 28

2.3.3 Fabrication process of hydrogen-annealed solution-processed ultra-wide bandgap a-Ga_2O_x TFTs 30

2.4 Achievement of semiconducting a-Ga_2O_x TFTs via hydrogen annealing 33
2.4.1 Film characteristics 34
2.4.2 TFT characteristics 36
2.5 The effect of annealing ambient gases to the a-Ga_2O_x film characteristics 38
2.5.1 Thin film deposition and sample preparation 38
2.5.2 Film characteristics 39
2.6 a-Ga_2O_x TFTs performance under different annealing ambient gases 46
2.6.1 Device fabrication 46
2.6.2 TFT characteristics 47
2.7 Mechanism on the electrical characteristic improvement of a-Ga_2O_x TFTs 49
2.7.1 H-doping mechanism 50
2.7.2 E_F shifting phenomena 50
2.8 Summary 51
2.9 References 52

Chapter 3 Study of humidity dependence on solution-processed UWB a-Ga_2O_x films .. 56
3.1 Introduction 56
3.2 Critical point of solution deposition technique 57
3.3 Evaluation of precursor aging on the a-Ga_2O_x Films 60
3.4 Achievement of semiconducting behavior of as-deposited a-Ga_2O_x TFTs in controlled RH 65
3.5 Evaluation of dry and wet humidity on the a-Ga_2O_x TFTs 67
3.6 Proposed mechanism on the electrical characteristic improvement of a-Ga_2O_x TFTs.. 73
3.7 Summary 74
3.8 References 75

Chapter 4 Analysis of Machine learning for Fermi level engineering 78
4.1 Introduction 78

4.2 Recent progress of machine learning approach in materials science 81
4.3 Fermi level estimation methods 83
4.3.1 Experimental approaches 83
4.3.2 Machine learning approaches 85
4.4 Machine learning regression models 87
4.5 Machine learning for Fermi level prediction of a-Ga_2O_x film. 88
4.5.1 Sample preparation 88
4.5.2 Materials characterization 90
4.5.3 Experimental result 91
4.5.4 Data set pre-processing 95
4.5.5 Machine learning pipeline 96
4.5.6 Experimental cross-validation 100
4.6 Summary 101
4.7 References 103

Chapter 5 Summary 107
5.1 Conclusions 107
5.2 Suggestions for future work 108

Research Achievements 110
List of Publication 110
Research Grant 111
Presented Works 111
Acknowledgements 112

Chapter 1 Introduction

1.1 Background

Human society has been actively growing from society 1.0 (hunting society), 2.0 (agricultural society), 3.0 (industrial society), 4.0 (information society), and recently faces the new era of society 5.0 (super smart society). In general, society 5.0 is a human-centered society which relies on a system that highly integrates cyberspace and physical space. In consequence, human and electronics have become indivisible components of society. Recent electronics technology allows us to get connected to people around the world. A huge transformation of the way people connect is marked by a pandemic breakout in early 2020. Thereupon, the market demand for technology innovation that allows human-electronic interfaces in such an easy, safe, and convenient way for the long term is needed.

Technological breakthroughs have pushed the boundaries of technology by enabling electronic devices which are smaller, thinner, and even lighter with a simpler appearance such as foldable, rollable, and wearable as well. Those technologies are used for multiple purposes including entertainment, life-assistant, work-assistant, and even for space exploration [1]. The future generation of electronic technologies requires large-scale production using highly transparent, cost-effective, and harsh-environment-resistant materials by utilizing ultra-wide bandgap material. To realize such devices, innovation of material exploration and engineering is highly demanded. The challenges, however, is to improve the performance of those material to be suitable with the current advance technology.

1.2 Thin-film transistors (TFTs)

1.2.1.1 Basic principle of TFTs

Thin-film transistors (TFTs) are switching elements which basically constructed by the MOSFET transistors. It consists of three terminals and are used for electrical switching or signal amplification [2]. TFT technology has been widely used in flat-panel displays, personal computers, smartphones, and personal digital assistants. Alongside that, its application on a

diverse area has been investigated such as X-ray detection [3], ultra-violet photodetectors [4][5], chemical sensing [6], and bio-chemical sensing [7].

As shown in ***Figure 1.1***, a basic TFT structure is composed of semiconductor channel, gate insulator, and metallic gate/source/drain electrodes. Specifically, the semiconductor channel is an active layer where the charge carriers are accumulated and laterally transported. Gate insulator acts to manipulate the conductance of the channel while ensuring electrical insulation to minimize a leakage current. Source/drain electrodes acts to inject or extract charge carriers from external sources. While the gate electrode acts to modulate the source-to-drain charge conduction. By applying a positive gate voltage (V_G > 0V), the gate insulator became electrostatically polarized. Thereupon, electron carriers in semiconductor channel are accumulated at the interface and laterally transported from source to drain.

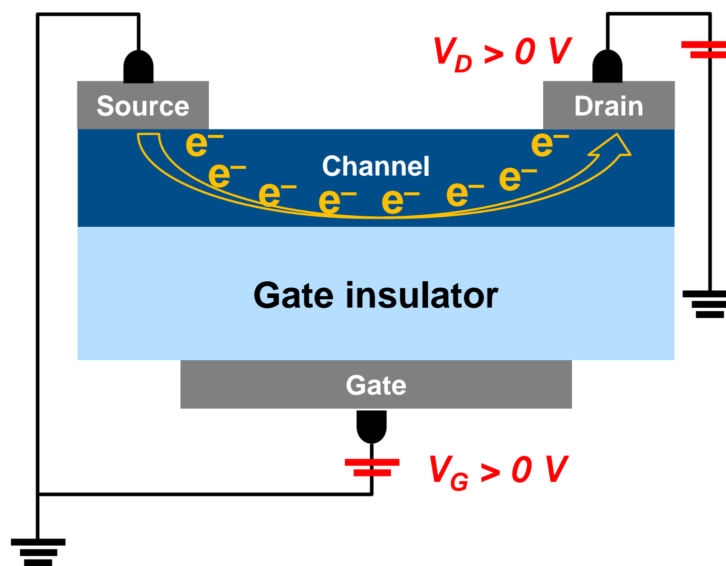

Figure 1.1. Schematic of *n*-type TFT operation.

TFT device performance is evaluated by specific parameters that are extracted from the output and transfer characteristics as represented in ***Figure 1.2***. The on-current is an important parameter which is highly dependent to the device geometry (channel thickness t_c, width W, and length L), gate insulator material selection, and applied voltage [8]. Thus, it is normalized into field-effect mobility (μ) based on the gradual channel approximation [9]. Furthermore, the linear regime as shown in ***Figure 1.2***a represented as a region where the carrier density is

uniform ($V_{ds} < V_{gs} - V_{th}$). In this specific case, the drain current is represented by the following equation:

$$I_{ds,lin} = \frac{W}{L}\mu_{lin}C_{ox}\left\{\left(V_{gs} - V_{th}\right) - \frac{V_{ds}}{2}\right\}V_{ds} \quad \textbf{(1.1)}$$

where $I_{ds,lin}$ is drain current in linear region, μ_{lin} is linear mobility, C_{ox} is the gate insulator capacitance per unit area, V_{gs} is gate voltage, V_{th} is V_{gs} at I_{ds}= 1 pA (in this work) , and V_{ds} is drain voltage. The μ_{lin} obtained from the following equation:

$$\mu_{lin} = g_m \frac{L}{WC_{ox}V_{ds}} \quad \textbf{(1.2)}$$

where g_m is transconductance. Otherwise, when $V_{ds} \geq V_{gs} - V_{th}$, the TFT device operates in saturation regime. Therefore, the drain current is represented by the following equation:

$$I_{ds,sat} = \frac{W}{2L}\mu_{sat}C_{ox}\left(V_{gs} - V_{th}\right)^2 \quad \textbf{(1.3)}$$

and the μ_{sat} represented by the equation:

$$\mu_{sat} = \frac{g_m^2}{2\frac{W}{L}C_{ox}I_{ds}} \quad \textbf{(1.4)}$$

Both mobility (μ_{lin} and μ_{sat}) correspond to the charge carrier transport efficiency which directly affects the maximum drain current. The main difference for both mobility (μ) is that it either describes the μ in the linear regime or saturation region. In this case, linear regime is obtained when the $V_{ds} = 0.1\ V$. While saturation regime is obtained when $V_{ds} = 5.0\ V$. Both values are calculated for each TFT. Nonetheless, in most cases in this study, only the saturation regime will be reposted.

Other than those parameters, current on/off ratio (I_{on}/I_{off}), and subthreshold swing (*SS*) are also evaluated. The I_{on}/I_{off} is obtained by dividing the maximum drain current with the minimum drain current in saturation regime. Whereas *SS* corresponds to how fast the TFT device switches between its ON and OFF states. Its value is related to the trap density [8]. The *SS* value is represented by the following equation:

$$SS = \frac{dV_{gs}}{dlog_{10}I_{ds}} \quad \textbf{(1.5)}$$

With respect to the device performance, the μ and I_{on}/I_{off} values are targeted as high as possible, V_{th} is targeted to be as close as 0 V, while the SS is targeted as low as possible. Those

parameter values are necessary to reduce the operating voltage and minimize the power consumption [10].

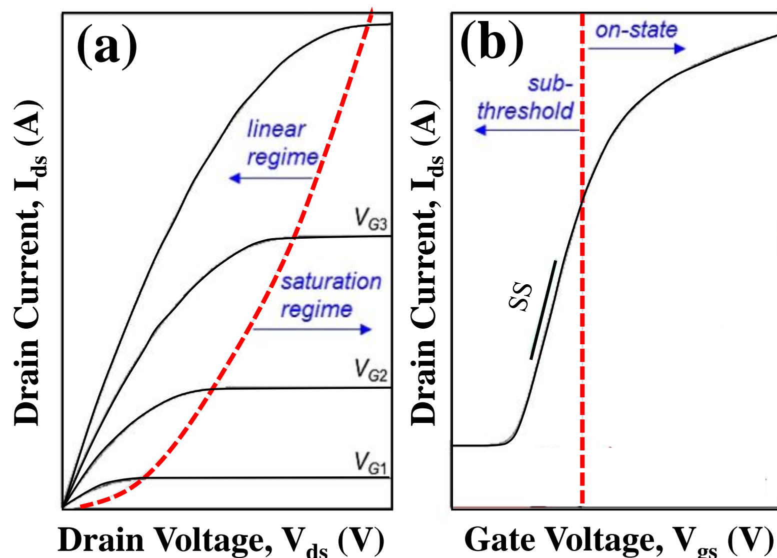

Figure 1.2. (a) Output and (b) transfer characteristics of an *n*-type TFT [2].

In this study, the equations above will used to evaluate the TFT device performance. The saturation mobility will be reported instead of linear mobility. Likewise, the ON voltage was defined at 1 pA since this device still has relatively poor performance. Moreover, the absolute value of drain current was used in producing the transfer curve. Despite the poor performance, this research is promising since it is the first demonstration on obtaining semiconducting behavior of solution-processed ultra-wide bandgap a-Ga_2O_x.

1.2.1.2 Amorphous oxide TFTs

Oxide semiconductor was first proposed as channel materials for TFT devices in 1964 using SnO_2 and In_2O_3 [11]. However, there was no significant progress on the oxide material-based TFT after this report. Later in 2004, Hosono *et al.* demonstrated high-performance amorphous InGaZnO (a-IGZO) TFT which was fabricated at room temperature [12]. This report, in any case, marked the regaining of the research interest in oxide material-based TFTs. Thereafter, a-IGZO TFT have been massively researched for various application including flat-panel displays [13][14], integrated circuits [15][16], and sensors [17][18]. In particular, a-IGZO

offers numerous attractive features which are better than amorphous silicon (a-Si) and low-temperature polysilicon (LTPS) as summarized in ***Table 1-1***.

For the past decade, a-IGZO became a rising star because it offers excellent uniformity, fabrication process simplicity, large-area scalability, and compatibility with various deposition technique. Moreover, it exhibits superior device performance with $\mu \geq 10$ cm^2/Vs. Furthermore, a-IGZO, and most of amorphous oxide semiconductor (AOS) materials, typically offer high optical transparency in the visible region (400 – 800 nm) which is promising for the realization of future generation flexible and transparent devices.

Table 1-1. Summary of the comparison between a-Si, LTPS, and a-IGZO [8].

	a-Si:H	**Poly-Si**	**a-IGZO**
Mobility (cm^2/Vs)	< 1	30 – 100	10 – 100
Uniformity	Good	Poor	Good
Cost/Yield	Low/High	High/Low	Low/High
Light stability	Poor	Good	> a-Si
Printable	No	Yes	Yes
Pixel circuit for OLED	Complex	Complex	Complex
Process cost	Low	High	Low

1.3 Paradigm shift from wide bandgap (WB) to ultra-wide bandgap (UWB) devices

In 1946, the first demonstration of the Ge- and Si-based transistor marked the beginning of semiconductor technologies. Shortly thereafter, for 40 years, semiconductor technology was dominated by Ge, Si and III-Vs materials [19]. From that time, semiconductor material was integrated into various electronic devices which are discrete, bulky, inefficient, and slow-turn-on. Until the late 1980s, semiconductor technology was limited to those materials which have relatively low bandgap of E_g~2.3 eV. Researchers realized that wider bandgap material has a high potential of higher breakdown voltage and excellent optical quality which are mainly required for advanced electronic devices. Nonetheless, despite their obvious potential, developing wider bandgap semiconductor is extremely challenging.

An essential material breakthrough was made by Prof. Akasaki, Amano, and Nakamura (AAN) which were awarded the 2014 Nobel Prize in Physics [20][21]. AAN made three

essential breakthroughs in the late 1980s and early 1990s: (a) “apparently magic” AlN and GaN buffer layers on sapphire can dramatically reducing the dislocation densities, (b) an excellent method to activate p-type Mg doping of GaN, and (c) a remarkable resistance of InGaN quantum well luminescence to defects. Since then, InGaN-based optoelectronics has been driving the development of wide bandgap (WB) semiconductor materials [22].

Shortly, for the past few decades, huge progress was achieved by WB semiconductor materials such as SiC and GaN. Both WB semiconductor materials are maturing rapidly with a significant market growth of ~US$210M per year in 2015[22]. It has been established for power electronic applications in hybrid and electric vehicles, photovoltaic inverters, and power supplies [22].

Table 1-2. Comparison of WB and UWB material properties.

	WB		**UWB**		
	GaN	**4H-SiC**	**AlN**	**β-Ga_2O_3**	**Diamond**
Bandgap (eV)	3.4	3.3	Up to 6.0	4.85	5.5
Thermal conductivity (W/mK)	253	370	up to 319	11-37	Up to 3450
p-type dopability	Good	Good	Poor	Poor	Good
n-type dopability	Good	Good	Moderate	Good	Moderate
Solution deposition compatibility	No	No	Yes	Yes	No

To date, the future generation of electronics demands advanced technology which is transparent, cost-effective, large-scale production, and harsh-environment-resistant for a wider application range. In order to realize such technology, tremendous research interest has shifted from wide bandgap materials (E_g > 3.0 eV) to ultra-wide bandgap materials (E_g > 4.0 eV). Ultra-wide bandgap (UWB) material is becoming a competitive candidate due to its unique features which enables great potential for high breakdown voltage, high thermal stability, and large-area scalability. Despite of its high potential, UWB semiconductor materials such as β-Ga_2O_3, AlGaN/AlN, and diamond are immature. Although there has been intensive research on those materials for the past two decades, the demonstration of UWB-based devices is totally immature. In addition, there is only a small number of laboratories around the world that has been established for the development of UWB-based devices. Thus, UWB materials currently find themselves at a stage of development, similar to WB materials in the 1980s. For the next

few decades, researchers will confidently make a breakthrough for UWB-based devices for wider applications such as space exploration.

Table 1-2 summarized the comparison of the recent WB and UWB material properties. Among other UWB materials, β-Ga_2O_3 is the newest and least mature material. Nonetheless, it became one of the most intriguing and fascinating material due to: (1) its unique fundamental material properties, (2) affordable native substrates, (3) a prospective candidate for transistor devices [22]. β-Ga_2O_3 has excellent transparency in deep ultra-violet (DUV) region which makes it prospective for solar-blind DUV photodetectors, flame detectors, high-temperature signal processing, harsh-environment electronics, and wireless communication devices [22].

1.4 Amorphous ultra-wide bandgap (UWB) materials

Gallium oxide (Ga_2O_3) is a direct ultra-wide bandgap (UWB) semiconductor material with seven phases (α, β, γ, δ, ε, polycrystalline, and amorphous) [23]. In particular, β-Ga_2O_3 has become promising material for solar-blind photodetectors, optoelectronic devices, photovoltaics, sensors, magneto electronics, flame detectors, harsh-environment electronics, and ozone layer monitoring [22][24][25][26]. Nevertheless, the β-Ga_2O_3 fabrication process is expensive and complicated as compared with the amorphous one [26]. In addition, among seven phases of Ga_2O_3, amorphous gallium oxide (a-Ga_2O_x) is the most promising material for large scale production [23]. In contrast with β-Ga_2O_3 which is highly transparent in DUV region, the a-Ga_2O_x has excellent transparency not only in DUV region, but all over UV, visible, and NIR region [23]. This appealing fact makes a-Ga_2O_x become a promising candidate material for future transparent devices which are highly flexible on device design.

In general, the properties of crystalline materials with minimum defects are superior compared to their amorphous counterparts. Nonetheless, things have changed since the emergence of a-IGZO as the new future of flexible high-performance TFT devices [12]. Thereafter, transparent amorphous oxide semiconductor (TAOS) have been extensively investigated and now used for commercial large-area flat-panel displays [8]. With respect to a-IGZO material, Ga element is a stabilizer component in amorphous structure since it will not crystallize unless the substrate temperature is high enough. While InO and ZnO tend to crystallize readily even at low temperature (room temperature) [27]. It indicates the flexibility of amorphous gallium oxide (a-Ga_2O_x) material modification and exploration as compared to a-InO and a-ZnO.

At the moment, a-Ga_2O_x has attracted a great attention as evident by the increased number of publications related to a-Ga_2O_x for the past decade (***Figure 1.3***). The a-Ga_2O_x is regarded as one of the most promising material for future electronic applications due to its ultra-wide bandgap (E_g > 4.8 eV), high breakdown field strength, device design flexibility, harsh-environment resistance, cost-effectiveness, and large-area scalability [28][29][1][30][29]. Currently, it has been widely used as thin-film transistors, solar blind ultra-violet photodetectors, and sensors, flame detection and missile warning [29][30][5][4][31][5]. Particularly, in ultra-violet photodetector applications, the a-Ga_2O_x have been reported to exhibit decent performance which is comparable with or even better than crystalline gallium oxide [29]. The contrast of crystalline and amorphous gallium oxide is summarized in ***Table 1-3***. With those excellent properties, a-Ga_2O_x is become promising candidate future devices which are highly transparent, large-scale, harsh environment-resistant, and more importantly it is cost-effective.

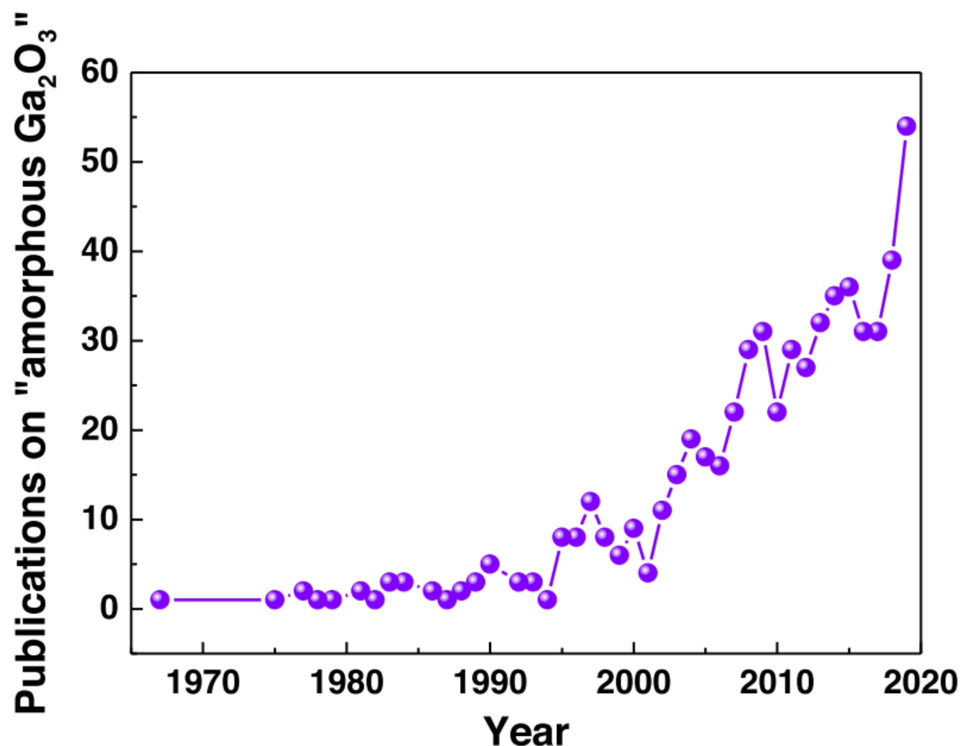

Figure 1.3. Number of publications related to a-Ga_2O_x from 1967 to the end of 2019 [29].

The challenges, however, is a-Ga_2O_x-based devices mainly exhibit poor device performance particularly solution-deposited a-Ga_2O_x [26][30]. Obtaining the electrical

conduction is quite challenging caused by a complex combination of ultra-wide bandgap and an amorphous structure which hinder electron mobility. Thus, numerous attempts to improve a-Ga_2O_x electrical properties have been demonstrated [30][31]. Later, UWB a-Ga_2O_x material development and enhancement will be continuously explored.

Table 1-3. Comparison of crystalline and amorphous Gallium Oxide.

	β-Ga_2O_3	**a-Ga_2O_x**
Bandgap (eV)	4.6 – 4.9 [28]	4.1 – 5.1 [31][28][32]
Spectral range	Deep UV	UV-VIS-NIR
Breakdown voltage	High	High
Fabrication cost	High	Low
Harsh-environment-resistant	Yes	Yes
Large-area scalability	Moderate	High

1.5 Deposition process for TFTs

With the immense application of TFT devices in the current 5.0 society, the TFT fabrication method which encourages cost-effective and large-scale production is indispensable to be economically efficient. TFT deposition method has two main categories: vacuum deposition technique, and solution deposition technique. Vacuum deposition technique has been widely used for deposition method of numerous oxide material including IGZO [27][33][34], InSnZnO [35], β-Ga_2O_3 [36], a-Ga2Ox [31], and countless oxide materials.

Particularly, in TFT device applications, the vacuum-deposited TFT exhibits unquestionably high-quality film and excellent TFT performance. Nevertheless, it is mainly struggling with serious issues of its high cost and energy requirement, experiment complexity, and difficulty in scaling to large-area electronic devices [31][37][38]. For the past decade, the solution deposition technique has become more popular and attractive as an alternative deposition method for oxide-based TFT channels evidence by the increased number of publications related to solution-processed oxide TFTs for the past decade (***Figure 1.4***). Since then, the solution process has become the superior alternative method due to large-area fabrication, equipment simplicity, atmospheric processing, and low cost [37][38]. In selected cases, solution-deposited TFT exhibit comparable device performance as summarized in ***Table 1-4***.

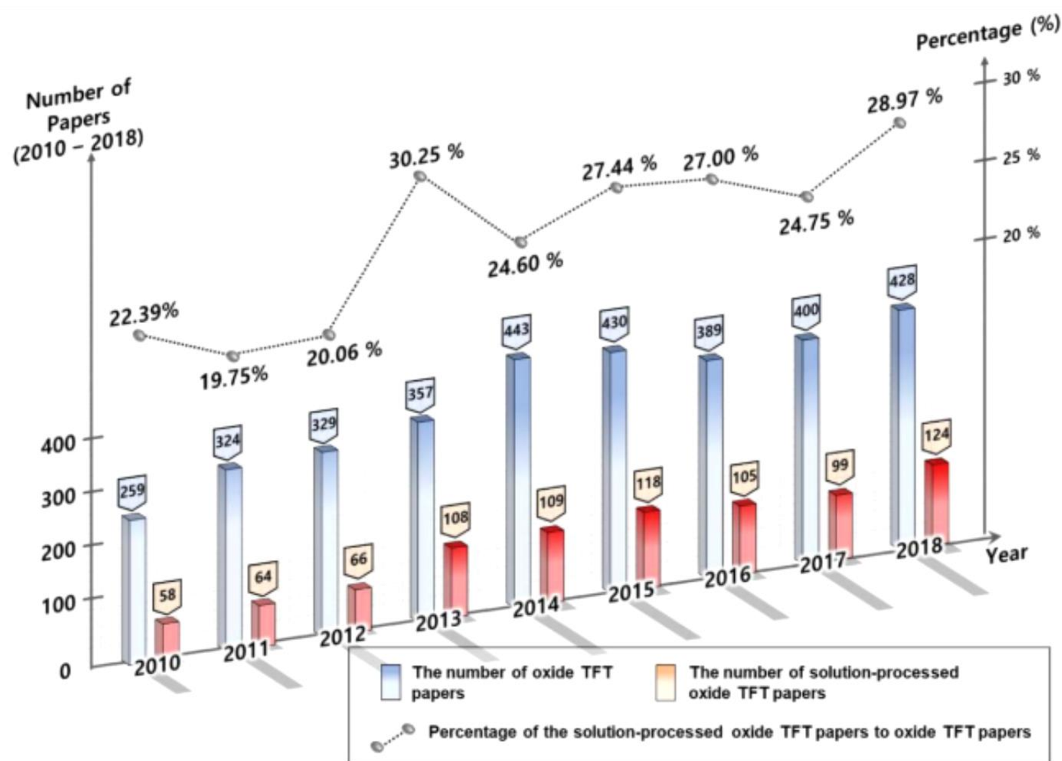

Figure 1.4. Number of publications related to oxide TFTs and solution-processed oxide TFTs from 2010 to 2018 [39].

Table 1-4. Comparison of solution-deposited TFTs vs vacuum-deposited TFTs.

Channel material	Mobility (cm^2/Vs)	On/Off ratio	V_{th} (V)	Deposition process	Reference
Li:ZnO	85.0	~10^6	< 6	Spray pyrolysis	[40]
IGZO	7.65	~10^6	-	Spin coating	[41]
IGZO	20.9	~10^7	-	DC sputtering	[42]
a-Ga_2O_x	1.5	> 10^7	-	PLD	[31]
a-Ga_2O_x	0.04	~10^7	5	RF sputtering	[5]
a-Ga_2O_x	0.01	~10^4	1.7	Spin coating	[30]

Nevertheless, in most cases, solution-deposited TFT performance is inferior to that the vacuum-deposited counterpart. An extensive effort to improve the performance of solution-deposited TFT in the past few years. Yet, solution deposition technique is still struggling with those issues. Another thing is, the solution deposition technique has severe impurities-related

issues which might be attributed to the precursor-related impurity or environment related impurity. Additionally, there still numerous unsolved issues for solution-deposited a-Ga_2O_x, not only how to improve its initial characteristics, but deep investigation of its stability is also expected. As of now, there is still limited report on solution-deposited a-Ga_2O_x-based device [26][30] which apparently open a wider opportunity for future exploration. Finally, by encouraging a-Ga_2O_x material exploration, future devices which are transparent, wearable, cost-effective, and harsh-environment-resistant will closely to achieved.

1.6 Fermi level engineering

Fermi level engineering is a technical term which refers to material design technique based on the Fermi level shifting phenomena. As mentioned in the past few sections, despite of its excellent potential for future devices, solution-deposited a-Ga_2O_x is an immature material which is widely open for material modification and exploration. In general, there are three main drawback of solution-deposited a-Ga_2O_x: (a) it has inferior electrical properties owing to insufficient electron carrier concentration, (b) p-type doping is extremely challenging which prevented its application to bipolar devices such as light emitters, (c) there is only limited information available regarding solution-deposited a-Ga_2O_x since this material is still continuously developing. Thus, to overcome those issues, innovation in material design technique is required.

In general, for *n*-type semiconductor (a-Ga_2O_x), excess electron carrier concentration is represented as fermi level (E_F) position relatively close to the conduction band minimum (CBM). The minimum E_F-CBM distance is imperative to enhance the electrical properties which further exhibit better device performance. Therefore, the main idea of Fermi level engineering is to modify the E_F-CBM distance. This method, however, is still quite challenging because of limited literature has been reported the Fermi level engineering, particularly in gallium oxide material (***Table 1-5***). As the comparison, E_F value of wide bandgap materials such as c-IGO and a-IGZO were also included. In particular, for β-Ga_2O_3, considerable optoelectronic devices was successfully obtained at E_F value of 1.92 – 2.07 eV [44]. Apparently, for ultra-wide bandgap material, the E_F value of ~2.0 eV is close enough to utilize this material as an electronic device. Nonetheless, this value is still relatively far compared to the wide bandgap materials such as c-IGO and a-IGZO. Generally, ultra-wide bandgap nature hinder the electron conduction which implies on the low electron carrier concentration [31] and reflected

as E_F relatively far from the CBM. Therefore, by considering several reasons that mentioned above, this study targeted the E_F value to be as close as ~0.4 eV to the CBM.

To achieve the targeted E_F value, Fermi level engineering to optimize the E_F position is required. By obtaining EF value close to the CBM, I expect to obtain excellent semiconducting solution-processed a-Ga_2O_x film. Nonetheless, in most cases, experimental optimization is time-consuming and it is required material intensive usage. Thus, advanced method of Fermi level engineering by combining material engineer and data scientist perspectives is required.

Table 1-5. Summary of reported work of E_F-CBM distance of oxide materials.

Material	Deposition process	Optical bandgap (E_g, eV)	E_F-CBM distance (eV)	Reference
c-IGO	ALD	3.63	0.05	[45]
a-IGZO	Sputter	3.01 – 3.03	0.39 – 1.09	[43]
β-Ga_2O_3	PECVD	4.40 – 5.10	1.92 – 2.07	[44]
β-Ga_2O_3	PLD	4.91 – 5.12	2.27 – 2.56	[46]
β-Ga_2O_3	PLD	4.12 – 4.90	1.12 – 2.13	[47]
β-Ga_2O_3	PLD	4.48 – 4.72	0.44 – 0.85	[36]
a-Ga_2O_x	Spin coating	4.22 – 4.80	1.18 – 1.72	[30]

1.7 Objective and research outline

In the 5.0 society era where human and electronics has become an unseparated component, technological breakthroughs and development for enabling future electronic devices are unceasingly demanding for innovation. Along with the innovation, proposed material and method explorations must be in line with the future electronic device trends, which are highly transparent, cost-effective, large-area scalable, and harsh-environment-resistant. With the recent paradigm shift from wide bandgap into ultra-wide bandgap material for advanced technologies application. With those in mind, the objectives of this dissertation are conceptualized:

a) Develop a semiconducting solution-processed hydrogenated ultra-wide bandgap amorphous Gallium Oxide.

Amorphous Gallium Oxide has unique fundamental properties which highly prospective for realizing advanced technology for future electronic trends. However, UWB-based devices are not yet established. Innovation in material development particularly electrical properties enhancement will further open the horizon of future development and application.

b) *Understand the role of humidity to develop a semiconducting solution-processed as-deposited ultra-wide bandgap amorphous Gallium Oxide.*

Solution deposition technique is struggles with solution-related issues such as precursor aging and water vapor (humidity). In most cases, solution-deposited film has a high sensitivity to its environment condition during film deposition. Understanding the role of humidity not only brings a comprehensive knowledge of solution-deposited a-Ga_2O_x, but also slightly improve the film quality and TFT performance as well.

c) *Develop a material design method for rapid and cost-effective material design*

Developing an immature material is not only challenging, but it is time consuming and expensive because it requires an intensive material resource. An optimization method to cut-off the experiment steps will significantly accelerate material design and device fabrication.

Achieving these objectives will greatly aid in the development of future transparent, wearable, and harsh-environment-resistant application for a-Ga_2O_x. In particular, this would be the first demonstration on utilization of solution-processed a-Ga_2O_x for TFT device application. This dissertation comprises five chapters. Chapter 1 provide a brief introduction on the fundamentals of TFTs, ultra-wide bandgap material trends, and specifically oxide material used in this work. The advanced material design method for accelerating material design and device fabrication was also introduced.

Chapter 2 starts with an overview of other report strategies for material properties modification of oxide TFTs. The developed semiconducting hydrogenated a-Ga_2O_x are described in detail. To achieve semiconducting behavior of solution-processed a-Ga_2O_x, the strategy is to shift the Fermi level position closer to the conduction band by performing various annealing condition. The Fermi level shifting phenomena is investigated by secondary ion mass spectrometry and is explained as a crucial mechanism which drive material conversion.

Chapter 3 starts with a critical point of solution deposition technique and current

strategies to address those issues. The developed semiconducting as-deposited a-Ga_2O_x are described in detail. To achieve semiconducting behavior of as-deposited a-Ga_2O_x, the strategy is by controlling the precursor aging time and relative humidity during film deposition.

Chapter 4 highlights the utilization of machine learning as an optimization method for accelerating material design and device fabrication. In particular, how this method is beneficial for developing novel materials with limited literature such as solution-processed a-Ga_2O_x. The strategy is by utilizing machine learning as an approach for predicting Fermi level of solution-processed a-Ga_2O_x.

The dissertation is concluded in Chapter 5 by summarizing the findings and providing suggestion for future studies.

1.8 References

[1] X. Hou, X. Zhao, Y. Zhang, Z. Zhang, Y. Liu, Y. Qin, P. Tan, C. Chen, S. Yu, M. Ding, G. Xu, Q. Hu, and S. Long, "High-Performance Harsh-Environment-Resistant GaOX Solar-Blind Photodetectors via Defect and Doping Engineering," *Adv. Mater.*, vol. 34, no. 1, pp. 1–11, 2022, doi: 10.1002/adma.202106923.

[2] S. Park, C. H. Kim, W. J. Lee, S. Sung, and M. H. Yoon, "Sol-gel metal oxide dielectrics for all-solution-processed electronics," *Mater. Sci. Eng. R Reports*, vol. 114, pp. 1–22, 2017, doi: 10.1016/j.mser.2017.01.003.

[3] S. O. Kasap and J. A. Rowlands, "X-ray photoconductors and stabilized a-Se for direct conversion digital flat-panel X-ray image-detectors," *J. Mater. Sci. Mater. Electron.*, vol. 11, no. 3, pp. 179–198, 2000, doi: 10.1023/A:1008993813689.

[4] Y. Qin, S. Long, Q. He, H. Dong, G. Jian, Y. Zhang, X. Hou, P. Tan, Z. Zhang, Y. Lu, C. Shan, J. Wang, W. Hu, H. Lv, Q. Liu, and M. Liu, "Amorphous Gallium Oxide-Based Gate-Tunable High-Performance Thin Film Phototransistor for Solar-Blind Imaging," *Adv. Electron. Mater.*, vol. 5, no. 7, Jul. 2019, doi: 10.1002/aelm.201900389.

[5] Z. Han, H. Liang, W. Huo, X. Zhu, X. Du, and Z. Mei, "Boosted UV Photodetection Performance in Chemically Etched Amorphous Ga2O3 Thin-Film Transistors," *Adv. Opt. Mater.*, vol. 8, no. 8, Apr. 2020, doi: 10.1002/adom.201901833.

[6] F. Liao, C. Chen, and V. Subramanian, "Organic TFTs as gas sensors for electronic nose applications," *Sensors Actuators, B Chem.*, vol. 107, no. 2, pp. 849–855, 2005, doi: 10.1016/j.snb.2004.12.026.

[7] P. Estrela and P. Migliorato, "Chemical and biological sensors using polycrystalline silicon TFTs," *J. Mater. Chem.*, vol. 17, no. 3, pp. 219–224, 2007, doi: 10.1039/b612469k.

[8] T. Kamiya, K. Nomura, and H. Hosono, "Present status of amorphous In-Ga-Zn-O thin-film transistors," *Sci. Technol. Adv. Mater.*, vol. 11, no. 4, 2010, doi: 10.1088/1468-6996/11/4/044305.

[9] S. M. Sze and K. K. Ng, "Physics of Semiconductor Devices," *Phys. Semicond. Devices*, p. 2006, 2006, doi: 10.1002/0470068329.

[10] L. Y. Su, H. Y. Lin, H. K. Lin, S. L. Wang, L. H. Peng, and J. Huang, "Characterizations of amorphous IGZO thin-film transistors with low subthreshold swing," *IEEE Electron Device Lett.*, vol. 32, no. 9, pp. 1245–1247, 2011, doi: 10.1109/LED.2011.2160931.

[11] H. A. Klasens and H. Koelmans, "A tin oxide field-effect transistor," *Solid State Electron.*, vol. 7, no. 9, pp. 701–702, 1964, doi: 10.1016/0038-1101(64)90057-7.

[12] K. Nomura, H. Ohta, A. Takagi, T. Kamiya, M. Hirano, and H. Hosono, "Room-temperature fabrication of transparent flexible thin-film transistors using amorphous oxide semiconductors," *Nature*, vol. 432, no. 7016, pp. 488–492, 2004, doi: 10.1038/nature03090.

[13] T. Arai, "Oxide-TFT technologies for next-generation AMOLED displays," *J. Soc. Inf. Disp.*, vol. 20, no. 3, p. 156, 2012, doi: 10.1889/jsid20.3.156.

[14] J. Jang, J. K. Um, and M. Mativenga, "Reliability of oxide TFT for display application," *Proc. Int. Symp. Phys. Fail. Anal. Integr. Circuits, IPFA*, pp. 373–376, 2013, doi: 10.1109/IPFA.2013.6599184.

[15] A. Suresh, P. Wellenius, V. Baliga, H. Luo, L. M. Lunardi, and J. F. Muth, "Fast all-transparent integrated circuits based on indium gallium zinc oxide thin-film transistors," *IEEE Electron Device Lett.*, vol. 31, no. 4, pp. 317–319, 2010, doi: 10.1109/LED.2010.2041525.

[16] Y. Li, J. Yang, Y. Wang, P. Ma, Y. Yuan, J. Zhang, and Z. Lin, "Complementary Integrated Circuit Based on p-Type SnO and n-Type IGZO Thin-Film Transi," vol. 39, no. 2, pp. 208–211, 2018.

[17] Y. Hu, L. Q. Guo, C. Huo, M. Dai, T. J. Webster, and J. Ding, "Transparent nano thin-film transistors for medical sensors, oled and display applications," *Int. J. Nanomedicine*, vol. 15, pp. 3597–3603, 2020, doi: 10.2147/IJN.S228940.

[18] Y. Hashima, T. Takahashi, Y. Ishikawa, and Y. Uraoka, "Development of High-Reliability and -Stability Chemical Sensors Based on an Extended-Gate Type Amorphous Oxide Semiconductor Thin-Film Transistor," *ACS Appl. Electron. Mater.*, vol. 2, no. 2, pp. 405–408, 2020, doi: 10.1021/acsaelm.9b00844.

[19] M. Riordan, L. Hoddeson, and C. Herring, "The invention of the transistor," *Rev. Mod. Phys.*, vol. 71, no. SUPPL. 2, 1999, doi: 10.1103/revmodphys.71.s336.

[20] J. Y. Tsao, J. Han, R. H. Haitz, and P. M. Pattison, “The Blue LED Nobel Prize: Historical context, current scientific understanding, human benefit,” *Ann. Phys.*, vol. 527, no. 5–6, pp. A53–A61, 2015, doi: 10.1002/andp.201570058.

[21] S. Nakamura and M. R. Krames, “History of gallium-nitride-based light-emitting diodes for illumination,” *Proc. IEEE*, vol. 101, no. 10, pp. 2211–2220, 2013, doi: 10.1109/JPROC.2013.2274929.

[22] J. Y. Tsao *et al.*, “Ultrawide-Bandgap Semiconductors: Research Opportunities and Challenges,” *Adv. Electron. Mater.*, vol. 4, no. 1, 2018, doi: 10.1002/aelm.201600501.

[23] H. Zhou, L. Cong, J. Ma, B. Li, M. Chen, H. Xu, and Y. Liu, “High gain broadband photoconductor based on amorphous Ga2O3 and suppression of persistent photoconductivity,” *J. Mater. Chem. C*, vol. 7, no. 42, pp. 13149–13155, 2019, doi: 10.1039/c9tc05159g.

[24] M. Higashiwaki, K. Sasaki, A. Kuramata, T. Masui, and S. Yamakoshi, “Gallium oxide (Ga 2O 3) metal-semiconductor field-effect transistors on single-crystal β-Ga 2O 3 (010) substrates,” *Appl. Phys. Lett.*, vol. 100, no. 1, pp. 1–4, 2012, doi: 10.1063/1.3674287.

[25] T. Oshima, T. Okuno, N. Arai, N. Suzuki, S. Ohira, and S. Fujita, “Vertical solar-blind deep-ultraviolet schottky photodetectors based on β-Ga2O3 substrates,” *Appl. Phys. Express*, vol. 1, no. 1, 2008, doi: 10.1143/APEX.1.011202.

[26] S. Mitra, Y. Pak, B. Xin, D. R. Almalawi, N. Wehbe, and I. S. Roqan, “Solar-Blind Self-Powered Photodetector Using Solution-Processed Amorphous Core-Shell Gallium Oxide Nanoparticles,” *ACS Appl. Mater. Interfaces*, vol. 11, no. 42, pp. 38921–38928, Oct. 2019, doi: 10.1021/acsami.9b11694.

[27] T. Kamiya and H. Hosono, “Material characteristics and applications of transparent amorphous oxide semiconductors,” *NPG Asia Mater.*, vol. 2, no. 1, pp. 15–22, 2010, doi: 10.1038/asiamat.2010.5.

[28] S. J. Pearton, J. Yang, P. H. Cary IV, F. Ren, J. Kim, M. J. Tadjer, and M. A. Mastro, “A review of Ga2O3 materials, processing, and devices,” *Appl. Phys. Rev.*, vol. 5, p. 011301, 2018.

[29] H. Liang, Z. Han, and Z. Mei, “Recent Progress of Deep Ultraviolet Photodetectors using Amorphous Gallium Oxide Thin Films,” *Phys. Status Solidi Appl. Mater. Sci.*, vol.

218, no. 1, p. 2000339, Jan. 2021, doi: 10.1002/pssa.202000339.

[30] D. Purnawati, J. P. Bermundo, and Y. Uraoka, "Insulator-to-semiconductor conversion of solution-processed ultra-wide bandgap amorphous gallium oxide via hydrogen annealing," *Appl. Phys. Express*, vol. 15, no. 2, p. 24003, 2022, doi: 10.35848/1882-0786/ac466a.

[31] J. Kim, T. Sekiya, N. Miyokawa, N. Watanabe, K. Kimoto, K. Ide, Y. Toda, S. Ueda, N. Ohashi, H. Hiramatsu, H. Hosono, and T. Kamiya, "Conversion of an ultra-wide bandgap amorphous oxide insulator to a semiconductor," *NPG Asia Mater.*, vol. 9, no. 3, 2017, doi: 10.1038/am.2017.20.

[32] Y. Chen, Y. Lu, M. Liao, Y. Tian, Q. Liu, C. Gao, X. Yang, and C. Shan, "3D Solar-Blind Ga2O3 Photodetector Array Realized Via Origami Method," *Adv. Funct. Mater.*, vol. 29, no. 50, pp. 1–8, 2019, doi: 10.1002/adfm.201906040.

[33] Y. Li, X. Hu, Z. Liu, and J. Ren, "Power and gas pressure effects on properties of amorphous In-Ga-ZnO films by magnetron sputtering," *J. Mater. Sci. Mater. Electron.*, vol. 23, no. 2, pp. 408–412, 2012, doi: 10.1007/s10854-011-0467-x.

[34] K. Nomura, A. Takagi, T. Kamiya, H. Ohta, M. Hirano, and H. Hosono, "Amorphous oxide semiconductors for high-performance flexible thin-film transistors," *Japanese J. Appl. Physics, Part 1 Regul. Pap. Short Notes Rev. Pap.*, vol. 45, no. 5 B, pp. 4303–4308, 2006, doi: 10.1143/JJAP.45.4303.

[35] J. S. Park, J. Sheng, J. H. Han, W. H. Choi, and J. Park, "Performance and Stability Enhancement of In-Sn-Zn-O TFTs Using SiO2 Gate Dielectrics Grown by Low Temperature Atomic Layer Deposition," *ACS Appl. Mater. Interfaces*, vol. 9, no. 49, pp. 42928–42934, 2017, doi: 10.1021/acsami.7b15419.

[36] M. K. Yadav, A. Mondal, S. Das, S. K. Sharma, and A. Bag, "Impact of annealing temperature on band-alignment of PLD grown Ga2O3/Si (100) heterointerface," *J. Alloys Compd.*, vol. 819, p. 153052, 2020, doi: 10.1016/j.jallcom.2019.153052.

[37] D. C. Corsino, J. P. S. Bermundo, C. Kulchaisit, M. N. Fujii, Y. Ishikawa, H. Ikenoue, and Y. Uraoka, "High-Performance Fully Solution-Processed Oxide Thin-Film Transistors via Photo-Assisted Role Tuning of InZnO," *ACS Appl. Electron. Mater.*, vol. 2, no. 8, pp. 2398–2407, 2020, doi: 10.1021/acsaelm.0c00348.

[38] W. Xu, H. Li, J. Bin Xu, and L. Wang, "Recent Advances of Solution-Processed Metal Oxide Thin-Film Transistors," *ACS Appl. Mater. Interfaces*, vol. 10, no. 31, pp. 25878–25901, 2018, doi: 10.1021/acsami.7b16010.

[39] J. W. Park, B. H. Kang, and H. J. Kim, "A Review of Low-Temperature Solution-Processed Metal Oxide Thin-Film Transistors for Flexible Electronics," *Adv. Funct. Mater.*, vol. 30, no. 20, pp. 1–40, 2020, doi: 10.1002/adfm.201904632.

[40] G. Adamopoulos, S. Thomas, P. H. Wöbkenberg, D. D. C. Bradley, M. A. McLachlan, and T. D. Anthopoulos, "High-mobility low-voltage ZnO and Li-doped ZnO transistors based on ZrO2 high-k dielectric grown by spray pyrolysis in ambient air," *Adv. Mater.*, vol. 23, no. 16, pp. 1894–1898, 2011, doi: 10.1002/adma.201003935.

[41] Y. H. Yang, S. S. Yang, and K. Sen Chou, "Characteristic enhancement of solution-processed In-Ga-Zn oxide thin-film transistors by laser annealing," *IEEE Electron Device Lett.*, vol. 31, no. 9, pp. 969–971, 2010, doi: 10.1109/LED.2010.2055821.

[42] R. Yao, Z. Zheng, Z. Fang, H. Zhang, X. Zhang, H. Ning, L. Wang, J. Peng, W. Xie, and X. Lu, "High-performance flexible oxide TFTs: Optimization of a-IGZO film by modulating the voltage waveform of pulse DC magnetron sputtering without post treatment," *J. Mater. Chem. C*, vol. 6, no. 10, pp. 2522–2532, 2018, doi: 10.1039/c7tc04970f.

[43] J. P. S. Bermundo, Y. Ishikawa, M. N. Fujii, H. Ikenoue, and Y. Uraoka, "Instantaneous Semiconductor-to-Conductor Transformation of a Transparent Oxide Semiconductor a-InGaZnO at 45 °c," *ACS Appl. Mater. Interfaces*, vol. 10, no. 29, pp. 24590–24597, 2018, doi: 10.1021/acsami.8b05008.

[44] Y. Chen, Y. Lu, X. Yang, S. Li, K. Li, X. Chen, Z. Xu, J. Zang, and C. Shan, "Bandgap engineering of Gallium oxides by crystalline disorder," *Mater. Today Phys.*, vol. 18, p. 100369, 2021, doi: 10.1016/j.mtphys.2021.100369.

[45] M. H. Cho, C. H. Choi, and J. K. Jeong, "Comparative Study of Atomic Layer Deposited Indium-Based Oxide Transistors with a Fermi Energy Level-Engineered Heterojunction Structure Channel through a Cation Combinatorial Approach," *ACS Appl. Mater. Interfaces*, vol. 14, no. 16, pp. 18646–18661, 2022, doi: 10.1021/acsami.1c23889.

[46] B. R. Tak, S. Dewan, A. Goyal, R. Pathak, V. Gupta, A. K. Kapoor, S. Nagarajan, and

R. Singh, "Point defects induced work function modulation of β-Ga 2 O 3," *Appl. Surf. Sci.*, vol. 465, no. June 2018, pp. 973–978, 2019, doi: 10.1016/j.apsusc.2018.09.236.

[47] H. Yang, Y. Qian, C. Zhang, D. S. Wuu, D. N. Talwar, H. H. Lin, J. F. Lee, L. Wan, K. He, and Z. C. Feng, "Surface/structural characteristics and band alignments of thin Ga 2 O 3 films grown on sapphire by pulse laser deposition," *Appl. Surf. Sci.*, vol. 479, no. January, pp. 1246–1253, 2019, doi: 10.1016/j.apsusc.2019.02.069.

Chapter 2 Insulator-to-Semiconductor conversion of solution-processed UWB a-Ga2Ox film via Fermi level engineering

2.1 Introduction

The global market is growing rapidly and demanding for next-generation electronics which require large-scale production using transparent, cost-effective and harsh-environment-resistant materials. This trend has pushed the boundaries of technology by enabling large-scale fabrication *via* solution deposition technique. Although vacuum deposition technique offers unquestionably high film quality as well as device performance, its application is restricted because of its high cost, high energy requirement, experiment complexity, and difficulty in scaling to large-area electronics [1][2][3]. Therefore, solution process has become the superior alternative method due to large-area fabrication, equipment simplicity, atmospheric processing, and low cost [2][3].

As introduced in Chapter 1, a huge research interest has been shifted from wide bandgap materials (E_g > 3.0 eV) to ultra-wide bandgap materials (E_g > 4.0 eV). Ultra-wide bandgap materials, such as amorphous Gallium Oxide (a-Ga_2O_x), is currently regarded as one of the most promising material due to its excellent optical quality (E_g > 4.8 eV), device design flexibility, harsh-environment resistance, cost-effectiveness, and solution-processed compatibility [4][5][6][7]. It has been widely used for various electronic devices such as solar blind ultra-violet photodetectors, sensors, and thin-film transistors (TFTs) [5][7][8][9][1]. In addition, it exhibits decent device performance which is comparable to single crystalline gallium oxide in selected applications [4][5]. With those excellent properties, fabricating solution-processed a-Ga_2O_x will encourage the realization of future devices which are large-scale, highly transparent, cost-effective, and harsh environment-resistant.

Nevertheless, obtaining electrical conduction on as-deposited a-Ga_2O_x is quite challenging because the combination of ultra-wide bandgap (UWB) and an amorphous structure has serious difficulties in encouraging electron mobility. Thus, it tends to exhibit insulating behavior, particularly in solution-processed a-Ga_2O_x. Therefore, developing semiconducting solution-processed UWB a-Ga_2O_x will be a superb research achievement from a materials engineer's

perspective. Likewise, it will widen the range of oxide material applications from industry perspectives.

This chapter demonstrates insulator-to-semiconductor conversion of solution processed ultra-wide bandgap a-Ga_2O_x material. The key strategy of material conversion is to enhance the electrical properties which is represented as the E_F relative position shift closer to the conduction band. For *n*-type semiconductor, particularly a-Ga_2O_x, this shifting phenomenon towards the conduction band implies an increase in electron carrier concentration which further improve the film conductivity and the TFT device as well. The material design technique based on Fermi level shifting phenomena is further named as Fermi level engineering.

Section 2.2 presents the recent methods in enhancing electrical properties of oxide materials such as thermal annealing, photo-assisted annealing, and film density modification. The advantages and disadvantages of each type will also be discussed. In particular, hydrogenation or hydrogen doping method is presented in section 2.3 as an alternative method for oxide material conversion. The hydrogen-doping principles, challenges and various hydrogen-incorporation method will also be discussed. This section will highlight the superiority of hydrogen annealing over other incorporation methods.

The first report in solution-processed a-Ga_2O_x material conversion was presented in section 2.4 as the superb achievement. For further investigation, film characteristics and TFT device performance were evaluated in section 2.5 and 2.6 respectively. Eventually, section 2.7 present the mechanism on how the hydrogen-incorporated affected the electrical properties of a-Ga_2O_x.

2.2 Insulator-to-semiconductor conversion methods

As mentioned in section 2.1, as-deposited a-Ga_2O_x mostly exhibit insulating behavior owing to its insufficient electron mobility and carrier concentration. Therefore, semiconducting a-Ga_2O_x can be obtained by enhancing the electron mobility by various methods which is appropriate for amorphous ultra-wide bandgap material. At the moment, several research approaches have been proposed to enhance the electrical properties of oxide materials such as thermal annealing [10], photo-assisted annealing [2][11][12][13][14], and film density modification [1].

In 2008, Nagarajan *et al.* highlighted the use of conventional thermal annealing for demonstrating insulator-to-metal transition of Gallium Oxide (Ga_2O_3) material. All Ga_2O_3 films are confirmed as insulator at room temperature. Once the films are heated up to 673 K,

the pronounce insulator-to-metal transition is observed for the films prepared in Argon atmosphere. At 673 K (~400 °C), the conductivity increases by seven orders of magnitude (10^3 S cm^{-1}). This excellent improvement is mainly induced by crystallization of stoichiometric Ga_2O_3 within metastable oxide matrix by disproportionation (chemically driven). Although conventional thermal annealing has successfully enhanced the film conductivity, it is mostly applied at relatively high temperature, particularly for thermally stable material such as Gallium Oxide [4]. In addition, obtaining electron conduction in Ga_2O_3 is not as challenging as a-Ga_2O_x, because Ga_2O_3 is a crystalline material. If high temperature of ~400 °C was needed to improved conductivity of Ga_2O_3, higher temperature will be needed to modified the conductivity of a-Ga_2O_x, particularly the solution-processed UWB a-Ga_2O_x.

Additionally, high temperature annealing tends to trahindensform oxide materials from an amorphous phase to crystalline phase which increase the surface roughness that further deteriorate the device performance [11]. Therefore, different annealing approaches which maintain amorphous phase of oxide materials is required. In consequence, new processing paradigm such as photo-assisted annealing has been proposed as a substitute method of conventional thermal annealing.

In general, thermal annealing is performed in solution processed materials for 3 reasons: solvent evaporation, precursor-related impurities evaporation and metal oxide formation. Thus, a certain temperature is required for a specific oxide material. Kang *et al.* (2016) revealed that Indium Oxide precursor is completely converted to oxide film after annealing at 120 °C (1 hour) and subsequent exposure to flash lamp annealing (FLA) for 30 s. The heat from 120 °C annealing is used for solvent evaporation. Whereas the heat induced from FLA is used to generate metal oxide formation. After > 30 s exposure, prominent oxide conversion which leads to good carrier transport properties is observed. After prolonging the exposure time, the light energy breaks the metal-oxide bond and creates oxygen vacancy (V_O) which fill the trap states at crystal domain boundaries and increasing the carrier transport properties [13].

To date, photo-assisted is considered an alternative annealing method which rely on the heat induced by photonic process. Several light sources such as flash lamp [13][12][14], mercury and excimer lamp[15], excimer laser [2] and ultra violet irradiation [14][2][16] have been widely used for photo-assisted annealing (***Table 2-1***). Despite excellent electrical improvement of photo-assisted annealing, the light energy is limited in its application to wide bandgap ($E_g \geq 3.0$ eV) oxide materials such as IZO, In_2O_3, IGZO, Ta_2O_3 etc. The effective energy of light source within visible and ultra-violet (UV) ranges are insufficient to enhance ultra-wide bandgap ($E_g \geq 4.0$ eV) oxide materials. Thereby, an appropriate method is required

for ultra-wide bandgap material, particularly a-Ga_2O_x.

In 2017, Kim *et al.* demonstrated a superb semiconducting vacuum-processed a-Ga_2O_x *via* film density modification. By increasing the film growth rate, higher film density was obtained which further suppressed the electron trap formation. The electrical conductivity increases exponentially with the increase in the film density. The minimum film density to obtain semiconducting a-Ga_2O_x is 5.2 g/cm^3 [1]. Nevertheless, as mentioned in chapter 2.1, large-scale production can be realized mainly if the film was deposited *via* solution deposition technique. Therefore, a proposed method by Kim *et al.* is likely inappropriate to solution-processed a-Ga_2O_x. The semiconducting behavior of insulating solution-processed a-Ga_2O_x might be achieved by performing material conversion for instance by introduce hydrogen doping which will be further discussed in section 2.3.

Table 2-1. Summary of various light sources for photo-assisted annealing.

Semiconductor	Light source	Light energy (eV)	Ref.
a-IZO	UV light	4.8 eV (85%), 6.7 eV (15%)	[2]
a-IZO	Excimer laser	4.9 eV	[2]
In_2O_3	Flash lamp	0.8 – 6.2 eV	[12]
In_2O_3	Flash lamp	0.8 – 6.2 eV	[13]
IGZO	Flash lamp	1.3 – 3.2 eV	[14]
IGZO	UV	4.4 – 6.9 eV	[14]
Ta_2O_5	Excimer lamp	3.5 eV (XeF)	[15]
Ta_2O_5	Mercury lamp	4.8 and 6.7 eV	[15]
IGZO	Deep UV	4.9 eV	[16]

2.3 Hydrogen-doping principles and challenges

In amorphous oxide semiconductors, potential barrier distribution around the conduction band minimum is formed by structural randomness of amorphous structure which hinders carrier transport. Once the carrier concentration increases, the potential barrier can be overcome and the carrier mobility can be improved [17]. Furthermore, it was reported that carrier mobility of IGZO increased as the carrier concentration increased [18][19][20]. The carrier concentration of *n*-type semiconductor, such as IGZO, can be controlled by introducing hydrogen dopant. As the hydrogen (H_2) is known as donor for various *n*-type semiconductors

[21][22][23], hydrogen doping is carried out to improve the electrical characteristics of TFTs. In addition, hydrogen is an effective passivator for defects. The hydrogen can passivate the deep states (defect sites due to oxygen deficiency) and interface trap state which reduces the threshold voltage (V_{th}) [24].

Nonetheless, it should be highlighted that the TFT characteristics of hydrogenated-IGZO are varied with the amount of hydrogen dose [25]. Kim *et al.* in 2012 revealed that the IGZO TFTs performance are improved as hydrogen plasma treatment time increased. However, prolonging the treatment time leads to TFT deterioration. The hydrogenated IGZO TFTs exhibit severe humps in the transfer characteristics and increment of subthreshold swing (SS). These deteriorations are attributed to excessively doped hydrogen which leads to interstitial defects rather than acting as defect passivator. Thus, the challenge of hydrogen doping method is to control the hydrogen dose at considerate amount. Fundamentally, the hydrogen dose can be modulated by controlling the hydrogen sources dose such as hydrogen gas or hydrogen plasma depending on the hydrogen-incorporation method. Various hydrogen-incorporated methods will be discussed in section 2.3.1.

2.3.1 Hydrogen-doping methods

As mentioned in section 2.3, the carrier concentration of most *n*-type semiconductor can be controlled by introducing hydrogen dopant. Since Gallium Oxide (Ga_2O_3) is known as an *n*-type semiconductor [4], this method is likely applicable for solution-processed ultra-wide bandgap a-Ga_2O_x material. Various methods to implant hydrogen (H_2) to oxide materials are developed and summarized in ***Table 2-2***.

In general, there are 2 principal methods to incorporate hydrogen dopant: pre-treatment and post-treatment. Pre-treatment means the incorporation occurs during film deposition, prior to film formation. The hydrogen gas flowed during film deposition and hydrogen will further diffuse and be incorporated [26]. On the other hand, post-treatment is where the incorporation occurs after film formation. This treatment includes hydrogen diffusion [22], hydrogen plasma [25][27], and hydrogen annealing [17].

Sato *et al.* (2009) demonstrated hydrogen diffusion phenomena of coplanar homojunction a-IGZO TFT (***Figure 2.1***). A SiO_x/SiN_x:H bilayer film was deposited onto a-IGZO layer by PECVD at 250 °C. The hydrogen from SiO_x/SiN_x:H which serves as donor was diffused into a-IGZO film and improved its conductivity. Thus, the a-IGZO region with SiO_x (indicated as

blue color of SiO_x) capping layer remain as semiconducting channel, while the region without capping layer is converted into conductive source/drain a-IGZO. The contact holes were created and Molybdenum (Mo) was deposited and patterned as wiring from a-IGZO source/drain region.

Table 2-2. Comparison of electrical properties of oxide film and TFTs performance with various hydrogen-doping methods.

Method	μ_{Hall} (cm^2/Vs)		n_e (cm^{-3})		μ_{sat} (cm^2/Vs)	Annealing (°C)	Ref.
	As-depo	H-doped	As-depo	H-doped			
PECVD-SiN_x:H	11	17	5.6×10^{16}	7.8×10^{19}	-	-	[22]
H_2 plasma	-	-	1.0×10^{14}	1.5×10^{20}	-	-	[25][27]
Deposition under Ar/H_2 ambient	1.2	0.3	7.4×10^{18}	5.3×10^{19}	3.6	-	[26]
H_2 annealing	16	15	7.0×10^{19}	2.0×10^{20}	-	300	[28]
	-	-	-	-	8.6	300	[29]
	1.8	6.4	3.4×10^{14}	10^{17}~10^{19}	7.4	260	[17]

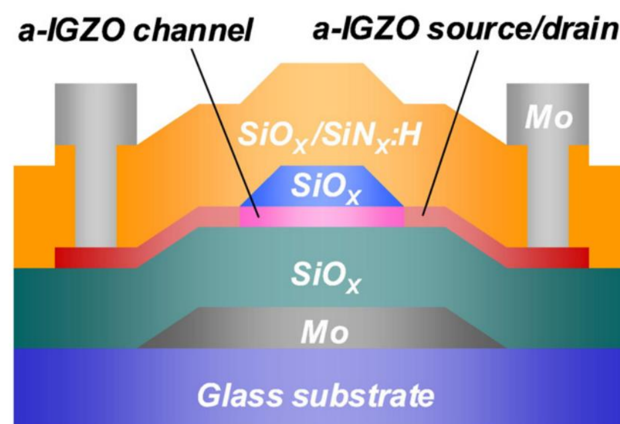

Figure 2.1. Cross-sectional schematic of coplanar homojunction a-IGZO TFT [22].

Moreover, hydrogenated IGZO *via* hydrogen plasma shows TFTs device improvement [25][27]. The hydrogen from hydrogen plasma treatment acts as shallow donor carriers, such as H^+ and OH [27]. The hydrogen which diffused to 50 nm-depth of a-IGZO, passivated the oxygen deficiency and the total trap which existed in channel layer and channel-gate insulator interface [25][27]. The presence of hydrogen in a-IGZO further improved its conductivity and transformed to conductive source/drain (***Figure 2.2***). By using a-IGZO as channel and source/drain at the same time, the contact resistance between channel and source/drain can be eliminated and the sheet resistance can be reduced [27]. Although the proper hydrogen dose well passivated the oxygen deficiency, excess hydrogen dose acted as excessive donors which exist as interstitial defects [25]. Additionally, prolonging the hydrogen plasma treatment time tends to damage the film surface and generate defect density [17].

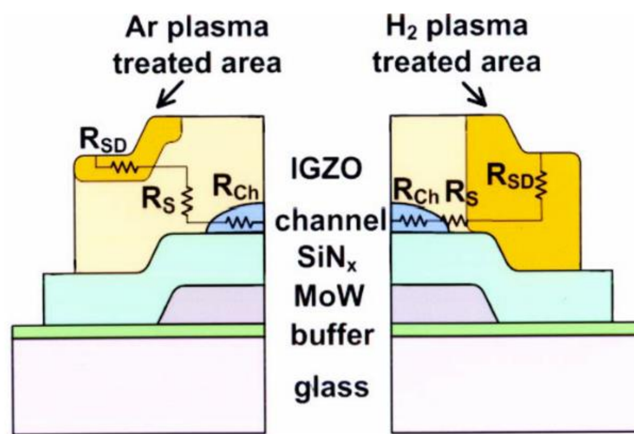

Figure 2.2. Schematic cross-sectional diagram of the total resistance in homojunction a-IGZO TFTs with Ar and H_2 plasma treatments [27].

In 2013, Oh *et al.* reported smoother surface of hydrogenated IGZO can be achieved by performed hydrogen annealing. After annealing the IGZO film at N_2 and H_2 ambient, the surface roughness was reduced. The smoothened surface is ascribed to film densification due to structural relaxation of IGZO which occurs during thermal annealing [30][31]. Hence, compared to existing hydrogenation methods which summarized in ***Table 2-2***, hydrogen annealing is apparently the most appropriate method to design semiconducting solution-processed ultra-wide bandgap a-Ga_2O_x. The detail of hydrogen annealing method will be discussed in section 2.3.2.

2.3.2 Hydrogen annealing

Hydrogen-incorporation *via* hydrogen-based annealing has been demonstrated by various methods such as hot isostatic pressing or HIP [28], high-pressure hydrogen annealing of HPHA [17], and post-thermal treatment of hydrogen annealing [29]. Kim *et al.* in 2011, carried out hydrogen-incorporation in an IGZO film using a hot isostatic pressing (HIP) method which was performed at 300 °C for 10 h under high pressure. Unlike hydrogen plasma treatment, the HIP did not activate hydrogen to form a reactive radical but it involved physical injection of atomic or molecular neutral state hydrogen. In addition, the hydrogen injected mainly occupies the Zn–O or Ga–O bond site rather than the In–O bond site. The hydrogen injection to the Zn–O or Ga–O bond site tends to generates free carrier. While the hydrogen injected to the In–O bond site particularly acts as a scattering center in the conduction path which decreases the mobility (μ).

In 2013, Oh *et al.* demonstrated hydrogenation of thin-film IGZO which was carried out by applying high-pressure hydrogen annealing (HPHA). The HPHA effectively increased the carrier concentration and Hall mobility of IGZO film. Moreover, the hydrogenated IGZO films exhibit smoother surface as compared to the as-deposited film. The increased carrier concentration in the HPHA samples strongly depends on the annealing temperature. By varying the annealing temperature from 260–280 °C, the carrier concentration is modulated from 10^{16} to 10^{19} cm^{-3}. Likewise, the negative shift of V_{th} was also observed as the annealing temperature increased which implies more carriers reside in the channel layer. Interestingly, the process temperature of HPHA is lower than the required process temperature of other reported hydrogenation methods. This is because the high hydrogen-incorporation rate in the HPHA process. According to Hendry's law, the hydrogen gas had higher solubility and higher diffusivity with higher hydrogen partial pressure at a given temperature [32].

Son *et al.* (2010) demonstrated post-treatment at 300 °C in H_2 gas ambient which increase the electron concentration of bottom-gate top-contact IGZO TFT. As shown in ***Figure 2.3***, the on current of hydrogenated IGZO TFT is higher than the one treated in O_2 and vacuum. In IGZO systems, hydrogen has been known to be a donor for *n*-type oxide semiconductors which improved IGZO film to be more conductive by increasing the electron concentration [27]. The increase in the electron concentration of IGZO is owing to percolation conduction through potential barriers in the vicinity of conduction band edge [18]. Furthermore, the increase in the electron concentration leads to negative shift of threshold voltage (V_{th}).

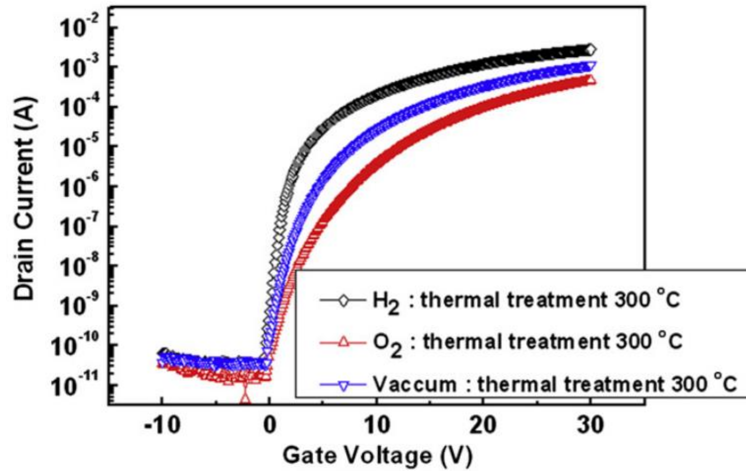

Figure 2.3. Transfer characteristics of Si/SiO_2/IGZO/Al TFT at V_D of 20 V [29].

To realize semiconducting ultra-wide bandgap a-Ga_2O_x, an appropriate method is needed to convert its conductivity without changing its amorphous phase. Although high-pressure system such as HIP and HPHA well passivated the deep states and interface trap state [24], the high pressure tends to rearranged the structure, densified [30][31] and transformed to crystalline phase in selected cases [17]. Therefore, instead of high-pressure system, conventional hydrogen annealing is preferred. In this study, the hydrogen annealing system is illustrated in ***Figure 2.4***. The hydrogen annealing treatment was performed in quartz glass tube under H_2/N_2 gas ambient.

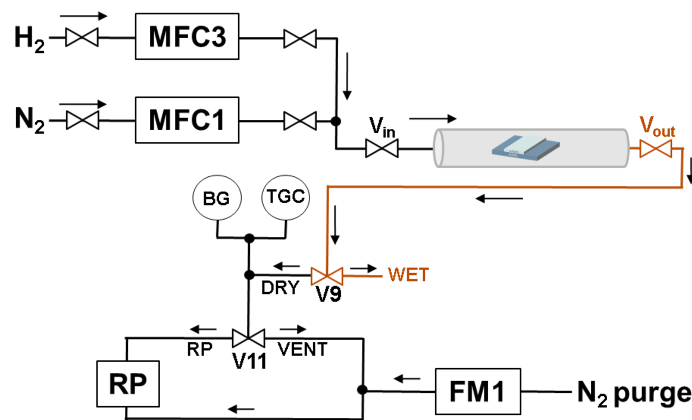

Figure 2.4. Schematic diagram of hydrogen annealing system that was used in this study.

2.3.3 Fabrication process of hydrogen-annealed solution-processed ultra-wide bandgap a-Ga_2O_x TFTs

2.3.3.1 Materials and precursor preparation

Solution-processed deposition technique has been widely developed for realization of large-scale production. Nonetheless, precursor-related impurities are highlighted as the major drawback of solution deposition approach. In general, a certain temperature is needed to completely evaporate the precursor-related impurities. Uncomplete evaporation affects the film formation, metal-oxide bond formation as well as the TFT device performance [33]. In addition, solution deposition technique is highly environment-dependent. For instance, it is relative humidity dependent, which might be another origin of impurities. In other words, the impurities might originate from the precursor-related impurities and/or environment-related impurities. Therefore, relatively high temperature is required for impurities evaporation. In particular, this section discussed the precursor-related impurities reduction by the precursor selection. The detail in the effect of precursor-related impurities and environment-related impurities will be discussed in chapter 3.

There have been numerous improvements in the chemistry to lowered down the processing temperature by solute and solvent engineering. The goal is to lower the processing temperature without unwanted impurities left after thermal decomposition. In 2008, Altungbas and colleagues [34] reported the effect of precursor selection to the structural and optical properties of ZnO thin-films. The ZnO films were fabricated from three different precursors (zinc nitrate, zinc acetate and zin chloride) at the same annealing temperature. The result reveals that different ZnO films had different surface morphologies and optical bandgaps cause by different decomposition temperatures, as illustrated in ***Figure 2.5***. Although the same annealing temperature was used, the film characteristics and device performances were determined by the precursor selection. Similar studies on HIZO and IZO precursor selection (zinc nitrate, zinc acetate, and zinc chloride) were also reported [35][36]. Among of these precursors, zinc nitrate exhibited the greatest weight loss of the residual organic materials at low temperature which implies fastest metal oxide formation (***Figure 2.5***). In consequence, zinc-nitrate-based TFTs exhibited the highest mobility and on/off ratio [35].

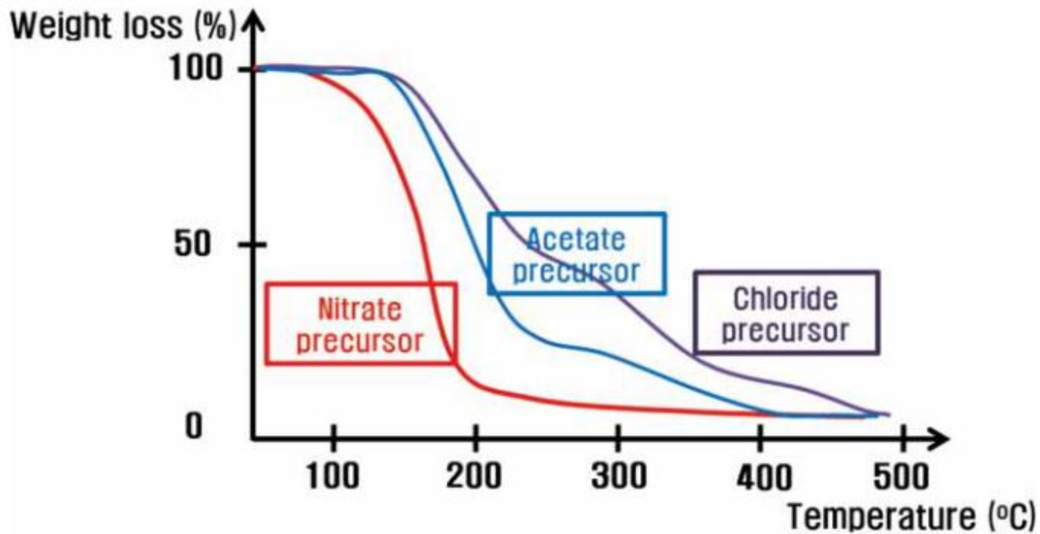

Figure 2.5. Comparison of weight loss with increasing temperature with respect to nitrate, acetate, and chloride precursors [33].

Furthermore, solvent selection is also critical in the conventional sol-gel process. A non-aqueous solvent, such as 2-methoxyethanol, must undergo high temperature annealing for metal-oxide formation. In contrast, an aqueous solvent, such as deionized water, has high complexity reaction caused by high reactivity of the metal-oxide precursors towards water [33]. Instead, in this study, 2-methoxyethanol was used as the solvent for gallium nitrate precursor.

In this study, Gallium oxide precursor (0.5 M) was synthesized *via* sol-gel method by dissolving gallium nitrate hydrate ($Ga(NO_3)_3{\cdot}xH_2O$ 99.999%, Sigma-Aldrich) in 2-methoxyethanol ($C_3H_8O_2$ anhydrous 99.8%, Sigma-Aldrich) under constant stirring at room temperature for 12 hours. The gallium oxide precursor was subsequently deposited after sol-gel process was finished. The detail on the precursor aging will be discussed in chapter 3.

2.3.3.2 Device fabrication

Figure 2.6 illustrates the experimental procedure for solution-processed a-Ga_2O_x TFT device fabrication. Heavily doped *p*-type Si substrates with thermally grown SiO_2 (85 nm) were used. To remove the organic residues on the substrates, conventional sulfuric-peroxide mixture (SPM) cleaning method was performed. The substrates were immersed in the H_2SO_4 solution

at 80 °C for 10 mins and subsequently the H_2O_2 solution was added for another 10 mins (***Figure 2.6***a). Prior to the deposition, the substrate surface hydrophilicity was improved by subjecting UV/O_3 treatment for 10 mins at 115 °C (***Figure 2.6***b) using SAMCO UV and Ozone Dry Stripper Model UV-1 with a wavelength of 254 nm (85%) and 185 nm (15%). The a-Ga_2O_x channel was deposited *via* spin coating technique at 2000 rpm for 15 s followed by 2-step baking process (***Figure 2.6***c). The pre-baking at 150 °C for 5 mins was performed to ensure that the solvent and precursor-related impurities have been completely evaporated. Whereas the post-baking at 500 °C for 5 mins was performed to generate metal-oxide formation and film densification without changing its phase to crystalline. The multiple-step baking process was subsequently performed until ~100 nm-thick-a-Ga_2O_x film was formed. Multi-stacking film deposition was done to fill physical voids that might be present in the preceding layers. In addition, this step is necessary to make the film denser and more homogeneous on each iteration of spin-coating and baking. The film thickness was controlled by controlling precursor volume per drop (30 μL), spin rate (2,000 rpm, 15 seconds), and number or layers. Afterwards, the final post-baking was done for 1 h.

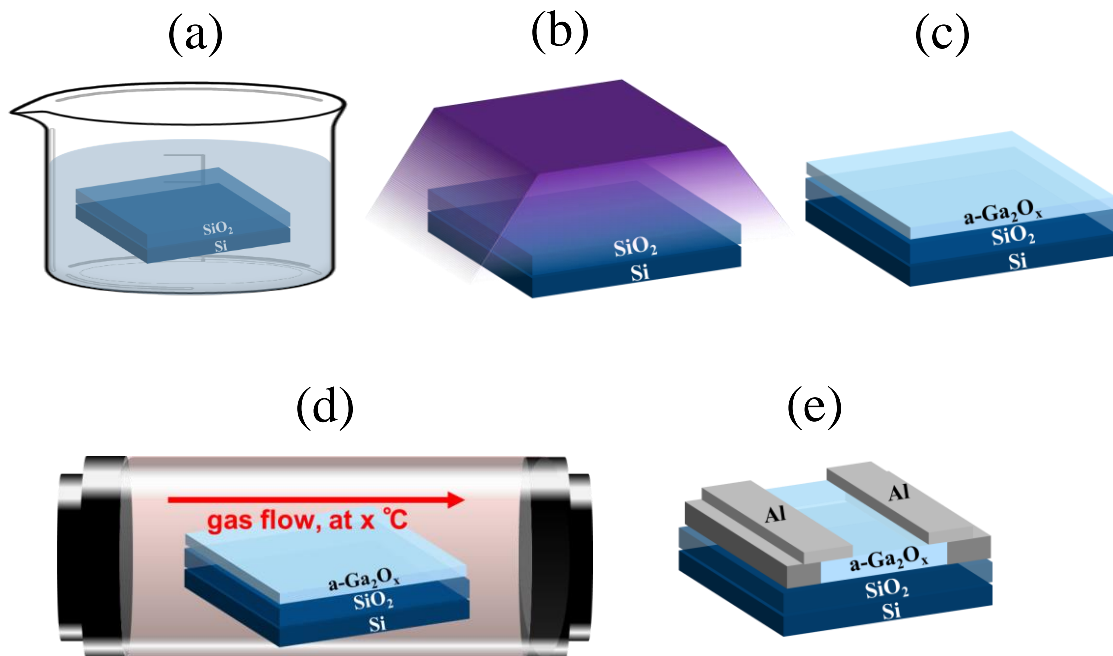

Figure 2.6. Schematic diagram of the fabrication process of a-Ga_2O_x TFTs. Started by (a) substrate cleaning via SPM process, (b) UV/O_3 treatment, (c) Gallium Oxide film deposition, (d) H_2-annealing treatment, and (e) film patterning and metal deposition.

The a-Ga_2O_x channel-islands were patterned by standard photolithography process and subsequently the wet etching was achieved using 0.05 M HCl solution. Afterwards, the a-Ga_2O_x film was annealed at 500 °C for 2 h under 4% hydrogen ambient (N_2:H_2 96:4%) which continuously flowed at a flowrate of 500 sccm (***Figure 2.6***d). Bottom-gate top-contact a-Ga_2O_x TFTs were fabricated by depositing 100-nm-thick Aluminum as source/drain electrodes *via* electron beam evaporation.

2.3.3.3 Characterization

The baking temperatures, pre-baking and post-baking, were determined by Thermogravimetry/Differential Scanning Calorimeter (TG-DSC; Hitachi DSC7000) measurement of a-Ga_2O_x precursor. The transfer characteristics of a-Ga_2O_x TFTs were analyzed using a semiconductor parameter analyzer (Agilent Technologies B1500A). Film thickness, phase structure, and film density were characterized and determined by profilometer, grazing incidence X-ray diffraction (XRD; Rigaku SmartLab9kW/IP/HY/N), and X-ray reflectivity spectroscopy (XRR; Rigaku SmartLab9kW/IP/HY/N), respectively. Optical bandgap values (E_g) and Valence band offset ($E_{V\text{-offset}}$) were estimated by ultraviolet-visible spectroscopy (UV-Vis; JASCO ILN-472) Tauc plot and X-ray photoemission spectroscopy (XPS; ULVAC-PHI 5000 VersaProbell). Finally, elemental analysis and hydrogen diffusion were evaluated by secondary ion mass spectroscopy (SIMS; ULVAC-PHI ADEPT-1010).

2.4 Achievement of semiconducting a-Ga_2O_x TFTs via hydrogen annealing

In fabricating a-Ga_2O_x film via solution process, temperature selection for pre-baking and post-baking are vital considerations since these temperatures can control the channel's film quality [7]. Those temperatures were determined by analyzing the thermal properties of Gallium Oxide precursor through TG-DSC measurement as shown in ***Figure 2.7***. The Gallium Oxide precursor exhibited gradual mass loss from ~25 °C to 120 °C which indicates evaporation of the solvent, 2-methoxyethanol. It was completely evaporated when it reached its boiling point at 124°C, which is also indicated by the ~90% mass loss.

The gallium nitrate hydrate ($Ga(NO_3)_3 \cdot xH_2O$) precursor contains three group compounds, which are gallium compound (Ga), nitrate compound ($(NO_3)_3$), and hydrate compound (H_2O). The hydrate compound was removed via thermally driven hydrolysis at ~100 °C indicated by a deep peak of endothermic reaction in DSC curve. Whereas the nitrate compound was removed via thermal decomposition at 124 °C to 138 °C which is observed as ~4% weight loss. Thus, the pre-bake temperature was chosen at 150 °C to ensure that the solvent and precursor-related impurities have been completely removed. The metal oxide started to form at ~200°C and followed by densification at 380°C. While the film was crystallized at 680°C. Therefore, the post-bake temperature was chosen at 500°C to ensure the metal oxide formation and densification of the film without changing its phase to crystalline. By applying both pre-bake and post-bake temperatures, the as-deposited a-Ga_2O_x films will be obtained. The hydrogenated film or the H_2-annealed a-Ga_2O_x films were obtained by applying hydrogen annealing as explained in section 2.3.3.2. The film characteristics of as-deposited and H_2-annealed a-Ga_2O_x films will be discussed in section 2.4.1.

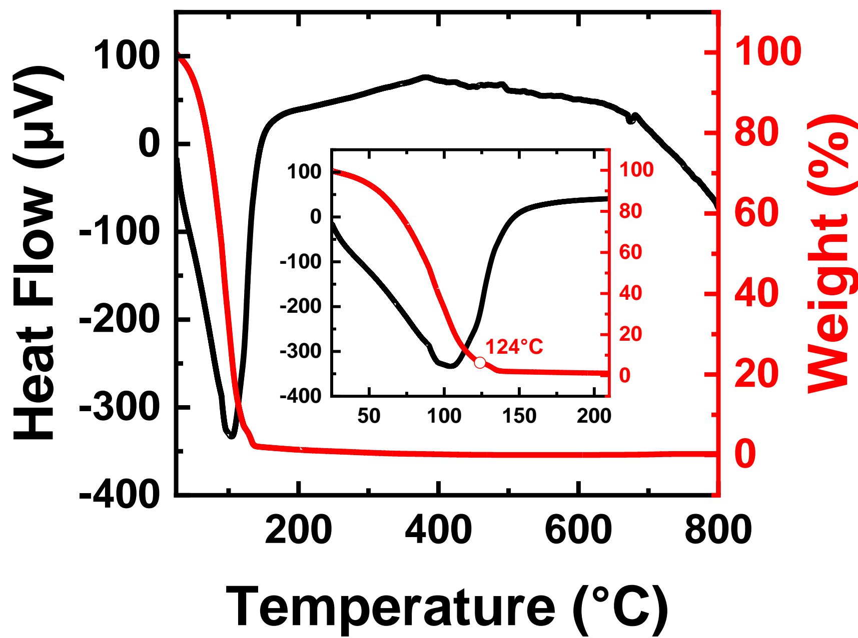

Figure 2.7. TG (red) and DSC (black) thermograph of Gallium Oxide precursor.

2.4.1 Film characteristics

The phase structural properties of the as-deposited and H_2-annealed Gallium Oxide films on Si/SiO_2 substrates were examined by using grazing incidence X-ray diffraction (XRD)

analysis. As displayed in ***Figure 2.8***a, the as-deposited Gallium Oxide film exhibits an amorphous structure which indicates as broad peak around 2θ of 30–40° which is assigned to monoclinic Gallium Oxide crystal structure. Similar XRD pattern was observed after performing H_2 annealing treatment at 500 °C. Despite being annealed at 500 °C, the H_2 annealing treatment can retain the amorphous nature of a-Ga_2O_x.

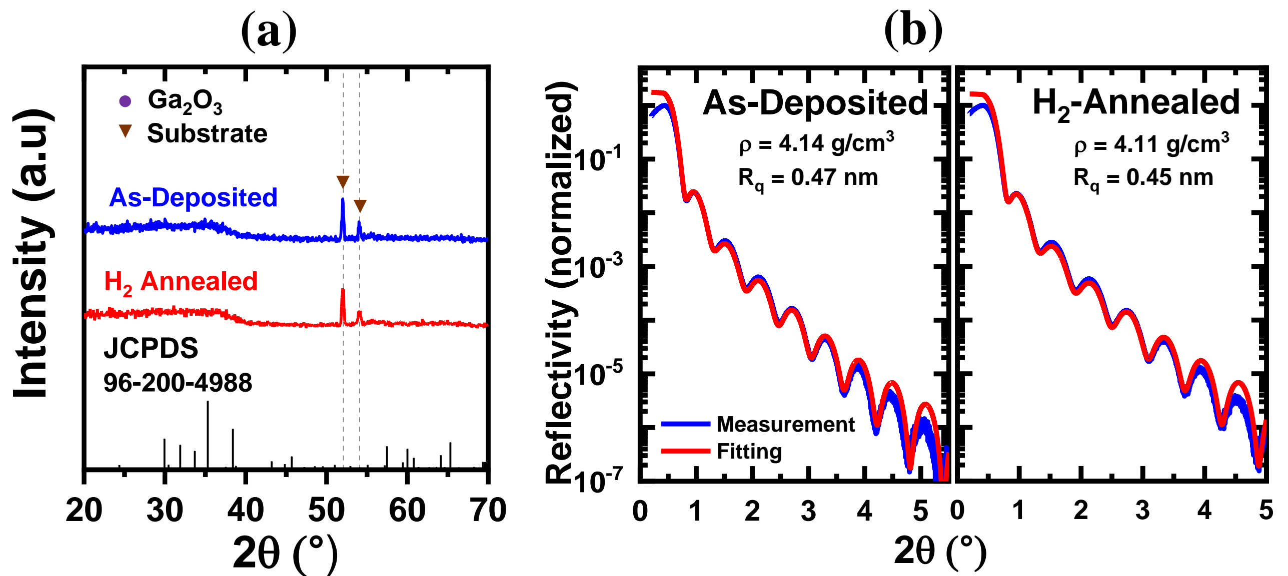

Figure 2.8. (a) XRD spectra and (b) XRR spectra of as-deposited and H_2-annealed Gallium Oxide films.

To look deeper into the structural differences between as-deposited and H_2-annealed a-Ga_2O_x films, the X-ray reflectometry (XRR) measurement was performed. The XRR oscillation pattern of as-deposited and H_2-annealed a-Ga_2O_x films are shown in ***Figure 2.8***b. The film thickness, film density, and film roughness were fitted and estimated based on the oscillation pattern. The values of as-deposited a-Ga_2O_x film thickness, film density and film roughness are 20.6 nm, 4.14 g/cm^3, and 0.47 nm respectively. Similar values were obtained for H_2-annealed a-Ga_2O_x at 21.0 nm, 4.11 g/cm^3, and 0.45 nm respectively (***Table 2-3***). This means that the H_2-annealing treatment did not change the structural characteristics of as-deposited a-Ga_2O_x. The hydrogenated a-Ga_2O_x films have relatively smooth surface which is ideal for TFT devices. The smooth surface tends to suppress the interfacial traps which implies better TFT device performance [25]. The detail on the as-deposited and H_2-annealed a-Ga_2O_x TFT characteristics will be discussed in section 2.4.2.

The optical bandgap and transparency of a-Ga_2O_x films before and after H_2 annealing was estimated by Tauc plot of UV-Visible spectra as displayed in ***Figure 2.9***. The red shift of optical bandgap (E_g) was observed from 4.80 eV (as-deposited) to 4.22 eV (H_2-annealed) which probably owing to annealing and/or hydrogen doping introduction [7]. To further investigate the main factors on this red shift phenomena, additional experiment to separate the effect of annealing temperature and annealing gases ambient will be discussed in section 2.5. Regardless the E_g values, those values confirmed that the a-Ga_2O_x is an ultra-wide bandgap material, despite being treated *via* H_2 annealing. The unique characteristic of ultra-wide bandgap material is its excellent transparency. In particular, a-Ga_2O_x has film transparency of >96% in the visible region (wavelength of 555 nm) which is a good candidate for transparent devices. The film characteristics of as-deposited and H_2-annealed films were summarized in ***Table 2-3***.

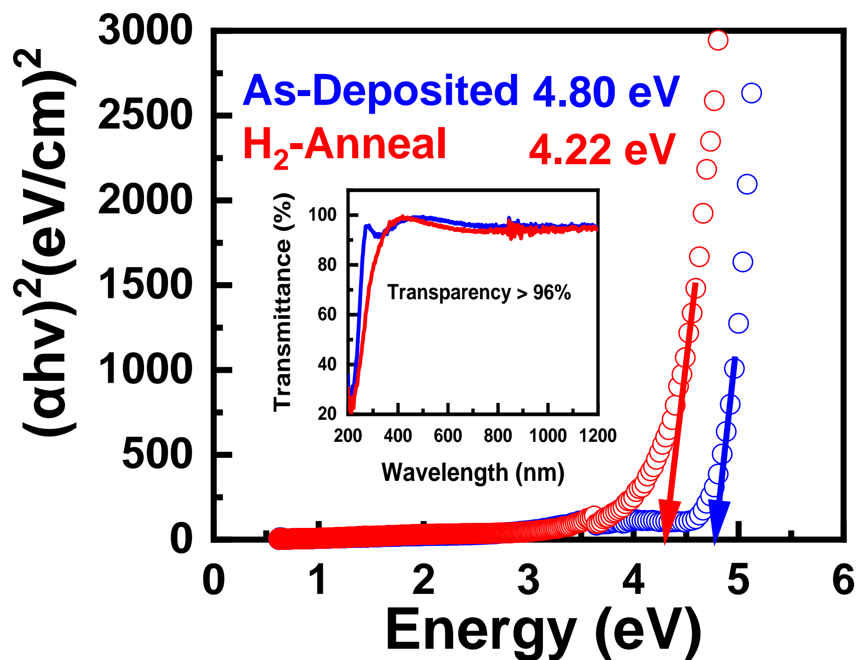

Figure 2.9. Optical bandgap and transmittance (inset) of as-deposited (blue) and H_2-annealed (red) a-Ga_2O_x films.

2.4.2 TFT characteristics

In the previous section, the characteristics of a-Ga_2O_x films were confirmed to as amorphous ultra-wide bandgap material. As mentioned in section 2.1, the combination of amorphous structure and ultra-wide bandgap material has severe difficulties in obtaining the electron conduction. This is caused by insufficient carrier concentration of as-deposited a-

Ga_2O_x [1]. As displayed in ***Figure 2.10***, the transfer characteristics of as-deposited solution-processed a-Ga_2O_x TFT is completely inactive. The complex combination of amorphous phase structure, ultra-wide bandgap material, and poor carrier concentration hinder electron mobility.

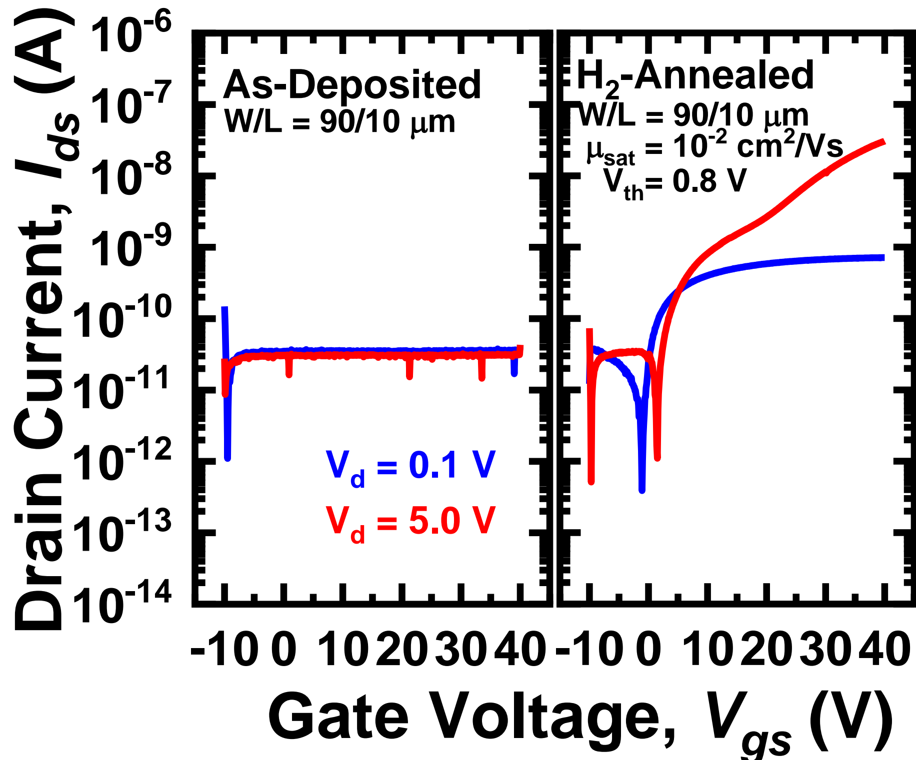

Figure 2.10. Transfer curves of as-deposited (left) and H_2-annealed (right) a-Ga_2O_x TFTs.

Interestingly, adding 4% H_2 gas significantly increases the carrier concentration by 1 order of magnitude (***Table 2-3***) which leads to conductivity improvement. As the conductivity increases, the a-Ga_2O_x film was transformed from insulator to semiconductor. Stacking the semiconducting a-Ga_2O_x film as an active channel in TFT structure which illustrated in ***Figure 2.6***, will eventually exhibits switching behavior as displayed in ***Figure 2.10***.

Table 2-3. Summary of as-deposited and H_2-annealed a-Ga_2O_x film characteristics.

Sample	Thickness (nm)	Roughness (nm)	Film density (g/cm^3)	E_g (eV)	Transparency (T_{555nm} in %)	Carrier density (cm^{-3})
As-deposited	20.6	0.47	4.14	4.80	98.62	1×10^{10}
H_2-annealed	21.0	0.45	4.11	4.22	96.14	6×10^{11}

In addition, the ON curve was successfully obtained at extremely lower drain voltage (V_d) $\leq$ 9.9 V unlike other reported a-Ga_2O_x TFTs which require higher V_d up to 50V [9][10]. This achievement of semiconducting solution-processed ultra-wide bandgap a-Ga_2O_x which was obtained from H_2-annealing need to be understood since it retained its amorphous structure even after annealing. To further understood the mechanism behind this improvement, the ambient gases were varied while maintaining the annealing temperature at 500 °C. The film characteristics as well as the TFT performance of this variations will be discussed in section 2.5.

2.5 The effect of annealing ambient gases to the a-Ga_2O_x film characteristics

Previous chapter reveals a superb research achievement by obtaining semiconducting behavior of the most challenging material, solution-processed ultra-wide bandgap a-Ga_2O_x. This improvement might be caused by either hydrogen doping [17][28][29] and/or annealing [37]. Aside from hydrogen doping which was explained in section 2.3.2, Yadav *et al.* (2020) demonstrated the effect of annealing temperature to the electrical properties of Ga_2O_3 films. As the annealing temperature increased from room temperature to 800 °C, the oxygen deficiency was generated. Thus, the free carrier concentration was also increased. Furthermore, bandgap narrowing and Fermi level shifting phenomena were also observed [37]. At high temperature, many body interactions between carriers in the conduction band and valence band were increased. This phenomenon is also known as bandgap renormalization where the bandgap narrows as the temperature increases [38].

To further study the main cause of this improvement, different gas environment was flowed during annealing while maintaining the temperature at 500°C. This experiment was performed to separate the effect of annealing gases (particularly H_2 gas) and annealing temperature.

2.5.1 Thin film deposition and sample preparation

The a-Ga_2O_x films were prepared for various characterizations to evaluate the structural, optical, and chemical properties of the untreated and treated-films. The fabrication steps were similar to ***Figure 2.6*** in section 2.3.3.2. Prior to the deposition, the Si/SiO_2 (p++) substrate and

glass substrate were cleaned and exposed by UV/O_3 treatment. The a-Ga_2O_x film was deposited *via* spin coating technique at 2000 rpm for 15 s followed by 2-step baking process at 150°C and 500 °C, 5 mins each. The final post-baking was done for 1 h. Afterwards, the a-Ga_2O_x film was annealed at 500 °C for 2 h under various annealing condition as displayed in ***Table 2-4***.

Film thickness, phase structure, and film density were characterized and determined by profilometer, grazing incidence X-ray diffraction (XRD; Rigaku SmartLab9kW/IP/HY/N), and X-ray reflectivity spectroscopy (XRR; Rigaku SmartLab9kW/IP/HY/N), respectively. Optical bandgap values (E_g) and Valence band offset ($E_{V\text{-offset}}$) were estimated by ultraviolet-visible spectroscopy (UV-Vis; JASCO ILN-472) Tauc plot and X-ray photoemission spectroscopy (XPS; ULVAC-PHI 5000 VersaProbell). Finally, elemental analysis and hydrogen diffusion were evaluated by secondary ion mass spectroscopy (SIMS; ULVAC-PHI ADEPT-1010). The film characteristics will be discussed in the next section.

Table 2-4. Summary of deposition parameters of untreated and treated a-Ga_2O_x films.

Sample	Temperature (°C)	Gases	Flowrate (sccm)	Time (h)
As-deposited		No annealing		
N_2-annealed	500	N_2 (100%)	500	2
H_2-annealed	500	N_2:H_2 (96:4%)	500	2
ATM-annealed	500	N_2:O_2 (80:20%)	500	2

2.5.2 Film characteristics

The phase structural properties of the untreated and treated Gallium Oxide films on Si/SiO_2 substrates were examined by using grazing incidence X-ray diffraction (XRD) analysis as displayed in ***Figure 2.11***. As-deposited a-Ga_2O_x was confirmed as amorphous which was also explained in the previous section. When the film was annealed at 500 °C in pure nitrogen ambient (N_2 gas 100%), the film was remained as an amorphous. This result emphasize that annealing gas ambient and annealing temperature did not induce film crystallization. Similar amorphous pattern was also observed for the film annealed under 4% H_2 gas ambient (N_2:H_2 96:4%). Interestingly, when the O_2 gas was introduced, the film started to crystallize. The mixture of N_2:O_2 gases which referred as atmospheric (ATM) annealing, exhibits several peaks of monoclinic crystalline gallium oxide (c-Ga_2O_3). Likely, the O_2 gas encourages Ga – O bond rearrangement which further initiate film crystallization. Nonetheless, incomplete

crystallization might have occurred because the film was annealed under crystallization temperature (Tc = 680 °C). By only annealing the film at 500 °C (without O_2 gas induced), the crystallized film will generally not be obtained. In the ATM-annealed film, the c-Ga_2O_3 structure existed amidst the a-Ga_2O_x structure, named as polycrystalline Gallium Oxide (poly-Ga_2O_3). Eventually, the XRD result suggests that the film crystallization is mainly dependent on the annealing ambient gases instead of the annealing temperature. The effect of both parameters was clearly observed.

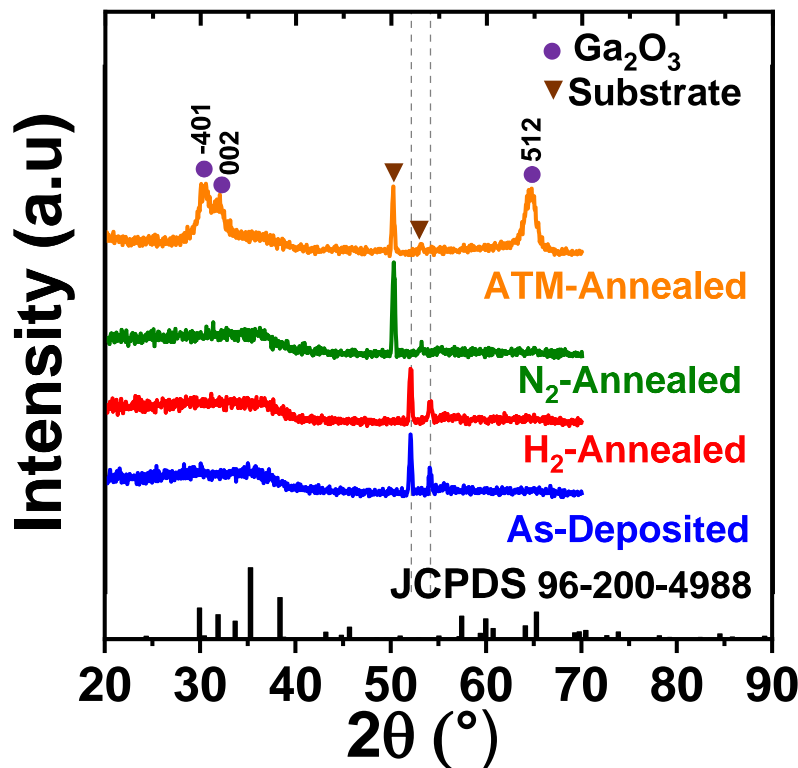

Figure 2.11. XRD spectra of untreated and treated a-Ga_2O_x films.

Furthermore, as the film was crystallized, the film density increases from 4.11 g/cm^3 to 5.13 g/cm^3 as summarized in ***Table 2-5***. In general, denser film tends to suppress the electron trap formation which further improves the electrical properties of a-Ga_2O_x film [1]. In this study, most film has relatively low film density of 4.1 – 4.2 g/cm^3 except the ATM-annealed film (5.1 g/cm^3). This is mainly caused by oxygen-driven crystallization which only occurred in the ATM-annealed film, as mentioned above. In consequence, this result highlighted the severe difference of the amorphous and polycrystalline Gallium Oxide film densities. The amorphous films have relatively ~ 1 g/cm^3 lower film density than the polycrystalline film.

Studies on the film density dependence of various Gallium Oxide film was summarized in

Table 2-6. Various Gallium Oxide film densities which were deposited *via* solution and vacuum deposition technique were reported. It showed that the solution-deposited film has relatively ~ 1 g/cm^3 lower film density than vacuum-deposited film. Kim *et al.* in 2017 reported the dependency of the film density on the conductivity. It was reported that the electrical conductivity increases exponentially with the increase in the film density. The minimum film density to obtain semiconducting a-Ga_2O_x is 5.2 g/cm^3 [1]. Despite the value (5.2 g/cm^3) being close to the ATM-annealed film density (5.1 g/cm^3), the ATM annealing treatment could not retain the amorphous nature of a-Ga_2O_x. Moreover, regardless of low film density of H_2-annealed film (4.11 g/cm^3), the H_2-annealed TFT showed excellent electrical characteristics improvement as mentioned in the previous section. Hence, there might be another reason to explain this improvement aside from the annealing temperature dependency. In particular, this improvement might be related to the presence of H_2 gas.

Table 2-5. Physical and optical properties of untreated and treated a-Ga_2O_x films.

Annealing ambient	**Thickness (nm)**	**Roughness (nm)**	**Film density (g/cm^3)**	**Phase structure**	**E_u (meV)**	**E_g (eV)**
As-deposited	20.6	0.47	4.14	a-Ga_2O_x	362.2	4.80
ATM-annealed	20.7	0.70	5.13	poly-Ga_2O_3	468.1	4.66
H_2-annealed	21.0	0.45	4.11	a-Ga_2O_x	746.9	4.22
N_2-annealed	22.0	0.50	4.17	a-Ga_2O_x	388.1	4.60

Table 2-6. Film density of solution-deposited and vacuum-deposited Gallium Oxide films.

AOS Material	**Dopant**	**Deposition**	**Film density (g/cm^3)**	**Ref.**
a-Ga_2O_x	-	solution	4.14	This work
a-Ga_2O_x	H_2	solution	4.11	This work
a-Ga_2O_x	B	solution	~4.8	[39]
a-Ga_2O_x	InZn	solution	~4.2	[40]
a-Ga_2O_x	-	vacuum	~5.2	[1]
c-Ga_2O_3	-	vacuum	~5.3	[41]
a-Ga_2O_x	-	vacuum	~6.0	[42]
c-Ga_2O_3	-	vacuum	~6.3	[42]

To further elucidate the electrical characteristics improvement of H_2-annealed sample, the optical properties such as optical bandgap (E_g), Fermi level (E_F) and Urbach energy (E_u) of each film were calculated from the UV-Vis and XPS spectra. The optical bandgap of direct bandgap was obtained through the Tauc equation:

$$(\alpha h\nu)^2 = A\,(h\nu - E_g) \quad \textbf{(2.1)}$$

where α is absorption coefficient, A is constant slope parameter, $h\nu$ is photon energy, and E_g is bandgap energy. Whereas the Fermi level (E_F) relative position and Urbach energy (E_u) were calculated using the following equation:

$$E_F = E_g - E_{V-offset} \quad \textbf{(2.2)}$$

$$\alpha = A\,exp\left(\frac{h\nu}{E_u}\right) \quad \textbf{(2.3)}$$

Where E_F is Fermi level relative position to the conduction band, E_g is bandgap energy which estimated from UV-Vis Tauc's plot, and $E_{V-offset}$ is Valence band offset which is estimated from XPS spectra at lower binding energy (0 – 10 eV), α is absorption coefficient, A is constant slope parameter, $h\nu$ is photon energy, and E_u is Urbach energy. The detail on the Fermi level estimation through UV-Vis and XPS spectra will be discussed in Chapter 4.

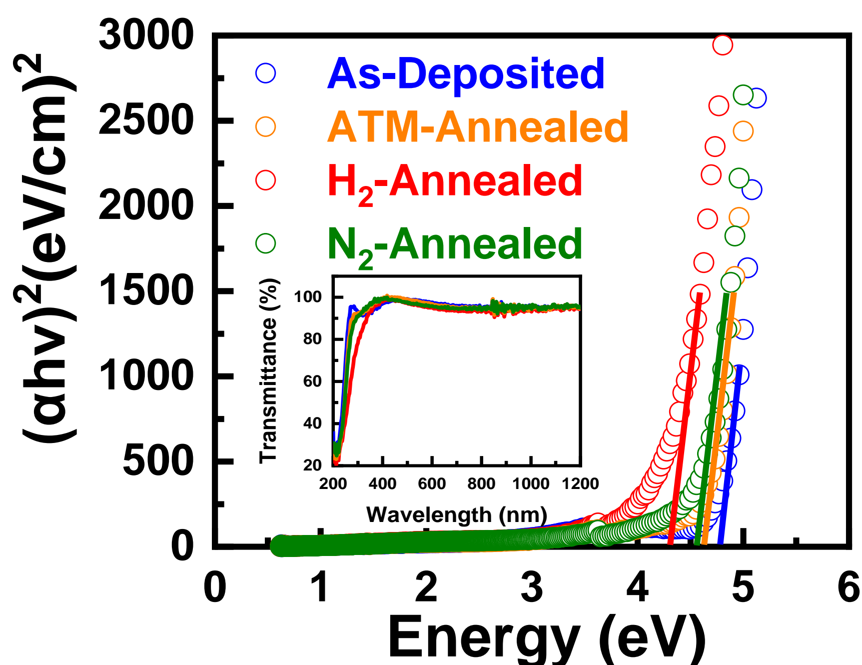

Figure 2.12. Optical bandgap and transmittance (inset) of untreated and treated a-Ga_2O_x films.

Figure 2.12 displayed the optical bandgap (E_g) of untreated and treated a-Ga_2O_x films. The optical and physical characteristics of those films were also summarized in ***Table 2-5***. It was observed that the E_g was shifted from 4.80 to 4.22 eV as different annealing ambient was applied. In particular, the E_g was shifted from 4.80 eV to 4.60 eV as the film was annealed at 500 °C in pure nitrogen ambient. This red shift phenomenon is mainly caused by the applied annealing temperature which encourage bandgap renormalization as mentioned above. As the temperature increases, the E_g narrows [38]. Moreover, the bandgap renormalization phenomenon was also observed on the ATM-annealed film where the E_g was narrowed to be 4.66 eV.

Interestingly, as 4% H_2 gas was introduced, the E_g was shifted even lower up to 4.22 eV. The large reduction in the E_g was mainly caused by hydrogen doping. As the dopant was incorporated to the oxide film, the E_g was narrowed owing to carrier concentration improvement [7][25]. In this case, the H_2 gas which continuously flowed was diffused and incorporated into a-Ga_2O_x bulk film, which further increased the carrier concentration and observed as E_g narrowing.

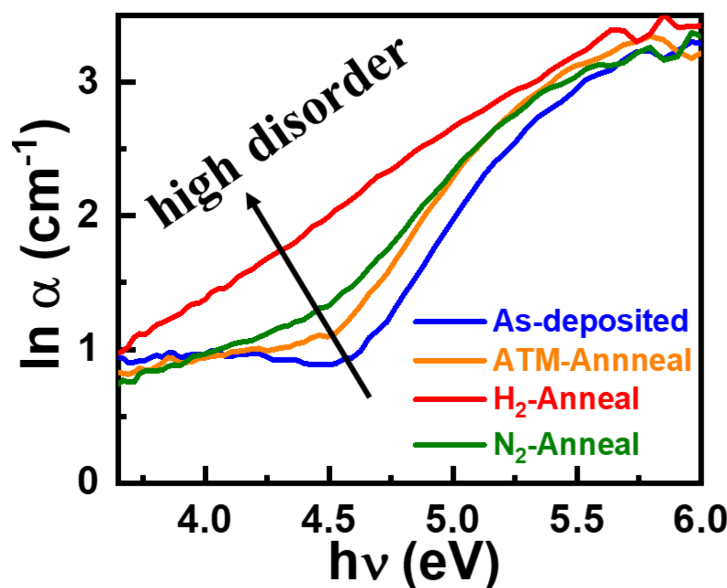

Figure 2.13. Optical absorption of untreated and treated a-Ga_2O_x films.

Hereafter, the Urbach energy (E_u) was also evaluated. The E_u indicates the subgap disorder level of oxide materials which might have originated from low/poor crystallinity, amorphous disorder, and defect impurity. Its value is the combination of both conduction band and valence band tail states. As showed in ***Table 2-5***, the E_u value was increased from 362.2 meV to 746.9

meV. In general, the amorphous nature has a random structure which contributes to subgap disorder of oxide materials. Likewise, the annealing treatments (N_2, H_2, and ATM annealing) tends to rearrange the a-Ga_2O_x structure uncontrollably, which might also be another origin of subgap disorder.

In case of N_2-annealed film, the subgap disorder mainly originated from the annealing temperature. As the a-Ga_2O_x film was annealed at 500 °C (100% N_2), the heat induced band rearrangement but insufficient to form a crystalline phase. Thus, the randomness of the amorphous structure increased which further increase the E_u (388.1 meV) as well. In contrast, the oxygen-driven crystallization transformed the a-Ga_2O_x to be poly-Ga_2O_3 under ATM annealing condition. The presence of crystalline structure amidst amorphous structure result in poor crystallinity which added subgap disorder in the bulk film. In other words, the subgap disorder of ATM-annealed film originated from annealing temperature and its poor crystallinity. Although crystalline structure tends to have relatively low E_u, unfortunately poly-Ga_2O_3 has relatively high Eu of 468.1 meV owing to incomplete crystallization which contributed to the increase of structure randomness.

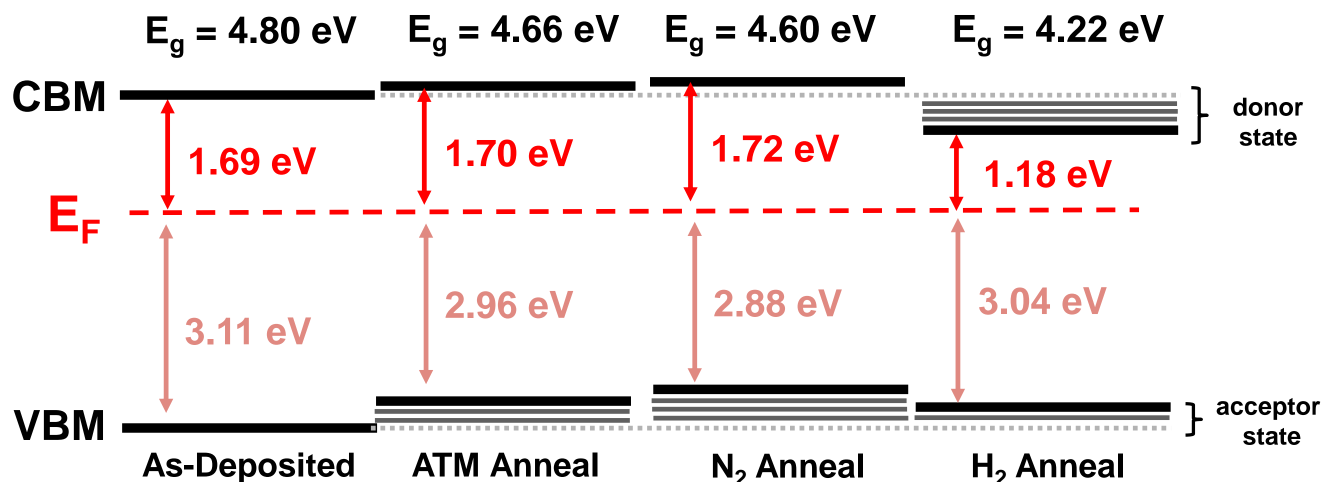

Figure 2.14. Band alignment of untreated and treated a-Ga_2O_x films.

Particularly, the H_2-annealed film has the highest subgap disorder of E_u = 746.9 meV. It might be caused by complex combination of amorphous disorder and defect impurity. In terms of amorphous disorder, the H_2-annealed film has the similar states to N_2-annealed film where the randomness of the structure was increased caused by annealing temperature. Its atomic bond was rearranged but did not crystallize. Nonetheless, the H_2-annealed film exhibit

extremely high E_u as compared to N_2-annealed film which mainly due to H_2 defect impurity. Apparently, the H_2 gas was diffused and was incorporated to the highly random H_2-annealed a-Ga_2O_x film.

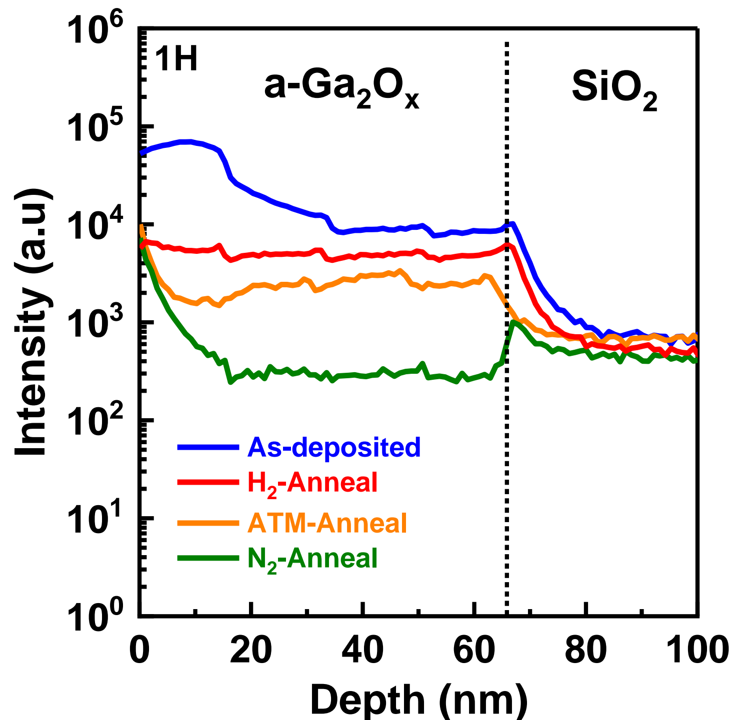

Figure 2.15. SIMS of untreated and treated a-Ga_2O_x films.

The presence of H_2-dopant was clearly observed as the high E_u value in ***Table 2-5*** and broad optical absorption showed in ***Figure 2.13***. Kamiya *et al.* reported that wider optical absorption of a-IGZO film indicates the higher subgap disorder [43]. Those subgap disorder tends to create tail states in the bandgap edges. In amorphous oxide semiconductor such as a-IGZO and a-Ga_2O_x, the energy width of valence tail states is larger than conduction tail states, implying that the E_u better represents the valence tail states [1][43]. Hence, additional acceptor states were created above valence band maximum. Nevertheless, in this study, the additional donor states tend to be created rather than acceptor states particularly for H_2-annealed film. This is because the H_2 gas serves as a shallow donor which increased the carrier concentration and reflected as a switching TFT (***Figure 2.10***). Therefore, additional donor states were created specifically only for H_2-annealed sample. As illustrated in ***Figure 2.14***, the additional acceptor states were created for ATM-annealed and N_2-annealed films which further narrowed the E_g as compared to the as-deposited film. While for H_2-annealed film, the minimum acceptor states were created

and dominant donor states were also created. This result reveals the presence of H_2-dopant as a shallow donor which occupied donor states and narrowed the E_g. The detail on the E_g narrowing as well as E_F shifting phenomena will be discussed in section 2.7.

To support the hypothesis, SIMS measurement was conducted to further investigate the H-incorporation. In particular, the H intensity was gradually decreased for H_2-annealed, ATM-annealed and N_2-annealed respectively as shown in ***Figure 2.16***. The detected H intensity might indicate either H-impurities or H-incorporated. H-impurity originated from the precursor-related impurity or H_2O environment impurity (relative humidity) which might be trapped to the film during solution deposition. While the H-incorporated refers to the H_2 gas which were incorporated to the film during H_2 annealing. However, it is quite difficult to distinguish which H contributed more.

In particular, the as-deposited film has the highest hydrogen intensity which eventually reduced after annealing treatment was applied (H_2 annealing, N_2 annealing, and ATM annealing respectively). It suggests that the as-deposited film contains excess water (H-impurities) which might be trapped during film formation. As the film was annealed under 100% N_2 ambient, those H-impurities were evaporated which observed as H intensity decreased in SIMS spectra. Interestingly, the H intensity was increase as 4% hydrogen was introduced which confirm that the H was incorporated and serves as a shallow donor.

2.6 a-Ga_2O_x TFTs performance under different annealing ambient gases

In the previous chapter, the effect of annealing gases ambient and annealing temperature to the a-Ga_2O_x films has been clearly discussed. The effect of both parameters was clearly observed and separated. In this chapter, the TFT performance of untreated and treated a-Ga_2O_x film will be further discussed.

2.6.1 Device fabrication

The a-Ga_2O_x TFTs fabrication steps were similar to ***Figure 2.6*** in section 2.3.3.2, and film preparation in section 2.5.1. In advance, the annealing treatments were performed after channel-islands of a-Ga_2O_x were patterned. This is because the annealing treatments somehow modified film characteristics which further affected the wet etching rate. Uncontrolled etching rate will cause under-etching or over-etching which brings another issue to the TFTs

characteristics. In addition, applying the annealing treatments after electrode deposition will bring additional issue such as electrode damage. The H_2 gas might diffuse to the Al electrode and form Al:H or damage the electrode thin-film. In contrast, the O_2 might also diffuse and promote oxidation, creating AlO_x. Thus, the films were etched at the same state condition: as-deposited. Afterwards, the a-Ga_2O_x film was annealed at 500 °C for 2 h under various annealing condition as displayed in ***Table 2-4***. And eventually, bottom-gate top-contact a-Ga_2O_x TFTs were fabricated by depositing 100-nm-thick Aluminum as source/drain electrodes *via* electron beam evaporation.

2.6.2 TFT characteristics

The transfer characteristics of a-Ga_2O_x TFTs are displayed in ***Figure 2.17***. The transfer characteristics of as-deposited solution-processed a-Ga_2O_x TFT is completely inactive. There was no switching behavior observed due to insufficient carrier concentration. The complex combination of amorphous phase structure, ultra-wide bandgap (E_g = 4.8 eV), and low carrier density (1×10^{10} cm^{-1}) hinder electron mobility. In addition, the as-deposited a-Ga_2O_x has relatively high trap states owing to high oxygen vacancy and low film density as mentioned in the previous section. The TFT performance of solution-processed ultra-wide bandgap Gallium Oxide was summarized in ***Table 2-7***.

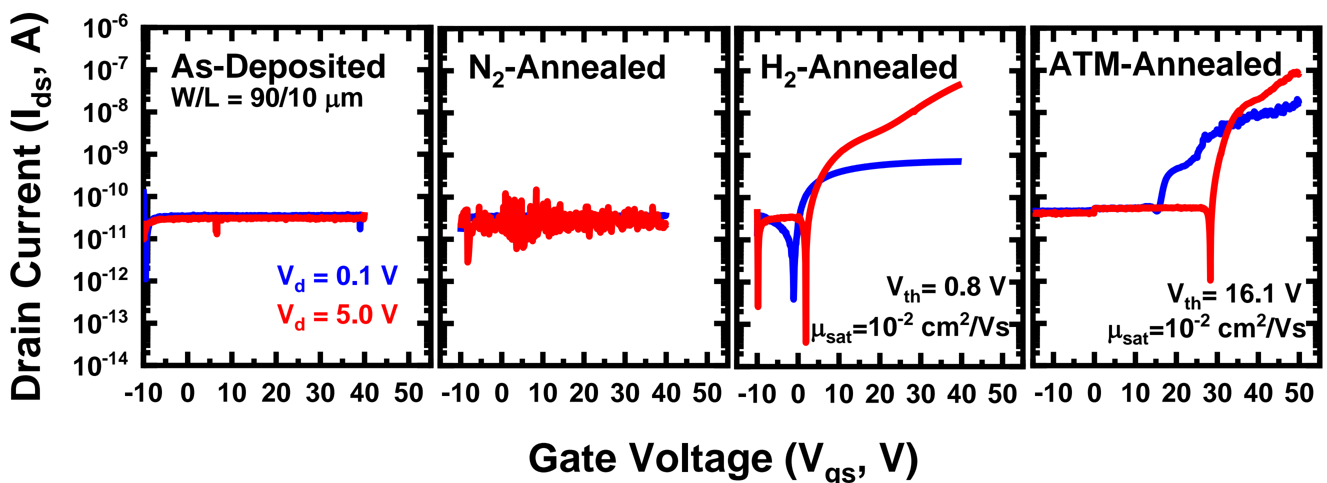

Figure 2.17. Transfer characteristics of untreated and treated a-Ga_2O_x TFTs.

When the film was annealed at 500 °C in pure nitrogen gas ambient (N_2 gas 100%), there was no severe changes observed in the optical, chemical and electrical properties. Particularly,

there was no changes in the TFT characteristic (***Figure 2.17***). This is because the N_2 is an inert gas which is not reactive and widely used to protect the electronic devices performance from degradation. The dissociation energy of N_2 molecules is fairly high (9.756 eV)[44]. Thus, high energy was needed to break those bonds. Apparently, 500 °C is insufficient to break the N_2 bonds. Therefore, there was no N_2 which diffused to the film which was also confirmed by XPS and SIMS measurement. In addition, this temperature was also insufficient to crystallize the a-Ga_2O_x films. Instead, it was only enough to rearrange the Ga – O bonds. Moreover, the E_u of the N_2-annealed film was increased as compared to the as-deposited film, owing to bond rearrangement without film crystallization. Hence, in the N_2 annealing treatment, the temperature of 500 °C mainly caused minimum film modification to the N_2-annealed film.

Furthermore, as 4% H_2 gas was added, significant film and TFT device improvements were observed. The H_2 serves as a shallow donor which occupies donor states near the conduction band. Likewise, the H_2 passivated the trap states which exist on the as-deposited film. As a result, the carrier density was improved which implies conductivity improvement as well. Thus, the switching behavior was observed on the H_2-annealed TFTs.

Table 2-7. Summary of Gallium Oxide TFT performance

Annealing ambient	**Gases**	μ_{sat} **(cm²/Vs)**	V_{th} **(V)**	**SS (V/dec)**	**ON/OFF ratio**
As-deposited	No annealing	No switching			
ATM-annealed	N_2:O_2 (78:21%)	$(7.6 \pm 0.9) \times 10^{-2}$	13.0 ± 2.8	0.16 ± 0.07	~10^4
H_2-annealed	N_2:H_2 (96:4%)	$(1.0 \pm 0.01) \times 10^{-2}$	1.7 ± 0.2	0.34 ± 0.20	~10^4
N_2-annealed	N_2 (100%)	No switching			

While for the ATM-annealed TFT, the switching behavior was mainly caused by the film crystallization. As the 500 °C was insufficient to modify the a-Ga_2O_x film, the O_2 gas modified the film characteristics as well as the TFT performance. The ATM-annealed film has higher density which implies lower trap states and further improved the TFT performance [1]. This is probably the main reason why the TFT switching behavior is observed in ***Figure 2.17***. However, the poly-Ga_2O_3 was formed which implies higher interface roughness. Thus, although the trap states in the bulk was reduced as the film density increased, another trap were

created in the interface (either channel-gate insulator interface or channel-source/drain interface) due to relatively high surface roughness. The presence of interfacial traps will further deteriorate the device performance [45]. Likewise, the charge trapping of the n-type semiconductor at the interface tends to shift the V_{th} positively.

2.7 Mechanism on the electrical characteristic improvement of a-Ga_2O_x TFTs

Figure 2.18 illustrates the schematic diagram of a-Ga_2O_x material conversion. The a-Ga_2O_x has an amorphous nature, ultra-wide bandgap (E_g = 4.8 eV), and low carrier density (1×10^{10} cm^{-3}) which hinder electron mobility. The Ga – O was loosely bounded and the interatomic distance was relatively high. This assumption is based on the fact that the as-deposited a-Ga_2O_x has relatively low Ga – O bond, high oxygen vacancy and low film density. Likewise, the a-Ga_2O_x has excessively high traps states which implies poor TFT performance.

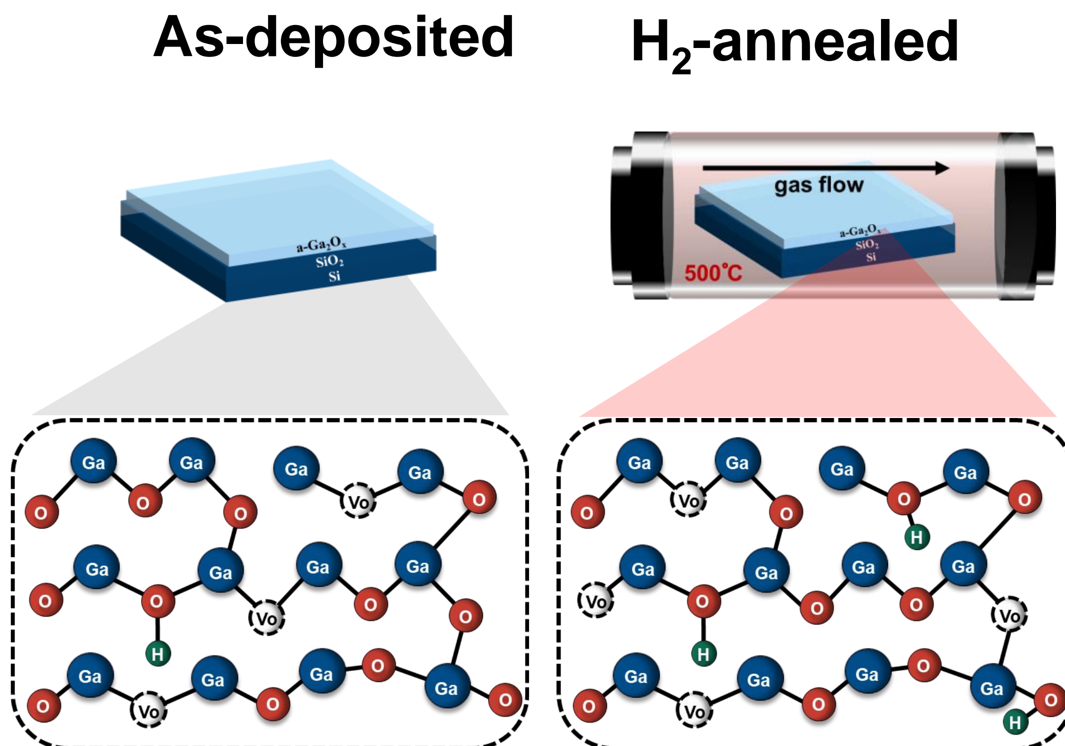

Figure 2.18. Schematic diagram of insulator-to-semiconductor conversion of solution-processed ultra-wide bandgap a-Ga_2O_x via H_2 annaling.

Once the film was annealed at 500 °C in 4% H_2 gas ambient, the H-dopant was introduced. The H_2 gas was diffused and was incorporated into the a-Ga_2O_x film. The H-incorporated serves as a shallow donor which occupies donor states near the conduction band and further increase the carrier density of 1 order magnitude (6×10^{11} cm^{-3}). In addition, the H-incorporated passivated the trap states of the as-deposited film. Eventually, the film conductivity was improved which reflected as TFT switching behavior.

2.7.1 H-doping mechanism

In general, the as-deposited a-Ga_2O_x has relatively high hydrogen impurities (H-impurities, H-imp.). Excessively high amounts of H-impurities create interstitial defects which further deteriorate the device performance [25]. As annealing was applied, the impurities were evaporated which was indicated by the ~10% decrease of Ga-OH percentage area in N_2-annealed sample (**Error! Reference source not found.**). Regardless of the N_2 gases, the applied t emperature mainly caused the H-impurities evaporation. Simultaneously, as 4% H_2 gas was introduced, the Ga-OH percentage area was increased by ~5% (H_2-annealed sample). It emphasizes that the H_2 gas which flowed during annealing was diffused and incorporated into a-Ga_2O_x film which further serve as shallow donor. At certain amounts, H acts as a shallow donor which is reflected in the switching of the H_2-annealed a-Ga_2O_x TFT. The H_2 gas (H^+ atom) binds to an oxygen creating O – H bond and serves as shallow donor in a-Ga_2O_x [46]. However, excessive H tends to creates interstitial defect, while lower H might refer to insufficient carrier concentration. Therefore, controlling the H percentage is crucial.

2.7.2 E_F shifting phenomena

An attractive phenomenon was observed as the a-Ga_2O_x was treated in various annealing gas ambient. In the previous section, the role of H_2-dopant as a shallow donor and defect passivator were discussed. As the H_2 gas was diffused and incorporated, the E_g as well as the E_F were decreased as displayed in ***Figure 2.19***. The reduction in the E_g was mainly due to carrier concentration induced by hydrogen doping. The hydrogen acts as a shallow donor which occupied donor level. Those electron carriers create additional states below conduction band minimum (CBM) and further shift E_F close to the CBM [7][25]. The E_F shifting phenomena implies electrical properties improvement. Nevertheless, the H-incorporated is implanted at considerable amount since excess H-incorporated tends to create interstitial defects. Apparently,

the E_F relative position to the CBM is a key strategy in enhancing the electrical properties of n-type semiconductors. The detail on the E_F engineering will be discussed in Chapter 4.

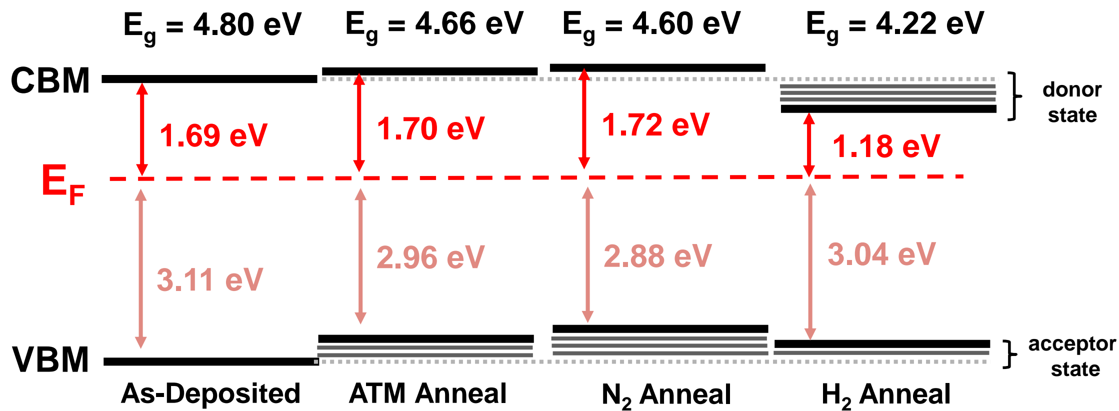

Figure 2.19. Band diagram of untreated and treated a-Ga_2O_x films.

2.8 Summary

In summary, the first demonstration of insulator-to-semiconductor conversion of solution-processed ultra-wide bandgap a-Ga_2O_x (E_g > 4.8 eV) has been successfully achieved. It was found that performing H_2 annealing at 500°C induced hydrogen incorporation which further serves as a shallow donor in insulating a-Ga_2O_x. The hydrogen incorporation leads to an increase in electron carrier concentration as reflected by E_F shifting closer to the CBM (1.18 eV). By applying H_2-annealing, semiconducting behavior of solution-processed a-Ga_2O_x was successfully achieved with excellent film quality and considerable TFT device performance. Likewise, by referring ***Table 1 – 4***, it can clearly observe that this result is comparable to the vacuum deposited counterpart. The H_2 annealing is a promising method which can be used to enhance other ultra-wide bandgap oxide materials.

2.9 References

[1] J. Kim, T. Sekiya, N. Miyokawa, N. Watanabe, K. Kimoto, K. Ide, Y. Toda, S. Ueda, N. Ohashi, H. Hiramatsu, H. Hosono, and T. Kamiya, “Conversion of an ultra-wide bandgap amorphous oxide insulator to a semiconductor,” *NPG Asia Mater.*, vol. 9, no. 3, 2017, doi: 10.1038/am.2017.20.

[2] D. C. Corsino, J. P. S. Bermundo, C. Kulchaisit, M. N. Fujii, Y. Ishikawa, H. Ikenoue, and Y. Uraoka, “High-Performance Fully Solution-Processed Oxide Thin-Film Transistors via Photo-Assisted Role Tuning of InZnO,” *ACS Appl. Electron. Mater.*, vol. 2, no. 8, pp. 2398–2407, 2020, doi: 10.1021/acsaelm.0c00348.

[3] W. Xu, H. Li, J. Bin Xu, and L. Wang, “Recent Advances of Solution-Processed Metal Oxide Thin-Film Transistors,” *ACS Appl. Mater. Interfaces*, vol. 10, no. 31, pp. 25878–25901, 2018, doi: 10.1021/acsami.7b16010.

[4] S. J. Pearton, J. Yang, P. H. Cary IV, F. Ren, J. Kim, M. J. Tadjer, and M. A. Mastro, “A review of Ga2O3 materials, processing, and devices,” *Appl. Phys. Rev.*, vol. 5, p. 011301, 2018.

[5] H. Liang, Z. Han, and Z. Mei, “Recent Progress of Deep Ultraviolet Photodetectors using Amorphous Gallium Oxide Thin Films,” *Phys. Status Solidi Appl. Mater. Sci.*, vol. 218, no. 1, p. 2000339, Jan. 2021, doi: 10.1002/pssa.202000339.

[6] X. Hou, X. Zhao, Y. Zhang, Z. Zhang, Y. Liu, Y. Qin, P. Tan, C. Chen, S. Yu, M. Ding, G. Xu, Q. Hu, and S. Long, “High-Performance Harsh-Environment-Resistant GaOX Solar-Blind Photodetectors via Defect and Doping Engineering,” *Adv. Mater.*, vol. 34, no. 1, pp. 1–11, 2022, doi: 10.1002/adma.202106923.

[7] D. Purnawati, J. P. Bermundo, and Y. Uraoka, “Insulator-to-semiconductor conversion of solution-processed ultra-wide bandgap amorphous gallium oxide via hydrogen annealing,” *Appl. Phys. Express*, vol. 15, no. 2, p. 24003, 2022, doi: 10.35848/1882-0786/ac466a.

[8] Z. Han, H. Liang, W. Huo, X. Zhu, X. Du, and Z. Mei, “Boosted UV Photodetection Performance in Chemically Etched Amorphous Ga2O3 Thin-Film Transistors,” *Adv. Opt. Mater.*, vol. 8, no. 8, Apr. 2020, doi: 10.1002/adom.201901833.

[9] Y. Qin, S. Long, Q. He, H. Dong, G. Jian, Y. Zhang, X. Hou, P. Tan, Z. Zhang, Y. Lu, C. Shan, J. Wang, W. Hu, H. Lv, Q. Liu, and M. Liu, “Amorphous Gallium Oxide-Based Gate-Tunable High-Performance Thin Film Phototransistor for Solar-Blind Imaging,” *Adv. Electron. Mater.*, vol. 5, no. 7, Jul. 2019, doi: 10.1002/aelm.201900389.

[10] L. Nagarajan, R. A. De Souza, D. Samuelis, I. Valov, A. Börger, J. Janek, K. D. Becker, P. C. Schmidt, and M. Martin, “A chemically driven insulator-metal transition in non-stoichiometric and amorphous gallium oxide,” *Nat. Mater.*, vol. 7, no. 5, pp. 391–398, 2008, doi: 10.1038/nmat2164.

[11] E. Yarali, C. Koutsiaki, H. Faber, K. Tetzner, E. Yengel, P. Patsalas, N. Kalfagiannis, D. C. Koutsogeorgis, and T. D. Anthopoulos, “Recent Progress in Photonic Processing of Metal-Oxide Transistors,” *Adv. Funct. Mater.*, vol. 30, no. 20, pp. 1–37, 2020, doi: 10.1002/adfm.201906022.

[12] K. Tetzner, Y. H. Lin, A. Regoutz, A. Seitkhan, D. J. Payne, and T. D. Anthopoulos, "Sub-second photonic processing of solution-deposited single layer and heterojunction metal oxide thin-film transistors using a high-power xenon flash lamp," *J. Mater. Chem. C*, vol. 5, no. 45, pp. 11724–11732, 2017, doi: 10.1039/c7tc03721j.

[13] C. M. Kang, H. Kim, Y. W. Oh, K. H. Baek, and L. M. Do, "High-Performance, Solution-Processed Indium-Oxide TFTs Using Rapid Flash Lamp Annealing," *IEEE Electron Device Lett.*, vol. 37, no. 5, pp. 595–598, 2016, doi: 10.1109/LED.2016.2545692.

[14] C. J. Moon and H. S. Kim, "Intense Pulsed Light Annealing Process of Indium-Gallium-Zinc-Oxide Semiconductors via Flash White Light Combined with Deep-UV and Near-Infrared Drying for High-Performance Thin-Film Transistors," *ACS Appl. Mater. Interfaces*, vol. 11, no. 14, pp. 13380–13388, 2019, doi: 10.1021/acsami.8b22458.

[15] I. W. Boyd and J. Y. Zhang, "Photo-induced large area growth of dielectrics with excimer lamps," *Mater. Res. Soc. Symp. - Proc.*, vol. 617, 2000, doi: 10.1557/proc-617-j4.4.

[16] W. Lee, S. Choi, K. T. Kim, J. Kang, S. K. Park, and Y. H. Kim, "Determination of insulator-to-semiconductor transition in sol-gel oxide semiconductors using derivative spectroscopy," *Materials (Basel).*, vol. 9, no. 1, pp. 1–9, 2016, doi: 10.3390/ma9010006.

[17] S. I. Oh, G. Choi, H. Hwang, W. Lu, and J. H. Jang, "Hydrogenated IGZO thin-film transistors using high-pressure hydrogen annealing," *IEEE Trans. Electron Devices*, vol. 60, no. 8, pp. 2537–2541, 2013, doi: 10.1109/TED.2013.2265326.

[18] A. Takagi, K. Nomura, H. Ohta, H. Yanagi, T. Kamiya, M. Hirano, and H. Hosono, "Carrier transport and electronic structure in amorphous oxide semiconductor, a-InGaZnO4," *Thin Solid Films*, vol. 486, no. 1–2, pp. 38–41, 2005, doi: 10.1016/j.tsf.2004.11.223.

[19] T. Kamiya, K. Nomura, and H. Hosono, "Origins of High Mobility and Low Operation Voltage of Amorphous Oxide TFTs: Electronic Structure, Electron Transport, Defects and Doping*," *J. Disp. Technol.*, vol. 5, no. 12, pp. 468–483, 2009, doi: 10.1109/jdt.2009.2034559.

[20] Y. Li, X. Hu, Z. Liu, and J. Ren, "Power and gas pressure effects on properties of amorphous In-Ga-ZnO films by magnetron sputtering," *J. Mater. Sci. Mater. Electron.*, vol. 23, no. 2, pp. 408–412, 2012, doi: 10.1007/s10854-011-0467-x.

[21] J. J. Dong, X. W. Zhang, J. B. You, P. F. Cai, Z. G. Yin, Q. An, X. B. Ma, P. Jin, Z. G. Wang, and P. K. Chu, "Effects of hydrogen plasma treatment on the electrical and optical properties of ZnO films: Identification of hydrogen donors in ZnO," *ACS Appl. Mater. Interfaces*, vol. 2, no. 6, pp. 1780–1784, 2010, doi: 10.1021/am100298p.

[22] A. Sato, M. Shimada, K. Abe, R. Hayashi, H. Kumomi, K. Nomura, T. Kamiya, M. Hirano, and H. Hosono, "Amorphous In-Ga-Zn-O thin-film transistor with coplanar homojunction structure," *Thin Solid Films*, vol. 518, no. 4, pp. 1309–1313, 2009, doi: 10.1016/j.tsf.2009.01.165.

[23] T. Toda, D. Wang, J. Jiang, M. P. Hung, and M. Furuta, "Quantitative analysis of the effect of hydrogen diffusion from silicon oxide etch-stopper layer into amorphous In-Ga-Zn-O on thin-film transistor," *IEEE Trans. Electron Devices*, vol. 61, no. 11, pp. 3762–3767, 2014, doi: 10.1109/TED.2014.2359739.

[24] S. W. Tsao, T. C. Chang, S. Y. Huang, M. C. Chen, S. C. Chen, C. T. Tsai, Y. J. Kuo, Y. C. Chen, and W. C. Wu, "Hydrogen-induced improvements in electrical characteristics of a-IGZO thin-film transistors," *Solid. State. Electron.*, vol. 54, no. 12, pp. 1497–1499, 2010, doi: 10.1016/j.sse.2010.08.001.

[25] J. Kim, S. Bang, S. Lee, S. Shin, J. Park, H. Seo, and H. Jeon, "A study on H 2 plasma treatment effect on a-IGZO thin film transistor," *J. Mater. Res.*, vol. 27, no. 17, pp. 2318–2325, 2012, doi: 10.1557/jmr.2012.199.

[26] C. H. Jung, D. J. Kim, Y. K. Kang, and D. H. Yoon, "Transparent amorphous In-Ga-Zn-O thin film as function of various gas flows for TFT applications," *Thin Solid Films*, vol. 517, no. 14, pp. 4078–4081, 2009, doi: 10.1016/j.tsf.2009.01.166.

[27] B. Du Ahn, H. S. Shin, H. J. Kim, J. S. Park, and J. K. Jeong, "Comparison of the effects of Ar and H2 plasmas on the performance of homojunctioned amorphous indium gallium zinc oxide thin film transistors," *Appl. Phys. Lett.*, vol. 93, no. 20, 2008, doi: 10.1063/1.3028340.

[28] W. K. Kim, S. Lee, Y. C. Cho, H. Koinuma, S. Y. Jeong, J. M. Shin, C. R. Cho, J. S. Bae, T. Y. Kim, and S. Park, "Stable high conductive amorphous InGaZnO driven by hydrogenation using hot isostatic pressing," *Appl. Phys. Lett.*, vol. 98, no. 12, pp. 1–4, 2011, doi: 10.1063/1.3567635.

[29] D. H. Son, D. H. Kim, S. J. Sung, E. A. Jung, and J. K. Kang, "High performance and the low voltage operating InGaZnO thin film transistor," *Curr. Appl. Phys.*, vol. 10, no. 4 SUPPL., pp. e157–e160, 2010, doi: 10.1016/j.cap.2010.03.012.

[30] K. Ide, K. Nomura, H. Hiramatsu, T. Kamiya, and H. Hosono, "Structural relaxation in amorphous oxide semiconductor, a-In-Ga-Zn-O," *J. Appl. Phys.*, vol. 111, no. 7, 2012, doi: 10.1063/1.3699372.

[31] J. Raja, K. Jang, H. H. Nguyen, T. T. Trinh, W. Choi, and J. Yi, "Enhancement of electrical stability of a-IGZO TFTs by improving the surface morphology and packing density of active channel," *Curr. Appl. Phys.*, vol. 13, no. 1, pp. 246–251, 2013, doi: 10.1016/j.cap.2012.07.016.

[32] J. Lee, H. Park, H. Choi, M. Hasan, M. Jo, M. Chang, B. H. Lee, C. S. Park, C. Y. Kang, and H. Hwang, "Modulation of TiSiN effective work function using high-pressure postmetallization annealing in dilute oxygen ambient," *Appl. Phys. Lett.*, vol. 92, no. 26, 2008, doi: 10.1063/1.2953192.

[33] S. J. Heo, D. H. Yoon, T. S. Jung, and H. J. Kim, "Recent advances in low-temperature solution-processed oxide backplanes," *J. Inf. Disp.*, vol. 14, no. 2, pp. 79–87, 2013, doi: 10.1080/15980316.2013.806274.

[34] E. Bacaksiz, M. Parlak, M. Tomakin, A. Özçelik, M. Karakiz, and M. Altunbaş, "The effects of zinc nitrate, zinc acetate and zinc chloride precursors on investigation of structural and optical properties of ZnO thin films," *J. Alloys Compd.*, vol. 466, no. 1–2, pp. 447–450, 2008, doi: 10.1016/j.jallcom.2007.11.061.

[35] W. H. Jeong, J. H. Bae, and H. J. Kim, "High-performance oxide thin-film transistors using a volatile nitrate precursor for low-temperature solution process," *IEEE Electron Device Lett.*, vol. 33, no. 1, pp. 68–70, 2012, doi: 10.1109/LED.2011.2173897.

[36] W. H. Jeong, J. H. Bae, K. M. Kim, D. L. Kim, Y. S. Rim, S. J. Kim, K.-B. Park, J.-B.

Seon, M.-K. Ryu, and H. J. Kim, "Solution-processed oxide thin-film transistors using aluminum and nitrate precursors for low-temperature annealing," *J. Soc. Inf. Disp.*, vol. 19, no. 9, p. 620, 2011, doi: 10.1889/jsid19.9.620.

[37] M. K. Yadav, A. Mondal, S. Das, S. K. Sharma, and A. Bag, "Impact of annealing temperature on band-alignment of PLD grown Ga2O3/Si (100) heterointerface," *J. Alloys Compd.*, vol. 819, p. 153052, 2020, doi: 10.1016/j.jallcom.2019.153052.

[38] J. W. Jeon, D. W. Jeon, T. Sahoo, M. Kim, J. H. Baek, J. L. Hoffman, N. S. Kim, and I. H. Lee, "Effect of annealing temperature on optical band-gap of amorphous indium zinc oxide film," *J. Alloys Compd.*, vol. 509, no. 41, pp. 10062–10065, 2011, doi: 10.1016/j.jallcom.2011.08.033.

[39] W. Xu, L. Chen, S. Han, P. Cao, M. Fang, W. Liu, D. Zhu, and Y. Lu, "Aqueous Solution-Processed Boron-Doped Gallium Oxide Dielectrics for High-Performance Thin-Film Transistors," *J. Phys. Chem. C*, vol. 124, no. 14, pp. 8015–8023, 2020, doi: 10.1021/acs.jpcc.0c01281.

[40] J. W. Na, Y. G. Kim, T. S. Jung, Y. J. Tak, S. P. Park, J. W. Park, S. J. Kim, and H. J. Kim, "Interface location-controlled indium gallium zinc oxide thin-film transistors using a solution process," *J. Phys. D. Appl. Phys.*, vol. 49, no. 8, 2016, doi: 10.1088/0022-3727/49/8/085301.

[41] R. O'Donoghue, J. Rechmann, M. Aghaee, D. Rogalla, H. W. Becker, M. Creatore, A. D. Wieck, and A. Devi, "Low temperature growth of gallium oxide thin films via plasma enhanced atomic layer deposition," *Dalt. Trans.*, vol. 46, no. 47, pp. 16551–16561, 2017, doi: 10.1039/c7dt03427j.

[42] Y. Chen, O. Sakata, H. Morita, A. Matsuda, F. Jia, O. Seo, L. Singgappulige, R. Kumara, T. Ina, E. Kobayashi, J. Kim, C. Song, S. Hiroi, N. Palina, Y. Lou, and W. Ren, "Applied Surface Science Electronic states of gallium oxide epitaxial thin films and related atomic arrangement," *Appl. Surf. Sci.*, vol. 578, p. 151943, 2022, doi: 10.1016/j.apsusc.2021.151943.

[43] T. Kamiya, K. Nomura, and H. Hosono, "Present status of amorphous In-Ga-Zn-O thin-film transistors," *Sci. Technol. Adv. Mater.*, vol. 11, no. 4, 2010, doi: 10.1088/1468-6996/11/4/044305.

[44] D. C. Frost and C. A. Mcdowell, "The dissociation energy of the nitrogen molecule," *Proc. R. Soc. London. Ser. A. Math. Phys. Sci.*, vol. 236, no. 1205, pp. 278–284, 1956, doi: 10.1098/rspa.1956.0135.

[45] J. S. Park, J. Sheng, J. H. Han, W. H. Choi, and J. Park, "Performance and Stability Enhancement of In-Sn-Zn-O TFTs Using SiO2 Gate Dielectrics Grown by Low Temperature Atomic Layer Deposition," *ACS Appl. Mater. Interfaces*, vol. 9, no. 49, pp. 42928–42934, 2017, doi: 10.1021/acsami.7b15419.

[46] H. Li and J. Robertson, "Behaviour of hydrogen in wide band gap oxides," *J. Appl. Phys.*, vol. 115, no. 20, 2014, doi: 10.1063/1.4878415.

Chapter 3 Study of humidity dependence on solution-processed UWB a-Ga_2O_x films.

3.1 Introduction

The rapid growth of mass-produced electronic devices has accelerated research into new deposition methods of thin-film components for large-scale production. Typically, vacuum deposition technique is limited because of its high cost, high energy requirement, experiment complexity, and difficulty in scaling to large-area electronics [1][2][3]. Thus, solution deposition technique provide an attractive alternative method due to large-area fabrication, equipment simplicity, atmospheric processing, and low cost [2][3][4]. It has been widely used as a deposition method of various oxide material such as amorphous InZnO [5][6], ZnO [7], InZnO [8][9], ScO_x [10], $LaAlO_3$ [11], $HfLaO_x$ [12], HfO_2 [13], etc.

In particular, since the research interest has shifted from wide bandgap materials ($E_g > 3.0$ eV) to ultra-wide bandgap materials ($E_g > 4.0$ eV), solution-processed ultra-wide bandgap (UWB) amorphous gallium oxide (a-Ga_2O_x) has been attracting great attention [1]. The huge interest on enhancing properties of solution-processed UWB a-Ga_2O_x is owing to large-scale production, high breakdown voltage, device design flexibility, excellent optical quality ($E_g >$ 4.8 eV), harsh-environment resistivity, and cost-effectiveness which has prospective applications for optoelectronic devices [14][15][16][17][18].

Nonetheless, precursor aging and atmospheric H_2O needs to be considered since it is an inevitable component in the solution deposition technique. The precursor aging was found to significantly affect thin-film formation as well as the device performance [19][20][21]. Moreover, the H_2O from nature (humidity) has potential to affect the metal oxide formation as well as the film formation. For instance, H_2O plays an integral role in sol-gel process particularly in the hydrolysis process [22]. It can dramatically decrease the decomposition temperature by changing the decomposition pathway [23][24], and further affect the metal-oxide formation as well as the film thickness [4]. Therefore, monitoring and controlling atmospheric H_2O during thin film deposition is critical.

In the previous chapter, a semiconducting solution-processed UWB a-Ga_2O_x has been successfully obtained *via* H_2 annealing. This chapter will specifically discuss an achievement of obtaining semiconducting behavior in as-deposited film which is apparently related to the deposition process. The effect of precursor aging and relative humidity (RH) on solution-deposited a-Ga_2O_x film characteristics will be further demonstrated. Section 3.2 presents the critical point of solution deposition technique such as precursor-related and environment-related impurity. The strategy to control these impurities will be discussed in detail.

Section 3.3 presents the precursor aging dependency on the a-Ga_2O_x films formation. While section 3.4 will discussed the achievement of obtaining semiconducting as-deposited solution-processed a-Ga_2O_x. Section 3.5 demonstrates the effect of dry and wet ambient on the a-Ga_2O_x TFTs. And eventually, the proposed mechanism will be discussed in section 3.6.

3.2 Critical point of solution deposition technique

Regardless of its ability to produce large-scale production, the solution deposition technique has severe impurities-related issues. It might originate from the precursor-related impurities and/or environment-related impurities as mentioned in the previous chapter. In this study, sol gel method was used to precursor synthesis by dissolving gallium nitrate hydrate in 2-methoxyethanol under constant stirring at room temperature for 12 hours. The nitrate-based precursor was selected to accelerate metal-oxide formation [25]. While the organic solvent was selected to prevent high reactivity reaction of metal-oxide and water [26]. In addition, the deposition routes based on 2-methoxyethanol is most appropriately considered as sol gel process because the key reaction precursor species are hydrolysis and condensation, in which metal-oxide bonds are formed [27] through the following equations:

Hydrolysis equation

$$M(OR)_x + H_2O \rightarrow M(OR)_{x-1}(OH) + ROH \quad \textbf{(3.1)}$$

Condensation equation (alcohol elimination)

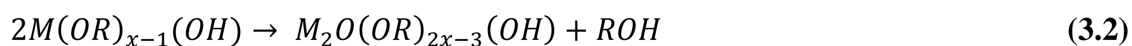

$$2M(OR)_{x-1}(OH) \rightarrow M_2O(OR)_{2x-3}(OH) + ROH \quad \textbf{(3.2)}$$

Condensation equation (water elimination)

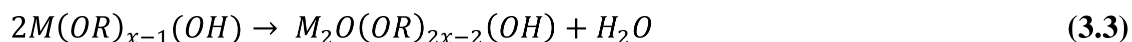

$$2M(OR)_{x-1}(OH) \rightarrow M_2O(OR)_{2x-2}(OH) + H_2O \quad \textbf{(3.3)}$$

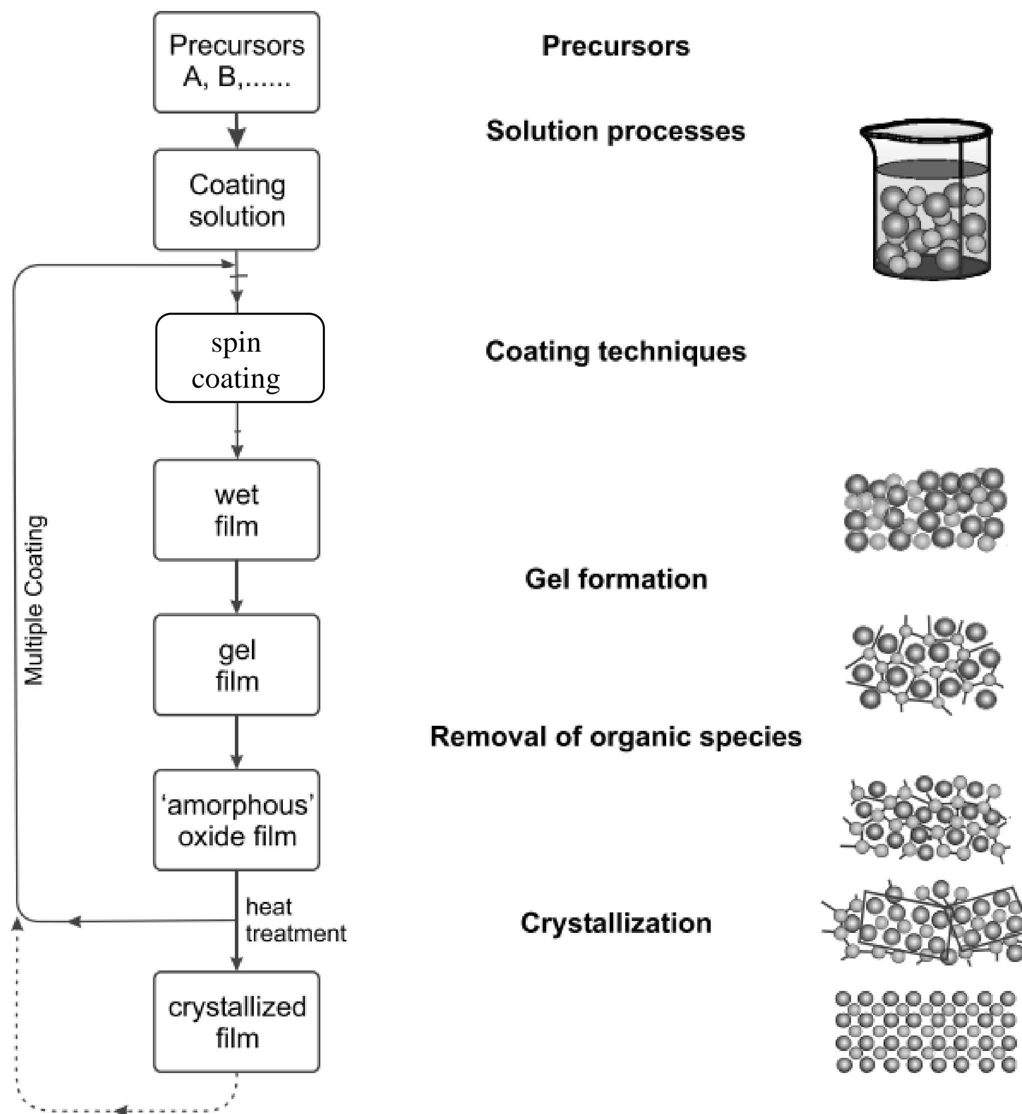

Figure 3.1. Flow chart of a typical solution deposition process [27].

Sol gel is an approach to synthesize materials through a phase transformation from liquid to sol and finally to gel. A typical sol gel reaction begins with dissolving metal salt in solvent. The metal cations undergo a hydrolysis reaction and subsequently the condensation reaction occurs to form metal oxide (M – O – M) bonds. Eventually, the oxide film is formed by coating the precursor solution and subjected to post-annealing to facilitate M – O – M bond formation (condensation), remove byproducts and solvent through evaporation/decomposition (impurity evaporation), and densify the resultant oxide film through void removal (film densification) [28]. Moreover, prolonging the annealing time or increasing the annealing temperature lead to

the film crystallization. Those film formation process through solution deposition technique was illustrated in ***Figure 3.1***.

Typically, precursor-related impurities are attributed to incomplete solvent evaporation which affects the film formation, metal-oxide bond formation as well as the TFT device performance [26]. Thus, the appropriate baking/annealing temperature is required. Thermograph analysis is generally used to define both pre-baking and post-baking temperature. As explained in chapter 2, the thermograph analysis of Gallium Oxide precursor reveals that the appropriate baking temperatures are at 150°C and 500°C for pre-baking and post-baking respectively. By applying both temperatures, Gallium Oxide films were successfully obtained. The XPS and SIMS spectra were also revealed that there were no nitrate-related peaks which suggest that the precursor-related impurities (nitrate compounds) were removed.

Other than that, the precursor-related impurities might be attributed to the precursor aging time. Olvera and colleagues in 2010 [20] demonstrated the effect of precursor aging time to the ZnO:F films. As the precursor was aged for 12 days, the F atoms are incorporated effectively into the ZnO lattice. When the F-incorporated increased, the electrical resistivity decreased which further increased the carrier concentration. Otherwise, 16-days-aged ZnO:F precursor in a dark room tends to increase the electrical resistivity owing to the instability of the chemical species formed during aging [21]. These competing results are mainly because of the different process parameters such as concentration, substrate temperature and F-dopant concentration. Selvan *et al.* reported that electrical resistivity increased as the CdZnS films aged from 1-4 days. Likewise, a red shift of optical bandgap was observed as the precursor was aged [29]. Apparently the precursor aging time was also increased the trap density [19].

In respect to the environment-related impurity, the solution deposition technique is highly environment-dependent, for instance relative humidity. The relative humidity is inversely proportional to the thickness [4]. Bakos *et al.* reported that the water content might affect the hydrolysis process because it might diffuse to the amorphous oxide films [22]. It can also change the decomposition pathway of ZnO precursor. An increase of the water vapor promotes Zn – O bonds formation [23][24].

Previous research revealed that precursor aging and relative humidity can significantly affect the film formation as well as the device performance. Nonetheless, there is no reported work focusing on the effect of precursor aging and relative humidity of solution-processed a-Ga_2O_x. Thus, this topic is much more interesting to be investigated.

3.3 Evaluation of precursor aging on the a-Ga_2O_x Films

As mentioned in the previous section, precursor aging time significantly affects the film formation as well as the electronic device performance. By varying the aging time, the film properties might be improved or deteriorate, mainly depending on the targeted materials. This chapter will specifically discuss the effect of precursor aging time to the solution-processed UWB a-Ga_2O_x material.

3.3.1.1 Device fabrication and characterization

Figure 3.2 illustrates the experimental procedure of a-Ga_2O_x films as well as the TFTs. Gallium oxide precursor (0.5 M) was synthesized *via* sol-gel method by dissolving gallium nitrate hydrate ($Ga(NO_3)_3{\cdot}xH_2O$ 99.999%, Sigma-Aldrich) in 2-methoxyethanol ($C_3H_8O_2$ anhydrous 99.8%, Sigma-Aldrich) under constant stirring at room temperature for 12 hours. The precursor solution was aged for 0, 3, and 7 weeks before the film deposition (***Figure 3.2***a).

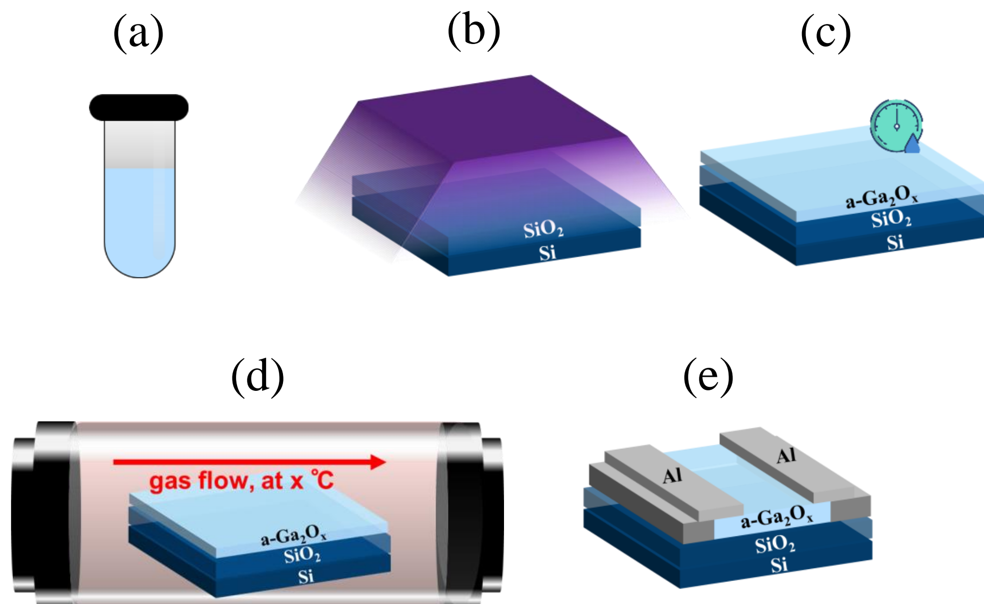

Figure 3.2. Schematic diagram of the fabrication of a-Ga_2O_x TFTs under controlled RH. Started by (a) precursor synthesis via sol-gel method, (b) substrate preparation and UV/O_3 treatment, (c) evaluate the humidity during film formation, (d) H2-annealing treatment, and (e) film patterning and metal deposition.

Heavily doped *p*-type Si substrates with thermally grown SiO_2 (85 nm) were used. To remove the organic residues on the substrates, conventional sulfuric-peroxide mixture (SPM) cleaning method was performed. Prior to the deposition, the substrate surface hydrophilicity was improved by subjecting UV/O_3 treatment for 10 mins at 115 °C (***Figure 3.2***b) using SAMCO UV and Ozone Dry Stripper Model UV-1 with a wavelength of 254 nm (85%) and 185 nm (15%). The a-Ga_2O_x channel was deposited *via* spin coating technique at 2000 rpm for 15 s followed by 2-step baking process at 150 °C and 500 °C, 5 mins each (***Figure 3.2***c). The final post-baking was done for 1 h. The relative humidity during baking (RH_{bake}) was fixed 20%.

For the annealed-films, the a-Ga_2O_x channel-islands were patterned by standard photolithography process and subsequent wet etching was performed using 0.05 M HCl solution. Afterwards, the a-Ga_2O_x film was annealed at 500 °C for 2 h under 4% hydrogen ambient (N_2:H_2 96:4%) which continuously flowed at a flowrate of 500 sccm (***Figure 3.2***d). Bottom-gate top-contact a-Ga_2O_x TFTs were fabricated by depositing 100-nm-thick Aluminum as source/drain electrodes *via* electron beam evaporation as illustrated in ***Figure 3.2***e.

3.3.1.2 Characterization

The optical properties such as optical bandgap (E_g), Urbach energy (E_u) and film transparency were estimated by ultraviolet-visible spectroscopy (UV-Vis; JASCO ILN-472). The E_g and E_u were calculated using Equation (2.1) and (2.3). Whereas the transfer characteristics of a-Ga_2O_x TFTs were analyzed using a semiconductor parameter analyzer (Agilent Technologies B1500A).

3.3.1.3 Film characteristics

To look deeper into the film characteristics, the optical properties such as E_g, film transparency, and E_u were evaluated and the results are summarized in ***Table 3-1***. As shown in ***Figure 3.3***, the blue shift of E_g was observed from 4.76 eV (non-aged precursor) to 4.98 eV (7 weeks-aged precursor). A wider E_g will lead to difficulty in obtaining semiconducting behavior

since it hinders electron mobility. Thus, using the starting non-aged precursor is preferred since it has relatively lower E_g. Regardless of the E_g values, all films are categorized as ultra-wide bandgap materials ($E_g > 4.0$ eV) which typically exhibit superior optical properties as compared to the wide bandgap material ($E_g > 3.0$ eV).

Moreover, a unique film transparency was observed at different range of light region. At visible light region (transmittance at wavelength of 555 nm, T_{555nm}), all samples show similar film transparency of ~95%. While at UV light region, (transmittance at wavelength of 450 nm, T_{450nm}), the film transparency increased up to 98% as the starting precursor was aged for 7 weeks. Typically, the reduction in the film transparency might be attributed to the free carrier absorption which is related to the improvement of the film carrier density [30]. On the other hand, an increase in the film transparency might be caused by the reduction of the film carrier density.

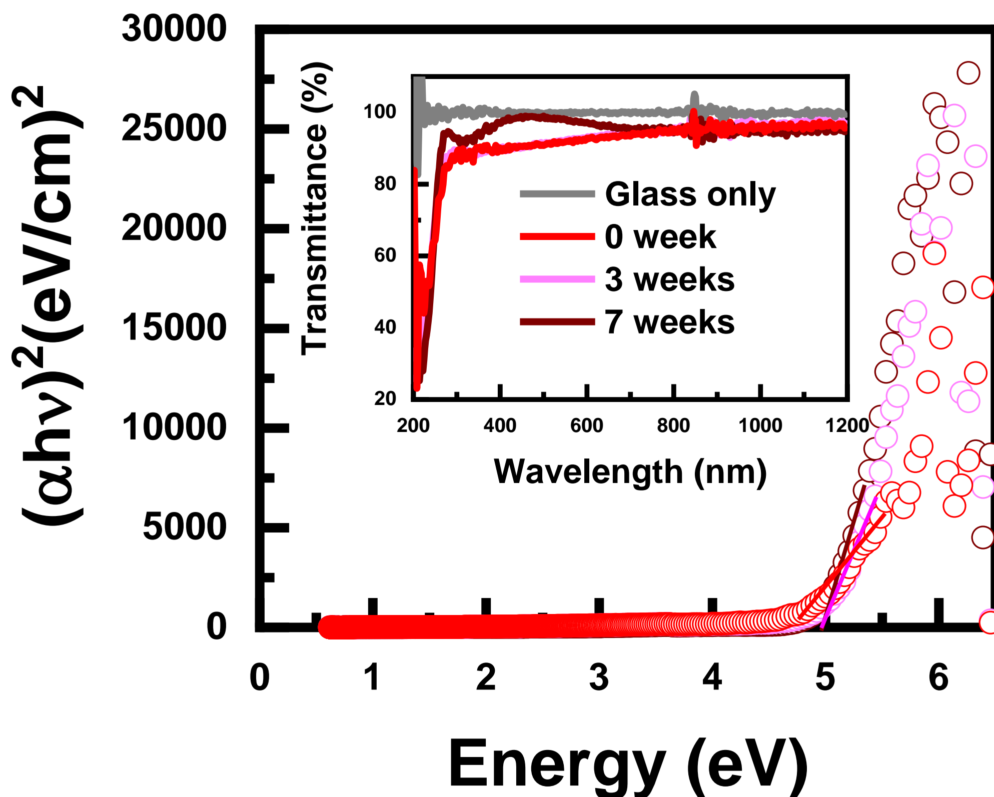

Figure 3.3. Optical bandgap and transmittance (inset) of non-aged and aged a-Ga_2O_x films.

Table 3-1. Summary of non-aged and aged a-Ga2Ox film characteristics.

Sample	E_g (eV)	Transparency (T_{555nm} in %)	Transparency (T_{450nm} in %)	E_u (meV)
0 week	4.76	95	90	688.4
3 weeks	4.89	95	90	530.1
7 weeks	4.98	95	98	371.2

Furthermore, the E_u which indicates the subgap disorder level of oxide material was also evaluated. As showed in ***Table 3-1***, the E_u was decreased from 688.4 meV to 371.2 meV proportional to the aging time. As the precursor was aged and atoms are tightly incorporated [20][31], the subgap disorder was reduced. To clarify this hypothesis, further film characterizations to elucidate the atomic bonds and chemical reactions is required. Since this is a preliminary work on solution-deposited a-Ga_2O_x films, future work on this topic is recommended.

3.3.1.4 TFT characteristics

By using the non-aged and aged precursors, the as-deposited a-Ga_2O_x TFTs were fabricated. ***Figure 3.4*** (left side) showed the transfer characteristics of as-deposited a-Ga_2O_x TFTs. It is observed that the TFT performance were degraded as the starting precursor was aged from 0 to 7 weeks. The as-deposited TFT, which prepared by using fresh precursor, showed excellent switching behavior with saturation mobility of ~10^2 cm^2/Vs, V_{th} = 32.9 V, SS = 0.31 V/dec, and ON/OFF current ratio of ~10^4 as summarized in ***Table 3-2***. When the additional H_2-annealing was applied, the V_{th} was shifted negatively which implies more electron carrier concentrations present in the H_2-annealed film (***Figure 3.4*** right side). The H-dopant was incorporated along with the H_2-annealing which further promotes electron carrier concentrations. However, excess H-dopant tends to degrade the device performance which showed as the reduce in the ON/OFF ratio up to 2 order magnitude. Likewise, the saturation mobility was also decreased.

Otherwise, the 3 weeks-aged precursor produced non-switching behavior of the as-deposited a-Ga_2O_x TFT. Interestingly, the H_2-annealed TFT exhibited switching behavior which mainly caused by the H-dopant incorporation as mentioned above. While for the 7 weeks-aged precursor, there were no switching behavior observed for both as-deposited and

H_2-annealed TFTs. Apparently, precursor aging tends to introduce defects and/or impurities which further deteriorate the film formation as well as the TFT device performances.

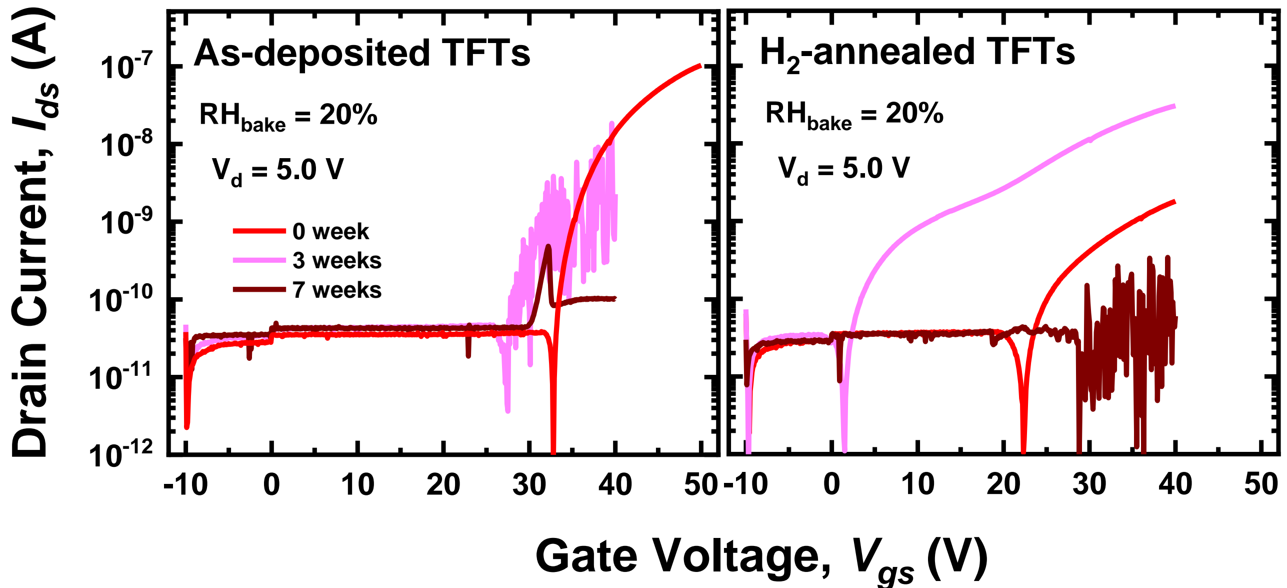

Figure 3.4. Transfer characteristics of non-aged and aged precursor for as-deposited (left) and H_2-annealed (right) a-Ga_2O_x TFTs.

Table 3-2. Summary of Gallium Oxide TFT performance for non-aged and aged precursor.

Sample	Aging	μ_{sat} (cm^2/Vs)	V_{th} (V)	SS (V/dec)	ON/OFF ratio
As-deposited	0 week	$(1.4 \pm 0.2) \times 10^{-2}$	32.9 ± 0.3	0.31 ± 0.08	$\sim 10^4$
As-deposited	3 weeks	No switching			
As-deposited	7 weeks	No switching			
H_2-annealed	0 week	$(7.7 \pm 0.2) \times 10^{-3}$	22.4 ± 1.0	0.34 ± 0.11	$\sim 10^2$
H_2-annealed	3 weeks	$(1.1 \pm 0.02) \times 10^{-2}$	1.7 ± 0.9	0.15 ± 0.19	$\sim 10^4$
H_2-annealed	7 weeks	No switching			

In selected cases, the H_2-annealing helps to enhance the electron carrier concentration as well as the device performance. Nonetheless, over-aged precursor has numerous defects and/or impurities which makes it difficult to obtain the electron mobility. In addition, H_2-annealing will deteriorate the device performance since it introduced more defects (H-dopant or H-interstitial defect). In respect to the source of defects and/or impurities of aged precursor, the

dedicated chapter to elucidate this topic is required. Therefore, I would suggest this topic for the future work. Regardless of the source of defects and/or impurities of aged precursor, the fresh starting precursor showed excellent TFT performance. Thus, this precursor will be used for the next studies in the next section.

3.4 Achievement of semiconducting behavior of as-deposited a-Ga_2O_x TFTs in controlled RH

Chapter 2 has demonstrated semiconducting behavior of solution-processed UWB a-Ga_2O_x *via* H_2-annealing. Whereas in the previous section, by using a fresh precursor solution and fixing the RH_{bake}, the semiconducting behavior of as-deposited a-Ga_2O_x TFT was successfully obtained. The achievement of obtaining semiconducting behavior of as-deposited a-Ga_2O_x TFTs will be further discussed in this section. In particular, the as-deposited TFTs will be prepared under different fabrication process: uncontrolled and controlled relative humidity (RH). The TFT characteristics will be evaluated. Moreover, the fresh precursor solution will be used starting from this section.

3.4.1.1 Device fabrication

Figure 3.5 illustrates the experimental procedure of as-deposited a-Ga_2O_x TFTs under uncontrolled and controlled RH_{bake}. Particularly, this section will discuss the as-deposited a-Ga_2O_x TFT under different fabrication process. Thus, there was no additional annealing applied. The fresh precursor (0.5 M Gallium Oxide precursor) was prepared by dissolving gallium nitrate hydrate ($Ga(NO_3)_3{\cdot}xH_2O$ 99.999%, Sigma-Aldrich) in 2-methoxyethanol ($C_3H_8O_2$ anhydrous 99.8%, Sigma-Aldrich) *via* sol gel method. The gallium oxide precursor was subsequently deposited after sol-gel process was finished (***Figure 3.5***a). Heavily doped *p*-type Si substrates with thermally grown SiO_2 (85 nm) were used. To remove the organic residues on the substrates, conventional sulfuric-peroxide mixture (SPM) cleaning method was performed. Prior to the deposition, the substrate surface hydrophilicity was improved by subjecting UV/O_3 treatment for 10 mins at 115 °C (***Figure 3.5***b) using SAMCO UV and Ozone Dry Stripper Model UV-1 with a wavelength of 254 nm (85%) and 185 nm (15%). The a-Ga_2O_x channel was deposited *via* spin coating technique at 2000 rpm for 15 s followed by 2-

step baking process at 150 °C and 500 °C, 5 mins each (***Figure 3.5***c). The final post-baking was done for 1 h.

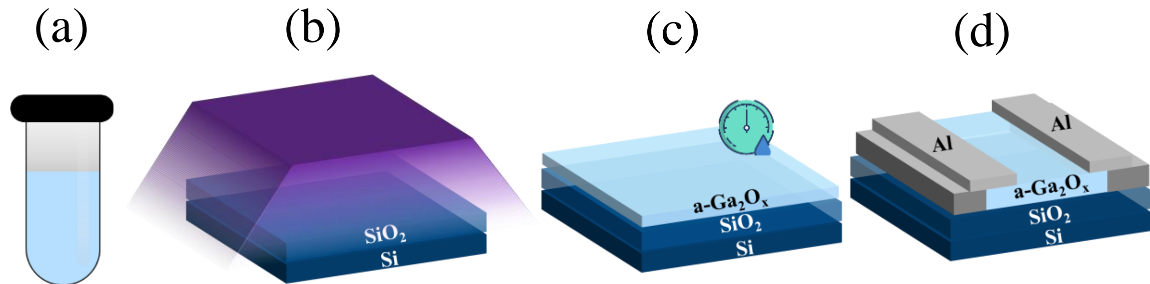

Figure 3.5. Schematic diagram of the fabrication process of as-deposited a-Ga2Ox TFTs under uncontrolled and controller RH.

The as-deposited TFTs were prepared at two different fabrication conditions: uncontrolled RH and controlled RH. The uncontrolled RH was fabricated by depositing the film at atmospheric condition without any environment modification. The controlled RH condition was obtained by controlling the RH during the spin coating deposition (RH_{depo} fixed at 70%), and during the baking (RH_{bake} was fixed at 30%). Afterwards, a-Ga_2O_x channel-islands were patterned by standard photolithography process and subsequently the wet etching was achieved using 0.05 M HCl solution. Bottom-gate top-contact a-Ga_2O_x TFTs were fabricated by depositing 100-nm-thick Aluminum as source/drain electrodes *via* electron beam evaporation (***Figure 3.5***d).

3.4.1.2 TFT characteristics

Figure 3.6 showed the as-deposited a-Ga_2O_x TFTs under uncontrolled and controlled RH. The transfer characteristics of uncontrolled a-Ga_2O_x TFT is completely inactive. This is might be due to the nature of UWB a-Ga_2O_x which has complex combination of amorphous phase structure, ultra-wide bandgap material, and low electron carrier concentration which hinder electron mobility.

Interestingly, as the film was deposited under controlled RH condition of RH_{depo} = 70% and RH_{bake} = 30%, it exhibited switching behavior as displayed in ***Figure 3.6***. This excellent

result marks the success of UWB material engineering, where the semiconducting behavior was successfully obtained for solution-processed as-deposited UWB a-Ga_2O_x material. Apparently, the controlled RH significantly modified the TFT device performance. To look deeper on the reason of this achievement, additional experiment was performed to further vary the RH under dry and wet condition which will be discussed in the next section.

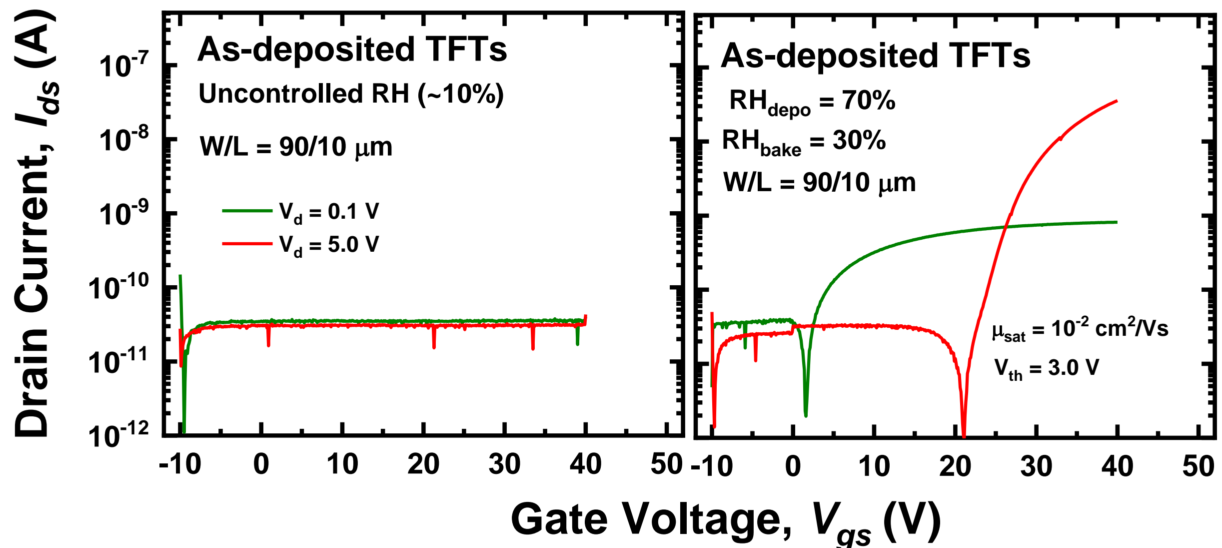

Figure 3.6. Transfer characteristics of as-deposited a-Ga_2O_x TFTs under uncontrolled (left) and controlled (right) RH.

3.5 Evaluation of dry and wet humidity on the a-Ga_2O_x TFTs

Previously, semiconducting behavior of vacuum-processed a-Ga_2O_x was demonstrated by Kim *et al.* in 2017 [1]. In this section, the first demonstration of obtaining semiconducting behavior of solution-processed as-deposited a-Ga_2O_x will be discussed.

3.5.1.1 Device fabrication and characterization

The fabrication process was similar to ***Figure 3.2*** in section 3.3.1. The 0.5 M of Gallium oxide precursor was prepared *via* sol-gel method by dissolving gallium nitrate hydrate ($Ga(NO_3)_3 \cdot xH_2O$ 99.999%, Sigma-Aldrich) in 2-methoxyethanol ($C_3H_8O_2$ anhydrous 99.8%, Sigma-Aldrich) under constant stirring at room temperature for 12 hours. The gallium oxide precursor was subsequently deposited after sol-gel process was finished. The a-Ga_2O_x channel

was deposited *via* spin coating technique at 2000 rpm for 15 s followed by 2-step baking process at 150 °C and 500 °C, 5 mins each. The final post-baking was done for 1 h. The relative humidity during film deposition (RH_{depo}) was fixed at 70%. Whereas the relative humidity during baking (RH_{bake}) were varied at 20% (dry) and 60% (wet). The film characteristics as well as the TFT performances were evaluated.

For the annealed-films, the a-Ga_2O_x channel-islands were patterned by standard photolithography process and subsequently the wet etching was achieved using 0.05 M HCl solution. Afterwards, the a-Ga_2O_x film was annealed at 500 °C for 2 h under 4% hydrogen ambient (N_2:H_2 96:4%) which continuously flowed at a flowrate of 500 sccm. Bottom-gate top-contact a-Ga_2O_x TFTs were fabricated by depositing 100-nm-thick Aluminum as source/drain electrodes *via* electron beam evaporation.

The film thickness, phase structure, and film density were characterized and determined by profilometer, grazing incidence X-ray diffraction (XRD; Rigaku SmartLab9kW/IP/HY/N), and X-ray reflectivity spectroscopy (XRR; Rigaku SmartLab9kW/IP/HY/N), respectively. Optical properties such as bandgap values (E_g), Urbach energy (E_u) and film transparency were estimated by ultraviolet-visible spectroscopy (UV-Vis; JASCO ILN-472). Lastly, elemental analysis and hydrogen diffusion were evaluated by secondary ion mass spectroscopy (SIMS; ULVAC-PHI ADEPT-1010). The transfer characteristics of a-Ga_2O_x TFTs were analyzed using a semiconductor parameter analyzer (Agilent Technologies B1500A).

3.5.1.2 Film characteristics

Figure 3.7 displays the XRD pattern of a-Ga_2O_x films under dry and wet RH to evaluate the phase structure of the films. It was observed that both dry and wet RH did not change the amorphous structure of a-Ga_2O_x films. Typically, the dry and wet RH mainly affect the water content in the bulk film. Whereas the film crystallization might occur because of high temperature annealing close to the crystalline temperature (T_C = 680 °C) or the thermally driven band rearrangement as mention in the chapter 2. In addition, the H_2-annealing also did not change the amorphous structure which was also consistent with the previous work in chapter 2.

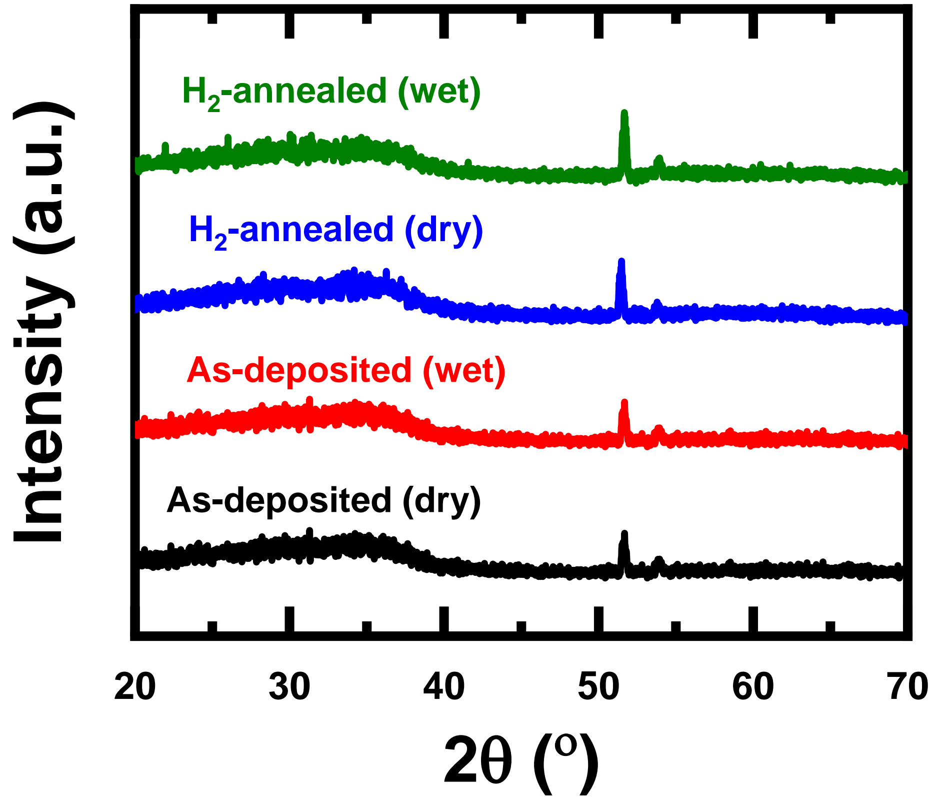

Figure 3.7. XRD spectra of a-Ga_2O_x films under dry and wet RH.

Although there was no significant phase structure dependency on the RH, a significant thickness dependency was observed. Wet RH has numerous water vapor which might be trapped to the wet Gallium Oxide film. In respect to the sol gel method, the film formation was started by coating the precursor onto a substrate, followed by phase transformation from liquid to sol, and finally to gel [28]. During that process, the wet film was highly sensitive to the environment condition. When the environment has numerous water vapor, it tends to be trapped into the wet film and loosely bounded to the atoms. As baking temperature was applied, those water vapor which is loosely bounded will evaporate. Apparently, a rapid-massive water evaporation occurred during the post-baking (500 °C) which further leave behind the remaining vacancies (oxygen vacancies). During the metal oxide formation, the atoms are tightly bounded and densified which implies the thickness reduction from 20.6 nm to 15.7 nm. Moreover, the presence of vacancies implies the loosening of atomic arrangement which further decreased the film density from 4.43 g/cm^3 to 4.14 g/cm^3 ***Table 3-3***.

Table 3-3. Summary of a-Ga_2O_x films characteristics under dry and wet RH.

Sample	Thickness (nm)	Roughness (nm)	Film density (g/cm^3)	Transparency (T_{450nm} in %)	E_u (meV)	E_g (eV)
As-depo (dry)	20.6	0.44	4.43	99	508.7	4.86
As-depo (wet)	15.7	0.52	4.14	98	506.7	4.86
H_2-anneal (dry)	21.0	0.44	4.03	96	828.6	4.65
H_2-anneal (wet)	15.9	0.50	3.79	92	707.4	4.79

Similar trend was also observed for the H_2-annealed films under dry and wet RH. Interestingly, the film density was reduced for the H_2-annealed films. In this case, the H_2 gas which flowed during H_2-annealing acts as a shallow donor. The H-dopant was diffused and was incorporated to the a-Ga_2O_x films (particularly in the oxygen side).

Furthermore, the optical properties such as film transparency, E_g and E_u were also evaluated. The as-deposited film has excellent optical quality with E_g of 4.86 eV and film transparency of ~99% as summarized in ***Table 3-3***. Similar transparency as well as the E_g were observed for the films deposited at dry and wet RH. It is likely that the water vapor (RH) did not affect the optical properties of as-deposited a-Ga_2O_x films. Once the film was annealed at 500 °C in 4% H_2 gas, the reduction of the film transparency as well as the E_g were observed. This might be caused by the H-dopant incorporation which acts as a shallow donor [14]. The H-dopant was incorporated to the a-Ga_2O_x bulk film and further increased the electron carrier concentration. This improvement was reflected to the film transparency reduction as the free carriers actively absorb the light energy [30]. Furthermore, the H-dopant also occupied the donor level near the conduction band which further narrowed the E_g from 4.86 meV to 4.65 meV.

Hereafter, the Urbach energy (E_u) was also calculated to evaluated the subgap disorder level of oxide materials. As showed in ***Table 3-3***, the E_u value was increased from 506.7 meV to 828.6 meV. In general, the amorphous nature has a random structure which contributes to subgap disorder of oxide films. After H_2-annealing, the E_u was increased up to 828.6 meV which is mainly caused by the complex combination of amorphous disorder and defect impurity. In terms of amorphous disorder, the H_2-annealed film has higher structural randomness level than the as-deposited films. The annealing encourages the atomic bond rearrangement but is insufficient to crystallize the films which contributed to the subgap disorder of H_2-annealed

films. In addition, the H_2 gas was diffused and was incorporated to the highly random H_2-annealed a-Ga_2O_x films. Thus, a relatively high E_u were observed for the H_2-annealed films.

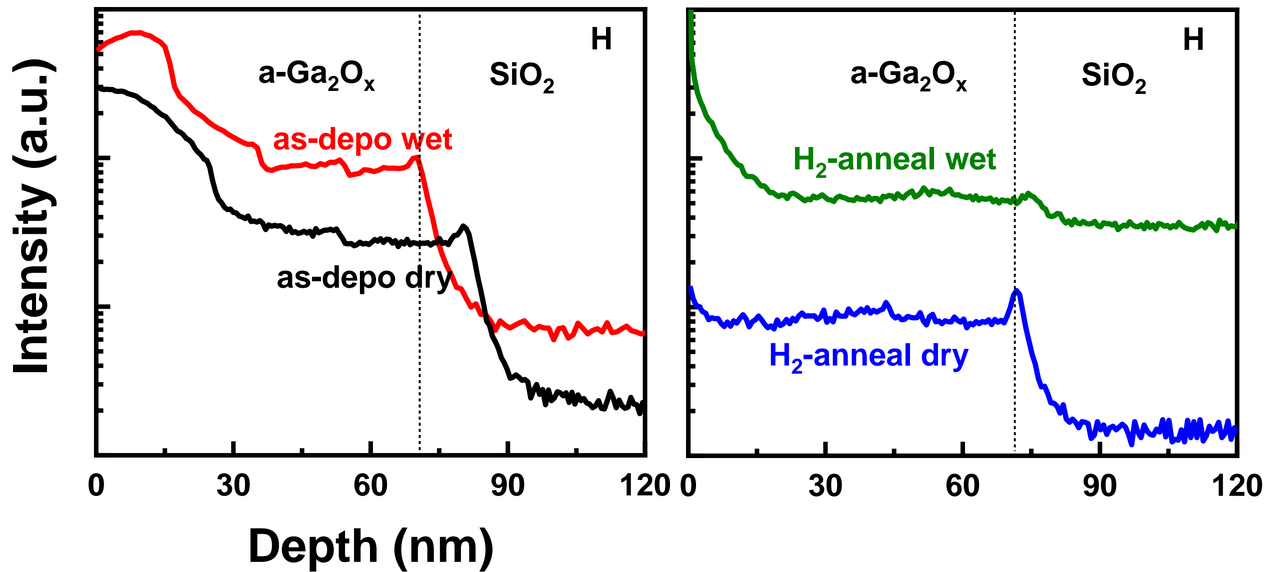

Figure 3.8. SIMS of a-Ga_2O_x films deposited at dry and wet RH.

To look deeper on the H-diffusion, SIMS measurement was conducted. In general, the wet RH has relatively higher H content as displayed in ***Figure 3.8***. A unique hump was observed specifically for the as-deposited films at ~ 30 nm depth from the surface. These humps were removed after H_2-annealing. Apparently, for the as-deposited films, the heat induced by the hot plate was restrained since a-Ga2Ox was known as thermally stable material [16]. Moreover, when the post-baking time was prolonged from 1 to 2 h, those humps were removed. Similarly, the humps were also removed for the H_2-annealed films.

3.5.1.3 TFT characteristics

The transfer characteristics of a-Ga_2O_x TFTs are displayed in ***Figure 3.9***. In particular, the as-deposited TFT deposited at RH_{bake} of 20% exhibited switching behavior with saturation mobility of ~10^{-2} cm^2/Vs, V_{th} = 34.8 V, SS = 0.31 V/dec, and ON/OFF current ratio of 10^4 as summarized in ***Table 3-4***. As the RH_{bake} was increased to 30%, the negative shift of the V_{th} was observed. This is caused by the water vapor which can also act as H-dopant and further increased the electron carrier concentration which was observed as the negative shift of V_{th}.

Nonetheless, as the RH_{bake} was increased up to 60%, device deterioration was observed. Numerous H-dopant was introduced and create interstitial defect which further reflected as switch-off TFT behavior.

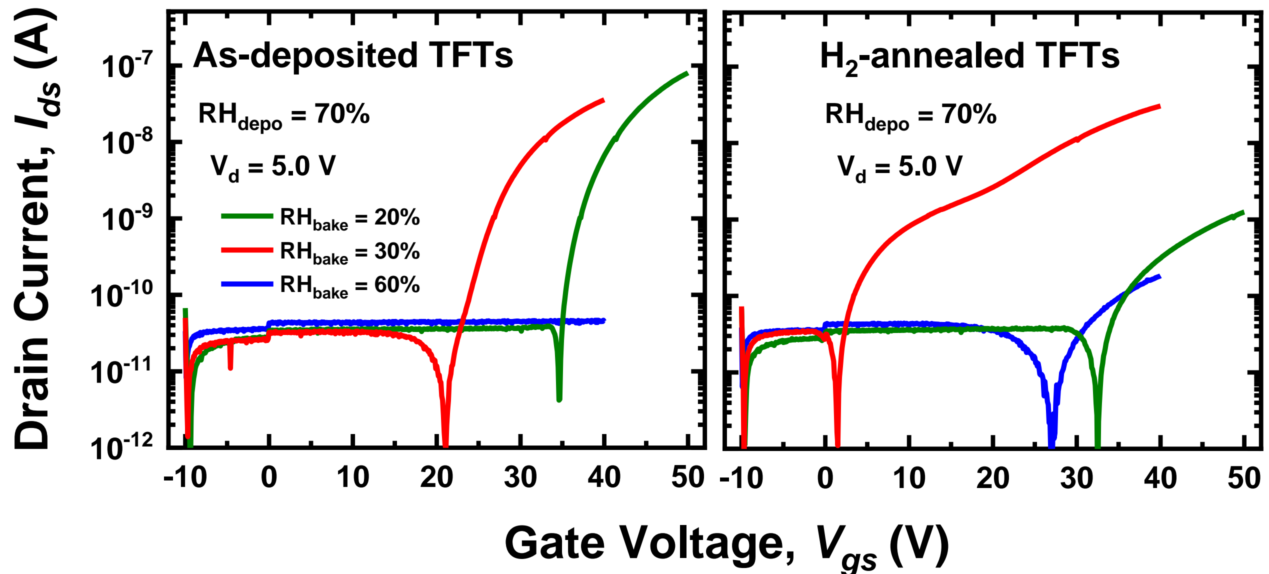

Figure 3.9. Transfer characteristics of a-Ga_2O_x TFTs at dry and wet RH.

Table 3-4. Summary of a-Ga_2O_x TFT performance at dry and wet RH.

Sample	RH_{bake}	μ_{sat} (cm^2/Vs)	V_{th} (V)	SS (V/dec)	ON/OFF ratio
As-deposited	20%	$(0.9 \pm 0.2) \times 10^{-2}$	34.8 ± 0.3	0.31 ± 0.02	$\sim 10^4$
As-deposited	30%	$(1.0 \pm 0.2) \times 10^{-2}$	21.4 ± 0.9	0.39 ± 0.30	$\sim 10^4$
As-deposited	60%		No switching		
H_2-annealed	20%	$(7.1 \pm 0.2) \times 10^{-3}$	32.6 ± 0.2	0.42 ± 0.11	$\sim 10^2$
H_2-annealed	30%	$(1.1 \pm 0.02) \times 10^{-2}$	1.5 ± 0.9	0.15 ± 0.19	$\sim 10^4$
H_2-annealed	60%		No switching		

Similar trend was also observed for the H_2-annealed TFTs. As the RH_{bake} was increased from 20% to 30%, the Vth was shifted negatively. As the RH_{bake} was increased at higher humidity of 60%, the device was deteriorated. Likely, the water vapor (H_2O) and H_2-gas annealing (H_2 atom) have similar role in improving the device performance by acting as a shallow donor. In general, for *n*-type semiconductor, the dopant will exist as a cation (H^+). Thus, the H-dopant tend to bind with oxygen atom. In respect to the H-dopant sources, it might be

originated from the hydroxyl group (OH^-) from water (H_2O), or it might be originated from H_2 gas which bind to oxygen atom.

3.6 Proposed mechanism on the electrical characteristic improvement of a-Ga_2O_x TFTs

Figure 3.10 illustrates the schematic of proposed mechanism. Prior to the proposed mechanism, the film formation process in from wet film into amorphous film needs to be understood (***Figure 3.10*** (a)). During that process, the wet film was highly sensitive to the environment condition. Therefore, the water vapor tends to trapped. When the film was deposited at dry RH, the film has relatively low H-trapped (***Figure 3.10*** (b)).

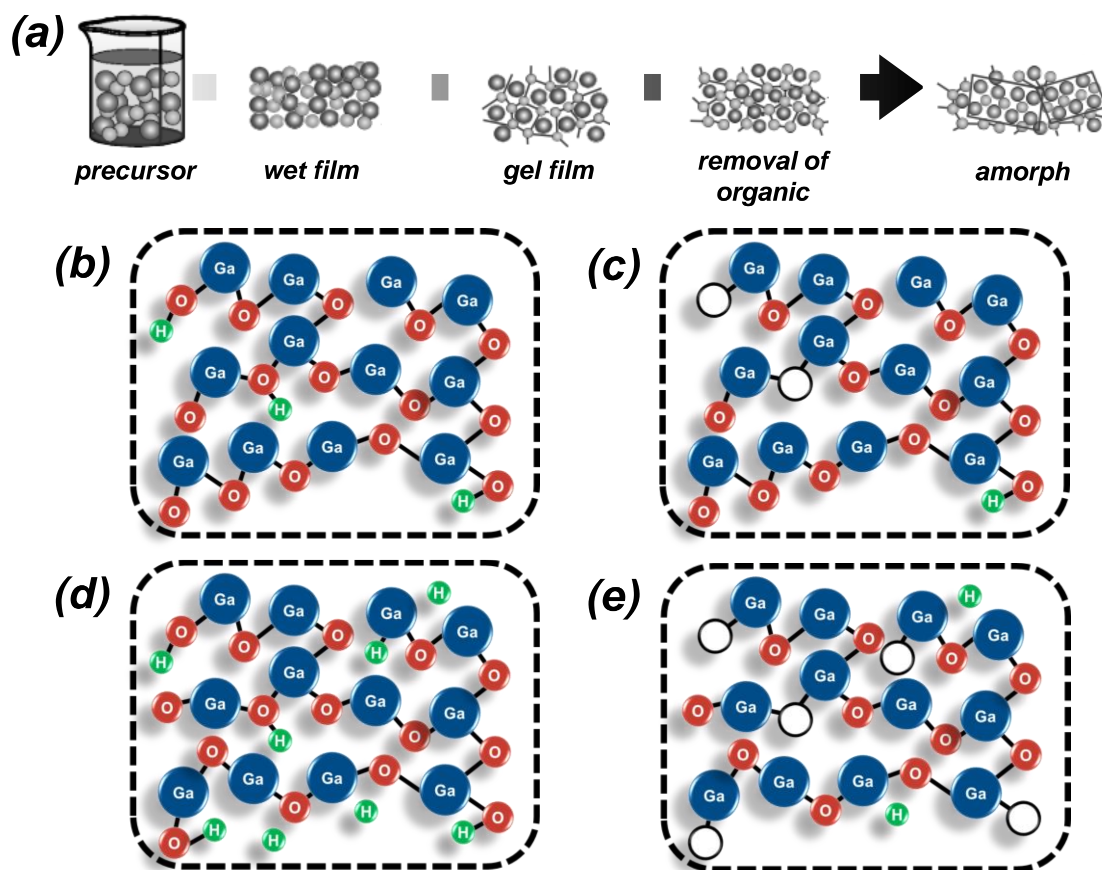

Figure 3.10. Schematic diagram of proposed mechanism. (a) Film formation from wet film into amorphous film. Film transformation from wet film (b) into amorphous film (c) in dry ambient. And film transformation from wet film (d) into amorphous film (e) in wet ambient.

As baking temperature was applied, those water vapor which is loosely bounded was evaporated as well as the organic compound. Thus, a rapid-massive water evaporation occurred

during the post-baking (500 °C) which further left the remaining vacancies (oxygen vacancies). During the film densification, the atoms are tightly bounded and densified which implies the reduction of thickness as well as the film density (***Figure 3.10*** (c)).

Otherwise, in wet ambient, it suggests that there was excess amount of H-trapped which further leaves numerous vacancies after baking (***Figure 3.10*** (d)). As compared to dry-sample, the wet-sample has more vacancies which tends to form thinner film with lower film density owing to numerous vacancies which present before the densification (***Figure 3.10*** (e)). Thus, dry ambient tends to form thicker film with higher film density. While wet ambient tends to form thinner film with lower film density.

3.7 Summary

In summary, the first demonstration of semiconducting behavior of as-deposited solution-processed ultra-wide bandgap a-Ga_2O_x (E_g > 4.8 eV) has been successfully achieved. We have briefly studied the effect of precursor aging to the solution-processed a-Ga_2O_x TFT performance. It was found that the optimum aging time for as-deposited film is 0 week. Moreover, we found that by controlling the relative humidity during film deposition, the semiconducting behavior of as deposited solution-process ultra-wide bandgap a-Ga_2O_x was obtained. It was found that the water vapor (H_2O) at wet humidity and the H_2 gas during annealing attributed to the H-dopant. The incorporation of H-dopant into a-Ga_2O_x film leads to an increase in electron carrier concentration as reflected by TFT switching behavior. Nonetheless, wet ambient tends to deteriorate the TFT performance owing to excess H-incorporated which acts as interstitial defect. Therefore, the optimum humidity condition was determined at 70% humidity during precursor deposition (RH_{depo}), and 30% humidity during film formation (RH_{bake}).

3.8 References

[1] J. Kim, T. Sekiya, N. Miyokawa, N. Watanabe, K. Kimoto, K. Ide, Y. Toda, S. Ueda, N. Ohashi, H. Hiramatsu, H. Hosono, and T. Kamiya, "Conversion of an ultra-wide bandgap amorphous oxide insulator to a semiconductor," *NPG Asia Mater.*, vol. 9, no. 3, 2017, doi: 10.1038/am.2017.20.

[2] D. C. Corsino, J. P. S. Bermundo, C. Kulchaisit, M. N. Fujii, Y. Ishikawa, H. Ikenoue, and Y. Uraoka, "High-Performance Fully Solution-Processed Oxide Thin-Film Transistors via Photo-Assisted Role Tuning of InZnO," *ACS Appl. Electron. Mater.*, vol. 2, no. 8, pp. 2398–2407, 2020, doi: 10.1021/acsaelm.0c00348.

[3] W. Xu, H. Li, J. Bin Xu, and L. Wang, "Recent Advances of Solution-Processed Metal Oxide Thin-Film Transistors," *ACS Appl. Mater. Interfaces*, vol. 10, no. 31, pp. 25878–25901, 2018, doi: 10.1021/acsami.7b16010.

[4] P. N. Plassmeyer, G. Mitchson, K. N. Woods, D. C. Johnson, and C. J. Page, "Impact of Relative Humidity during Spin-Deposition of Metal Oxide Thin Films from Aqueous Solution Precursors," *Chem. Mater.*, vol. 29, no. 7, pp. 2921–2926, 2017, doi: 10.1021/acs.chemmater.6b05200.

[5] K. K. Banger, Y. Yamashita, K. Mori, R. L. Peterson, T. Leedham, J. Rickard, and H. Sirringhaus, "Low-temperature, high-performance solution-processed metal oxide thin-film transistors formed by a 'sol-gel on chip' process," *Nat. Mater.*, vol. 10, no. 1, pp. 45–50, 2011, doi: 10.1038/nmat2914.

[6] G. Liu, A. Liu, H. Zhu, B. Shin, E. Fortunato, R. Martins, Y. Wang, and F. Shan, "Lowerature, nontoxic water-induced metal-oxide thin films and their application in thin-film transistors," *Adv. Funct. Mater.*, vol. 25, no. 17, pp. 2564–2572, 2015, doi: 10.1002/adfm.201500056.

[7] J. Chang, K. L. Chang, C. Chi, J. Zhang, and J. Wu, "Water induced zinc oxide thin film formation and its transistor performance," *J. Mater. Chem. C*, vol. 2, no. 27, pp. 5397–5403, 2014, doi: 10.1039/c3tc32311k.

[8] J. W. Na, Y. G. Kim, T. S. Jung, Y. J. Tak, S. P. Park, J. W. Park, S. J. Kim, and H. J. Kim, "Interface location-controlled indium gallium zinc oxide thin-film transistors using a solution process," *J. Phys. D. Appl. Phys.*, vol. 49, no. 8, 2016, doi: 10.1088/0022-3727/49/8/085301.

[9] S. Kumaran, M. T. Liu, K. Y. Lee, and Y. Tai, "The Impact of Solvents on the Performances of Solution-Processed Indium Gallium Zinc Oxide Thin-Film Transistors Using Nitrate Ligands," *Adv. Eng. Mater.*, vol. 22, no. 2, pp. 1–9, 2020, doi: 10.1002/adem.201901053.

[10] A. Liu, G. Liu, H. Zhu, H. Song, B. Shin, E. Fortunato, R. Martins, and F. Shan, "Water-Induced Scandium Oxide Dielectric for Low-Operating Voltage n- and p-Type Metal-Oxide Thin-Film Transistors," *Adv. Funct. Mater.*, vol. 25, no. 46, pp. 7180–7188, 2015, doi: 10.1002/adfm.201502612.

[11] P. N. Plassmeyer, K. Archila, J. F. Wager, and C. J. Page, "Lanthanum aluminum oxide thin-film dielectrics from aqueous solution," *ACS Appl. Mater. Interfaces*, vol. 7, no. 3, pp. 1678–1684, 2015, doi: 10.1021/am507271e.

[12] J. Ko, J. Kim, S. Y. Park, E. Lee, K. Kim, K. H. Lim, and Y. S. Kim, "Solution-processed amorphous hafnium-lanthanum oxide gate insulator for oxide thin-film transistors," *J. Mater. Chem. C*, vol. 2, no. 6, pp. 1050–1056, 2014, doi: 10.1039/c3tc31727g.

[13] K. Jiang, J. T. Anderson, K. Hoshino, D. Li, J. F. Wager, and D. A. Keszler, "Low-energy path to dense HfO2 thin films with aqueous precursor," *Chem. Mater.*, vol. 23, no. 4, pp. 945–952, 2011, doi: 10.1021/cm102082j.

[14] D. Purnawati, J. P. Bermundo, and Y. Uraoka, "Insulator-to-semiconductor conversion of solution-processed ultra-wide bandgap amorphous gallium oxide via hydrogen annealing," *Appl. Phys. Express*, vol. 15, no. 2, p. 24003, 2022, doi: 10.35848/1882-0786/ac466a.

[15] S. Mitra, Y. Pak, B. Xin, D. R. Almalawi, N. Wehbe, and I. S. Roqan, "Solar-Blind Self-Powered Photodetector Using Solution-Processed Amorphous Core-Shell Gallium Oxide Nanoparticles," *ACS Appl. Mater. Interfaces*, vol. 11, no. 42, pp. 38921–38928, Oct. 2019, doi: 10.1021/acsami.9b11694.

[16] S. J. Pearton, J. Yang, P. H. Cary IV, F. Ren, J. Kim, M. J. Tadjer, and M. A. Mastro, "A review of Ga2O3 materials, processing, and devices," *Appl. Phys. Rev.*, vol. 5, p. 011301, 2018.

[17] H. Liang, Z. Han, and Z. Mei, "Recent Progress of Deep Ultraviolet Photodetectors using Amorphous Gallium Oxide Thin Films," *Phys. Status Solidi Appl. Mater. Sci.*, vol. 218, no. 1, p. 2000339, Jan. 2021, doi: 10.1002/pssa.202000339.

[18] X. Hou, X. Zhao, Y. Zhang, Z. Zhang, Y. Liu, Y. Qin, P. Tan, C. Chen, S. Yu, M. Ding, G. Xu, Q. Hu, and S. Long, "High-Performance Harsh-Environment-Resistant GaOX Solar-Blind Photodetectors via Defect and Doping Engineering," *Adv. Mater.*, vol. 34, no. 1, pp. 1–11, 2022, doi: 10.1002/adma.202106923.

[19] H. Tsai, W. Nie, Y. H. Lin, J. C. Blancon, S. Tretiak, J. Even, G. Gupta, P. M. Ajayan, and A. D. Mohite, "Effect of Precursor Solution Aging on the Crystallinity and Photovoltaic Performance of Perovskite Solar Cells," *Adv. Energy Mater.*, vol. 7, no. 11, pp. 1–9, 2017, doi: 10.1002/aenm.201602159.

[20] R. R. Biswal, S. Velumani, B. J. Babu, A. Maldonado, S. Tirado-Guerra, L. Castañeda, and M. De La, "Fluorine doped zinc oxide thin films deposited by chemical spray, starting from zinc pentanedionate and hydrofluoric acid: Effect of the aging time of the solution," *Mater. Sci. Eng. B Solid-State Mater. Adv. Technol.*, vol. 174, no. 1–3, pp. 46–49, 2010, doi: 10.1016/j.mseb.2010.03.013.

[21] R. Anandhi, R. Mohan, K. Swaminathan, and K. Ravichandran, "Influence of aging time of the starting solution on the physical properties of fluorine doped zinc oxide films deposited by a simplified spray pyrolysis technique," *Superlattices Microstruct.*, vol. 51, no. 5, pp. 680–689, 2012, doi: 10.1016/j.spmi.2012.02.006.

[22] T. Bakos, S. N. Rashkeev, and S. T. Pantelides, "Reactions and Diffusion of Water and Oxygen Molecules in Amorphous [Formula presented]," *Phys. Rev. Lett.*, vol. 88, no. 5, p. 4, 2002, doi: 10.1103/PhysRevLett.88.055508.

[23] T. Arii and A. Kishi, "The effect of humidity on thermal decomposition of zinc acetylacetonate monohydrate," *J. Therm. Anal. Cal.*, vol. 83, pp. 253–260, 2006.

[24] S. A. Mauger, K. X. Steirer, J. Boé, D. P. Ostrowski, D. C. Olson, and S. R. Hammond,

"Effects of humidity during formation of zinc oxide electron contact layers from a diethylzinc precursor solution," *Org. Electron.*, vol. 31, pp. 63–70, 2016, doi: 10.1016/j.orgel.2016.01.012.

[25] W. H. Jeong, J. H. Bae, and H. J. Kim, "High-performance oxide thin-film transistors using a volatile nitrate precursor for low-temperature solution process," *IEEE Electron Device Lett.*, vol. 33, no. 1, pp. 68–70, 2012, doi: 10.1109/LED.2011.2173897.

[26] S. J. Heo, D. H. Yoon, T. S. Jung, and H. J. Kim, "Recent advances in low-temperature solution-processed oxide backplanes," *J. Inf. Disp.*, vol. 14, no. 2, pp. 79–87, 2013, doi: 10.1080/15980316.2013.806274.

[27] R. W. Schwartz, T. Schneller, and R. Waser, "Chemical solution deposition of electronic oxide films," *Comptes Rendus Chim.*, vol. 7, no. 5, pp. 433–461, 2004, doi: 10.1016/j.crci.2004.01.007.

[28] S. Park, C. H. Kim, W. J. Lee, S. Sung, and M. H. Yoon, "Sol-gel metal oxide dielectrics for all-solution-processed electronics," *Mater. Sci. Eng. R Reports*, vol. 114, pp. 1–22, 2017, doi: 10.1016/j.mser.2017.01.003.

[29] G. Selvan, M. P. Abubacker, K. Usharani, and A. R. Balu, "Precursor aging effect on the properties of CdZnS films," *Surf. Eng.*, vol. 32, no. 3, pp. 212–217, 2016, doi: 10.1080/02670844.2015.1111559.

[30] A. Takagi, K. Nomura, H. Ohta, H. Yanagi, T. Kamiya, M. Hirano, and H. Hosono, "Carrier transport and electronic structure in amorphous oxide semiconductor, a-InGaZnO4," *Thin Solid Films*, vol. 486, no. 1–2, pp. 38–41, 2005, doi: 10.1016/j.tsf.2004.11.223.

[31] C. C. Hsu, J. K. Sun, C. C. Tsao, and Y. T. Chen, "Effects of sol aging on resistive switching behaviors of HfOx resistive memories," *Phys. B Condens. Matter*, vol. 508, no. December 2016, pp. 98–103, 2017, doi: 10.1016/j.physb.2016.12.023.

Chapter 4 Analysis of Machine learning for Fermi level engineering

4.1 Introduction

Ultra-wide bandgap (UWB) oxide semiconductors have gained great attention for optoelectronic device applications owing to their unique combination of electrical conductivity and optical transparency [1]. It has been widely used in various device applications such as thin film transistors (TFTs), sensors, and solar-blind photodetectors (SBPDs) [2][3][4][5][6]. In particular, UWB amorphous gallium oxide (a-Ga_2O_x) is the most superb candidate for future device applications due to its excellent optical properties (E_g = 4.8 eV), high film uniformity, high breakdown voltage, harsh-environment resistivity, cost-effectiveness and flexibility in device design [2] [3][7][8]. Moreover, it exhibits decent performance which is comparable to single crystalline gallium oxide in selected applications [2][7]. Nonetheless, as-deposited a-Ga_2O_x-based devices exhibit poor device performance which is highlighted as the major drawback. Apparently, Fermi level engineering is an appropriate method to modified solution-processed UWB a-Ga_2O_x as explained in Chapter 2. As the H-dopant was introduced and occupied the donor level, the electrical properties were significantly improved [3] from insulator to a semiconductor. Likewise, the device performance was also improved.

For *n*-type semiconductor such as a-Ga_2O_x [7], excess electron carrier concentration is required to enhance electrical properties which further exhibit better device performance. Thus, quantifying and controlling the number of electron carrier concentration is a critical consideration for fabricating a-Ga_2O_x-based devices. One method to quantify the carrier concentration of materials is through Hall effect measurement. Hall effect can describe the movement of charge carriers through a material when a perpendicular magnetic field is introduced. This phenomenon was first introduced by Edwin Hall in 1879, and has been widely used to quantify carrier concentration for various oxide semiconductor materials [6][9][10][11][12][13][14][15][16]. Nevertheless, due to equipment limitations, performing Hall effect measurement for insulating UWB a-Ga_2O_x is quite challenging [3]. UWB a-Ga_2O_x has a complex combination of ultra-wide bandgap (E_g = 4.8 eV), structural randomness of amorphous nature, low carrier concentration, and high resistivity which makes it difficult to be measured.

As an alternative, the carrier concentration can be identified by estimating the Fermi level (E_F) relative position. For *n*-type semiconductor, the carrier concentration represents as electron carrier concentration which is expressed by the following equation:

$$n = N_C e^{-(E_C - E_F)/kT} \quad \textbf{(4.1)}$$

where n is electron carrier concentration, N_C is density of state in the conduction band, E_C is conduction band energy, E_F is Fermi energy, k is Boltzmann constant, and T is temperature in Kelvin degree. This equation means that the higher electron carrier concentration is reflected as the E_F is close to the conduction band minimum (CBM). As the E_F shifts closer to the valence band maximum (VBM), the electron carrier concentration is lower. Whereas for *p*-type semiconductor, the dominant mobile carrier is represented as hole carrier concentration (p) which is expressed by this equation:

$$p = N_V e^{-(E_F - E_V)/kT} \quad \textbf{(4.2)}$$

where p is the hole carrier concentration, N_V is density of states in the valence band, and E_V is valence band energy. As the E_F is closer to the VBM, the hole carrier concentration is higher. Otherwise, lower hole carrier concentration is reflected as E_F shifts towards the CBM. To further understand the different between electron and hole carrier concentration, the concept of energy band diagram was illustrated in ***Figure 4.1***.

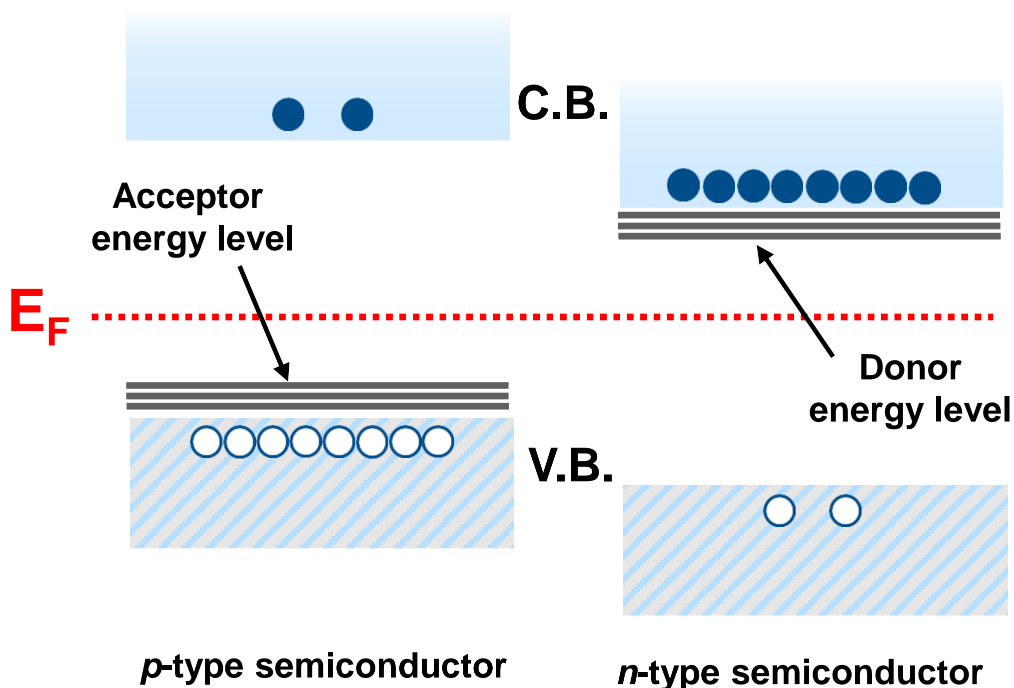

Figure 4.1. Energy band diagram of *p*-type and *n*-type semiconductor.

By understanding this concept, a facile method to modify UWB a-Ga_2O_x material can be developed, for instance by shifting the E_F relative position. Several research approaches have been demonstrated to shift the E_F relative position of oxide materials such as thickness modification [17], temperature modification [18][19], and hydrogen doping incorporation [3]. In particular, as explained in Chapter 2, the hydrogen doping incorporation method has successfully modified solution-processed UWB a-Ga_2O_x by shifting the E_F as close as 1.18 eV toward the CBM. Likewise, this E_F shifting phenomena has further improved the electrical properties and exhibited semiconductor behavior of solution-process UWB a-Ga_2O_x. Aside from hydrogen-incorporation method, thickness modification and temperature modification can also be applied as an alternative method to obtain optimized E_F relative position.

Nevertheless, experimental methods require complex optimization, have intensive material resource usage, and are time-consuming to obtain the optimized E_F result. Therefore, simulation approach is necessary to accelerate material design and device fabrication such as density functional theory (DFT). DFT has been widely used to calculate optical and electrical properties of various materials [20][21][22][23]. Nonetheless, DFT calculation is generally expensive, particularly in case of large supercell requirement, charge states, explicit image charge correlations [20], and an advance level of theory such as GW corrections [24] or hybrid functionals [25]. In addition, it is quite challenging to demonstrate DFT calculation for amorphous materials. Thus, machine learning is proposed as an alternative method for rapid and cost-effective optimization of E_F prediction of amorphous materials, particularly solution-processed UWB a-Ga_2O_x.

Section 4.2 presents the recent progress on machine-learning-assisted method in materials science and how it works in predicting the optical and electrical properties of various materials. Specifically, the E_F prediction *via* supervised machine learning will also be discussed in detail. In contrast, experimental approach of E_F estimation will be discussed in section 4.3. Likewise, this section will compare two E_F estimation approaches: experimental and simulation approaches in general. The advantages and disadvantages of both methods will be discussed. Several machine learning regression models which is likely appropriate for solution-processed UWB a-Ga_2O_x will be discussed in section 4.4. And eventually, the machine-learned E_F prediction of solution-processed UWB a-Ga_2O_x films will be discussed in section 4.5.

4.2 Recent progress of machine learning approach in materials science

To date, machine learning is gaining traction in materials science and engineering due to its short time consumption, cost-effectiveness, large prediction area, and low material resource requirement. Machine learning has become a promising method for materials design which has been widely used in predicting optical [26] and electrical properties [27], as well as accelerating materials [28] and experimental design [22]. Fernandez *et al.* in 2016 demonstrated the electrical properties prediction of graphene material using machine learning algorithms. The electrical properties such as electron affinity (E_A), energy of Fermi level (E_F), electron bandgap (E_g) and ionization potential (E_I) are calibrated with structural features of 70% of dataset describing more than 70% of cross-validation variance. Machine learning models showed accurate prediction with a strong correlation of R^2 ~90% [27].

In 2020, Regonia *et al.* presented the implementation of supervised machine learning to predict the optical bandgap energy (E_g) of ZnO material. It showed that developing mathematical models of ZnO nanostructures *via* machine learning can significantly accelerate the production of ZnO-based devices and applications [26]. This report reveals that by adding diverse data, collinearity which reduces the model accuracy can be prevented. Moreover, Ramprasad and colleagues [28] demonstrated machine learning as a powerful method to accelerate design of polymer dielectrics. Similarly, Talapatra *et al.* was also demonstrated machine learning as an autonomous and adaptive learning method on accelerating experimental design [22].

Nowadays, machine learning has become an integral component of material design [29]. Researchers have extracted the models and design rules from material data to drive accelerated discovery. The machine-learning-based design of materials design in material science was illustrated in ***Figure 4.2***. The data set consist of materials which is referred to as "input, and the property of interest is referred as the "target" or "output (***Figure 4.2***a). ***Figure 4.2***b illustrates the learning problem when the problem is defined as follows:

$$Given\ a\ \{material \rightarrow property\} data\ set \quad \textbf{(4.3)}$$

what is the best estimate of the property for a new material that have not been defined in the original data set? To address that problem, all data-driven strategies are composed of two distinct steps. First, the input cases (materials) are represented as numerical data set. At the end of this step, each input case would have been reduced to a string of number (fingerprints) as

illustrated in ***Figure 4.2***c. The second step establishes a mapping between the fingerprinted input and target property which are entirely numerical in nature.

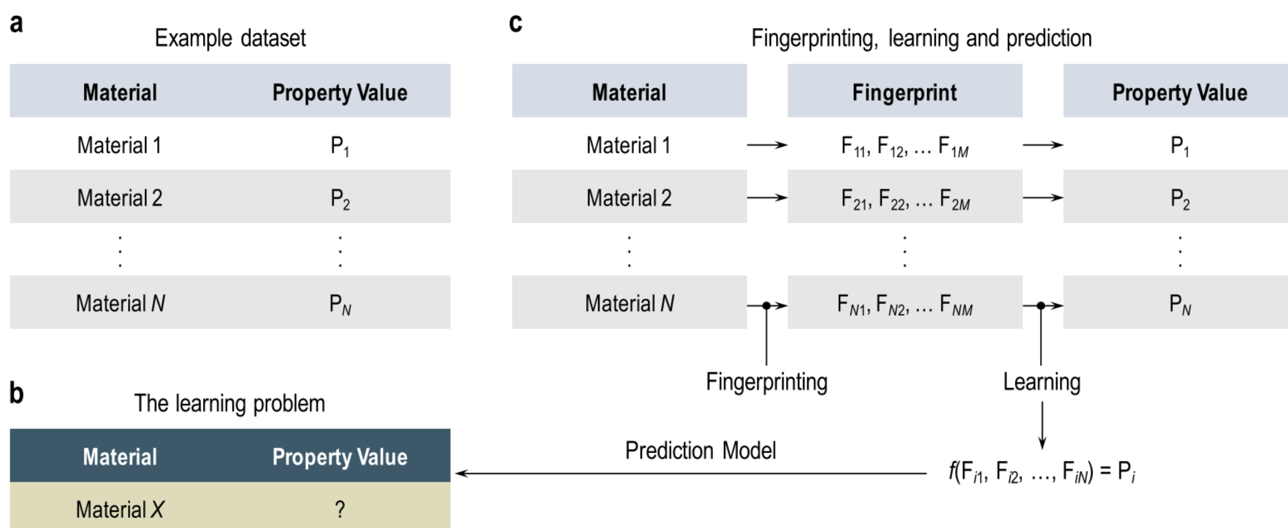

Figure 4.2. (a) Schematic view of an example data set, (b) statement of the learning problem, and (c) creation of a surrogate prediction model *via* the fingerprinting and learning steps [29].

As an example, complex polymers are 'fingerprinted' as simple, easily attainable numerical representations, which are mapped to the properties of interest (Y) using machine learning algorithm to develop an on-demand property prediction model as displayed in ***Figure 4.3***. The different steps are involved in generating the database of the properties of 4-block polymers *via* DFT calculation (***Figure 4.3***a). Afterwards, the DFT calculated result were plotted in ***Figure 4.3***b. While the Pearson correlation coefficient between fingerprint and properties was displayed in ***Figure 4.3***c. And eventually, the correlation between fingerprint component and the properties was represented in the form of heat maps. Where the red crosses represent the components which lead to unstable polymers and were not considered in the present study.

In particular, machine learning has been used to predict the E_F of graphene nanoflakes with a model accuracy > 90% [27][30]. The best of our knowledge, there is no reported work of supervised machine learning of solution-deposited amorphous UWB material. Thus, this study will be a premier work on applying machine learning for E_F prediction of solution-processed UWB a-Ga_2O_x.

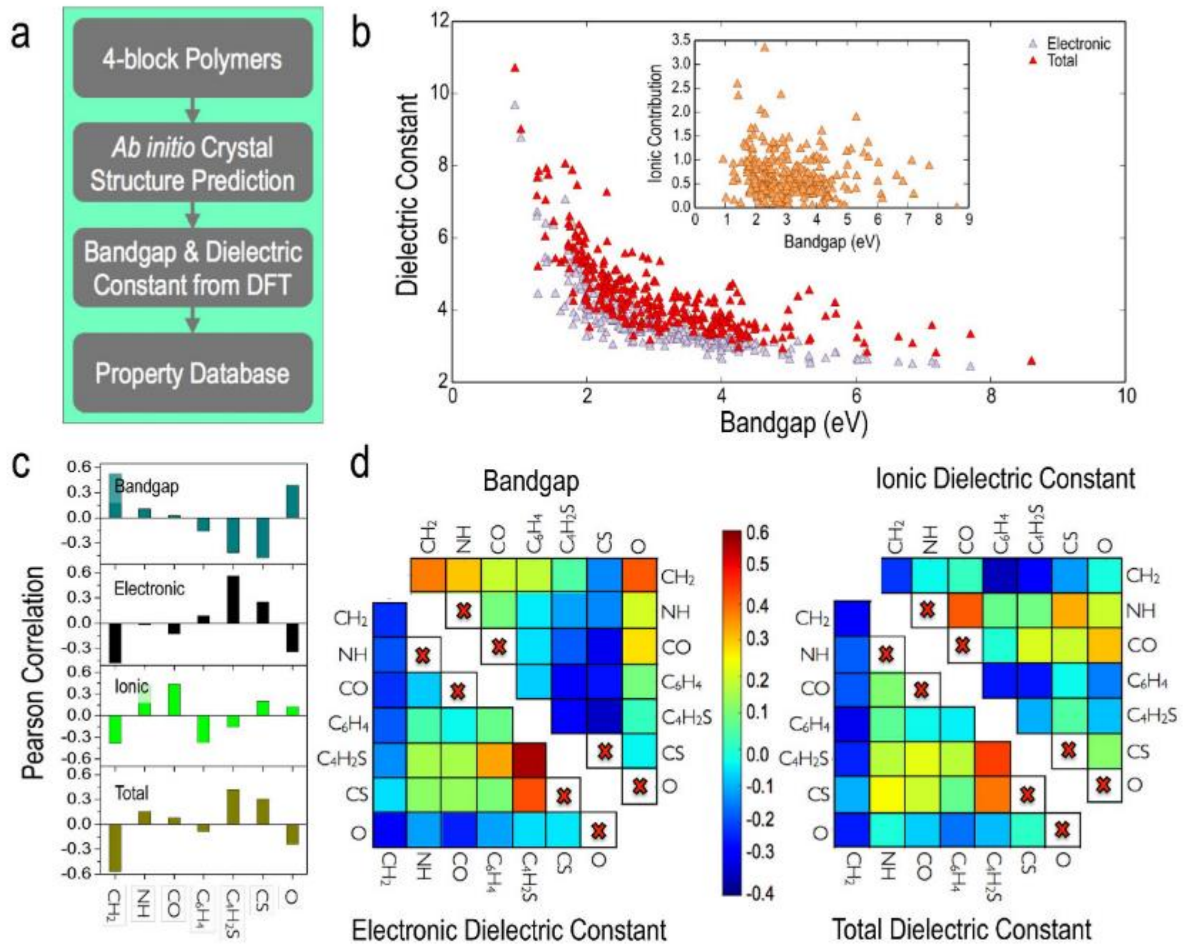

Figure 4.3. (a) Generating a database, (b) the DFT computed electrical properties, (c) the Pearson correlation coefficient, and (d) the heat map of fingerprint and properties [28].

4.3 Fermi level estimation methods

As explained in section 4.1, obtaining the E_F relative position is crucial for material design. By modifying the E_F, the optical and electrical properties of oxide semiconductor material will be enhanced. In general, E_F relative position can be estimated through experimental and simulation approaches. The detail of both approaches will be discussed in this section.

4.3.1 Experimental approaches

The experimental approach to estimate the E_F is illustrated in ***Figure 4.4***. Prior to the calculation, the optical bandgap energy (E_g) was determined by Tauc plot relation of UV-Visible spectra using Equation 2.1. ***Figure 4.4***a displayed the Tauc plot of an a-Ga_2O_x/glass

sample. The x-intercept was determined by fitting a straight line towards the x-axis. An obtained x-intercept of 5.0 eV was defined as the E_g. Afterwards, the valence band offset ($E_{V\text{-}offset}$) was determined from the XPS spectra. The $E_{V\text{-}offset}$ is a level energy which implies the energy difference between E_F and VBM. Its value can be estimated by taking the x-axis intercept where x = 0 at low binding energy of around 0 – 10 eV. In ***Figure 4.4***b, the $E_{V\text{-}offset}$ was obtained at 2.9 eV. Eventually, the E_F was estimated by subtracting E_g and $E_{V\text{-}offset}$ using Equation 2.2 and resulting E_F position of 2.1 eV relative to the CBM as shown in ***Figure 4.4***c.

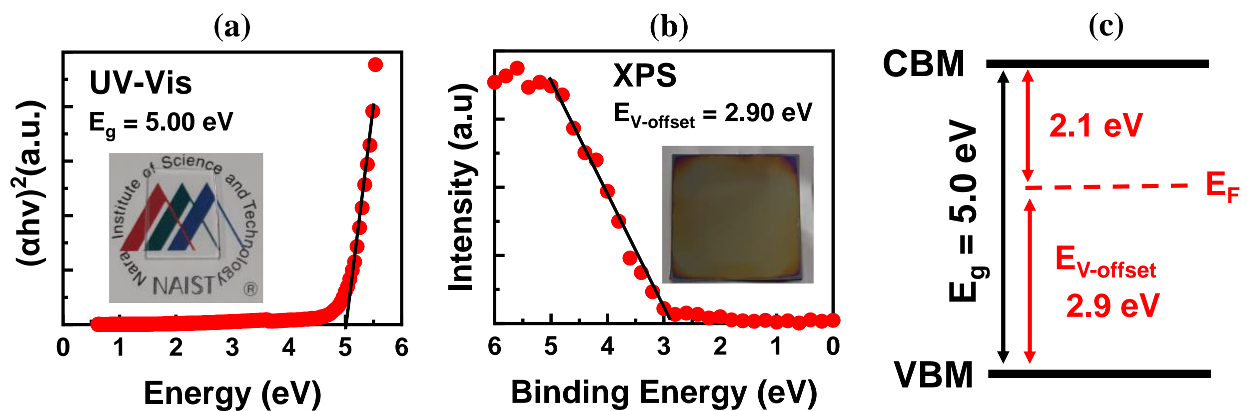

Figure 4.4. (a) Tauc plot for E_g estimation, (b)Valence band for $E_{V\text{-}offset}$ estimation, and (c) E_F estimation from experimental approach. Inset: the a-Ga_2O_x/glass and a-Ga_2O_x/SiO_2/Si samples that were used for film characterization on (a) UV-Vis and (b) XPS respectively.

In general, there are three critical points of this experimental approach. First, the experimental data should be valid, especially the $E_{V\text{-}offset}$ value. Charge neutralization should be applied for insulating samples [31] for accurate estimation. Second, this estimation should be applied for numerous sample conditions to obtain accurate E_F estimation. It means that the estimation time will be highly time consuming. In consequence, for a frequent experiment, an intensive material resources are needed. Thus, by considering those issues, machine learning approach is apparently much more appropriate and powerful to obtain an optimized E_F value.

4.3.2 Machine learning approaches

In machine learning approach, a diverse data of experimental parameters from various valid sources were prepared. The experimental parameters (referred to as features X) are mapped into expected resulting properties (referred to as target or predicted values Y). For target variables with continuous value, the mapping X→Y may be performed with appropriate regression techniques. The detail of the machine learning work principle was explained in section 4.2.

As compared to the experimental approach, machine learning offers short time consumption, cost-effectiveness, large prediction area by using minimum material resources. Nevertheless, machine learning has low environment dependency which is the consequence of ideal condition in simulation environment. For instance, a temperature of 380 °C was applied to generate the metal-oxide bond formation of a-Ga_2O_x film. The machine would note and understand that 380 °C is an absolute parameter to generate metal-oxide formation. In reality, metal-oxide formation is influenced by many factors, not only the temperature. The effect of atmosphere ambient, relative humidity, chemical reaction, precursor aging, and any other complex undefined parameters are neglected. In contrast, experimental approach are greatly realistic where every single detail on the experimental condition which might affect the result, will be included. The comparison of both approaches is summarized in ***Table 4-1***.

Table 4-1. Comparison of experimental and machine learning approach.

Aspects	Experimental	Machine Learning
Time consumption	Long (month)	Short (day)
Cost consumption	High	Low
Prediction area	Small	Large
Material resources	High	Low
Environment dependence	High	Low

For a comprehensive result, herein both approaches were merged as illustrated in ***Figure 4.5***. A highly realistic data will be used as an input of machine learning pipeline instead of simulation-based data such as DFT data. Afterwards, to cut-off the time consumption, the machine learning approach will be used as an optimization method to obtain the predicted E_F value. In machine learning (ML) pipeline, the predicted E_F value was cross-validated by the machine and subsequently gives an output of predicted E_F data. Finally, the machine learning output was cross-validated by highly realistic experimental data. By applying this approach, I expect that the E_F predicted value meets the credibility in both material science and material informatics perspectives.

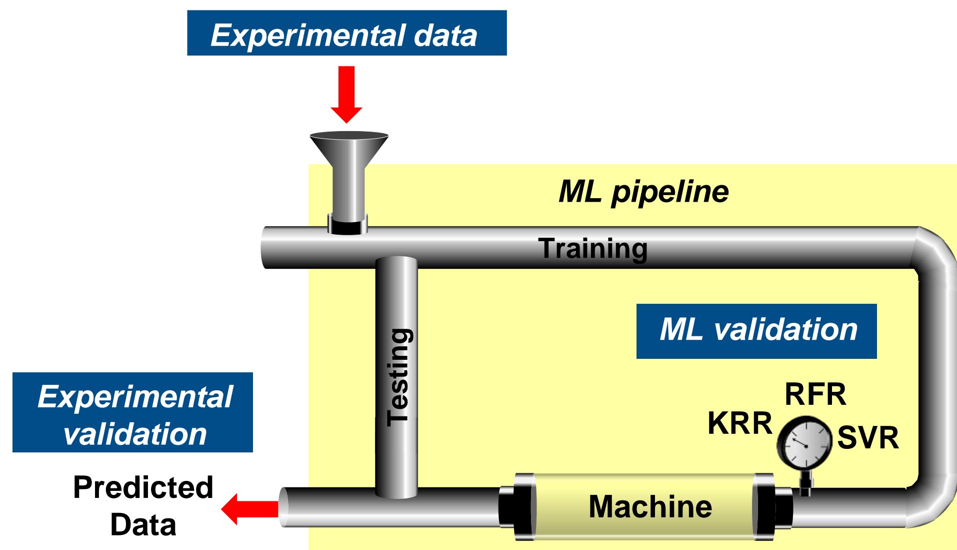

Figure 4.5. Schematic diagram of merged experimental and machine learning approach.

Additionally, in terms of materials science perspective, the chosen datasets must meet credibility and reasonability principles. Simulating untrusted data will lead to biased calculation and misinterpretation. For instance, a-Ga_2O_x is well-known as a UWB material, therefore the E_g should be higher than 4.0 eV. In many cases, a-Ga_2O_x bandgap is within 4.1 – 5.1 eV [6][7][32]. Therefore, the reported work of a-Ga_2O_x with E_g of 2.0 eV should be excluded since it is questionable.

Whereas from material informatic perspective, data separation of training and testing in the pipeline is a must since unseparated data leads to biased calculation. In other words, the credibility of the model performance will be in doubt. Hence, I applied both data selection and

data separation to guarantee the credibility and validity of our simulation result.

4.4 Machine learning regression models

In machine learning approach, regression model was used to map the features X into predicted values Y. Each model has their unique characteristics which make it appropriate to a specific data set, while it is not appropriate for other data sets [29]. Up to now, several regression models have been widely used for various prediction such as Kernel Ridge Regression (KRR) [26], Support Vector Regression (SVR) [27], and Random Forest Regression (RFR) [20].

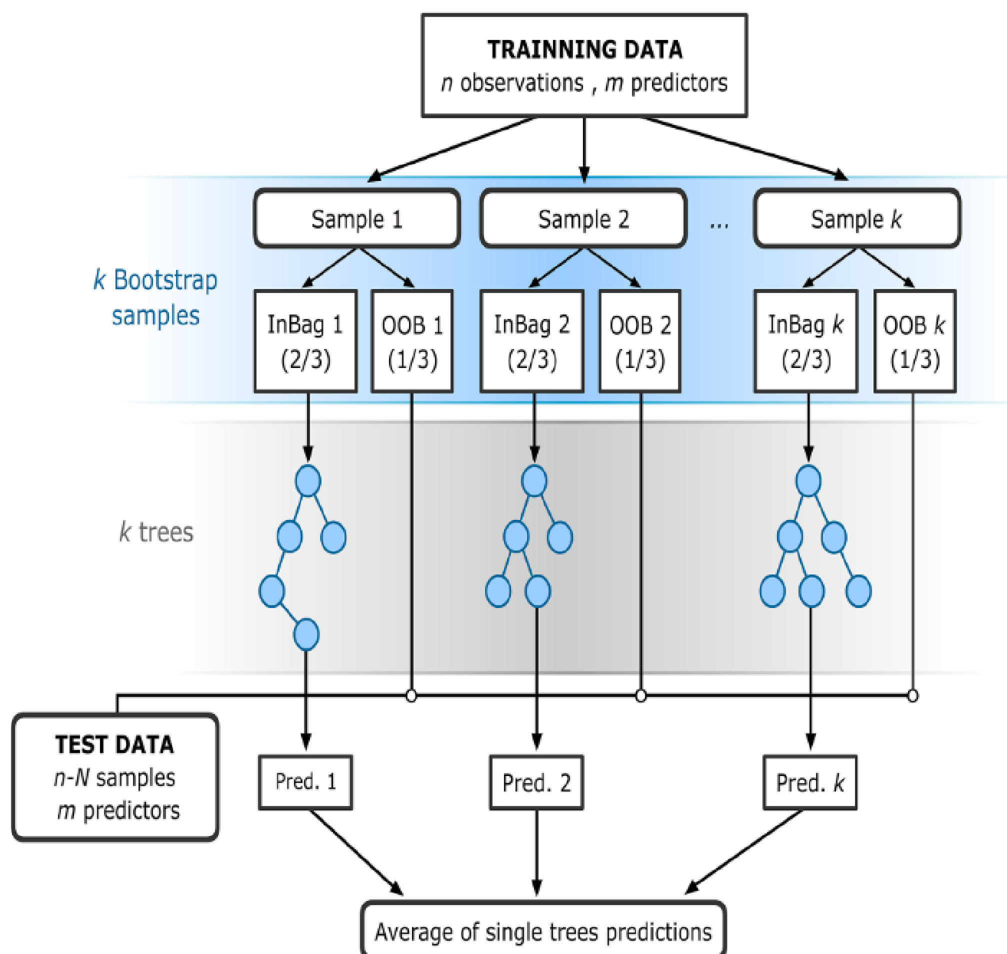

Figure 4.6. The flowchart of RFR [33].

KRR combines Ridge regression and classification with the kernel trick. It learns a linear function in the space induced by the respective kernel and the data. KRR is similar with SVR. Nevertheless, both regression models use different loss functions. KRR uses squared error loss, while SVR uses ϵ-insensitive loss. Moreover, the KRR fitting can be done in closed-form and it is typically faster for medium-sized data sets. Likewise, KRR learning model is non-sparse which implies slower prediction time as compared to SVR. In other words, KRR is faster in fitting, but SVR is faster in predicting owing to its sparse model [34].

Furthermore, RFR utilizes ensemble learning which fits a number of classifying decision trees on various sub-sample of data sets. It uses averaging to improve the predictive accuracy and control over-fitting. Compared to KRR and SVR, RFR has higher performance accuracy [35][36] and has been used to predict E_F of graphene nanoflakes with excellent accuracy of more than 90% [30]. In this study, those three regression models are used to predict the E_F of a-Ga_2O_x. Each model performance in predicting the E_F will also be evaluated.

4.5 Machine learning for Fermi level prediction of a-Ga_2O_x film.

This section demonstrates the machine-learned E_F prediction of solution-processed UWB a-Ga_2O_x. In particular, the analysis focused on the relationship between E_F (predicted value, Y) and experimental conditions (features, X) such as thickness, baking temperature, and environment gases during annealing of a-Ga_2O_x film. Prior to the machine learning simulation, an experimental data set of E_F value of a-Ga_2O_x were collected. Since there is a limited report on the dependency of fabrication parameters on the E_F of a-Ga_2O_x, additional experiment was conducted.

4.5.1 Sample preparation

The a-Ga_2O_x films fabrication steps were similar to ***Figure 2.6*** in section 2.3.3.2. Prior to the deposition, the Si/SiO_2 (p++) substrate and glass substrate were cleaned and exposed by UV/O_3 treatment (***Figure 4.7***a-b). The a-Ga_2O_x film was deposited *via* spin coating technique at 2000 rpm for 15 s followed by 2-step baking process at 150°C and 500 °C, 5 mins each. The a-Ga_2O_x film deposition was repeated to make multi-layers with varying thickness from 80 to 150 nm. The final post-baking was performed for 1 hour (***Figure 4.7***c). ***Figure 4.7***d displays additional annealing treatments that were performed by varying annealing temperature (300 to

900 °C) and ambient gases concentration (mix H_2/N_2, and pure N_2). Afterwards, the E_F of each sample was experimentally estimated through UV-Visible (UV-Vis) Spectrometer and X-ray Photoemission Spectrometer (XPS) as explained in section 4.3.1 (***Figure 4.7***e). The estimated E_F values as well as the varied experimental parameters were summarized in ***Table 4-2***. Those data were used as the main data source. Since there is only limited report on the fabrication parameters dependency of amorphous gallium oxide E_F, the literature data were mixed with the experimental data. In total, there were 31 data points, including 24 data points of this work or experiments (e) and 7 data points of reported work or literatures (L).

Three machine learning models (KRR, SVR, and RFR) were trained (***Figure 4.7***f), and the hyperparameters of each model were optimized with leave-one-out cross validation (LOOCV). Afterward, the models were evaluated using the following metrics: root mean square error (RMSE), mean absolute error (MAE), and coefficient of determination (R^2). RMSE measures the distance between the expected value and the predicted value of a sample. MAE expresses the absolute difference between the expected value and predicted value of a sample While R^2 express the accuracy of regression models in training the data set. The detail on the machine learning pipeline will be discussed in section 4.5.5.

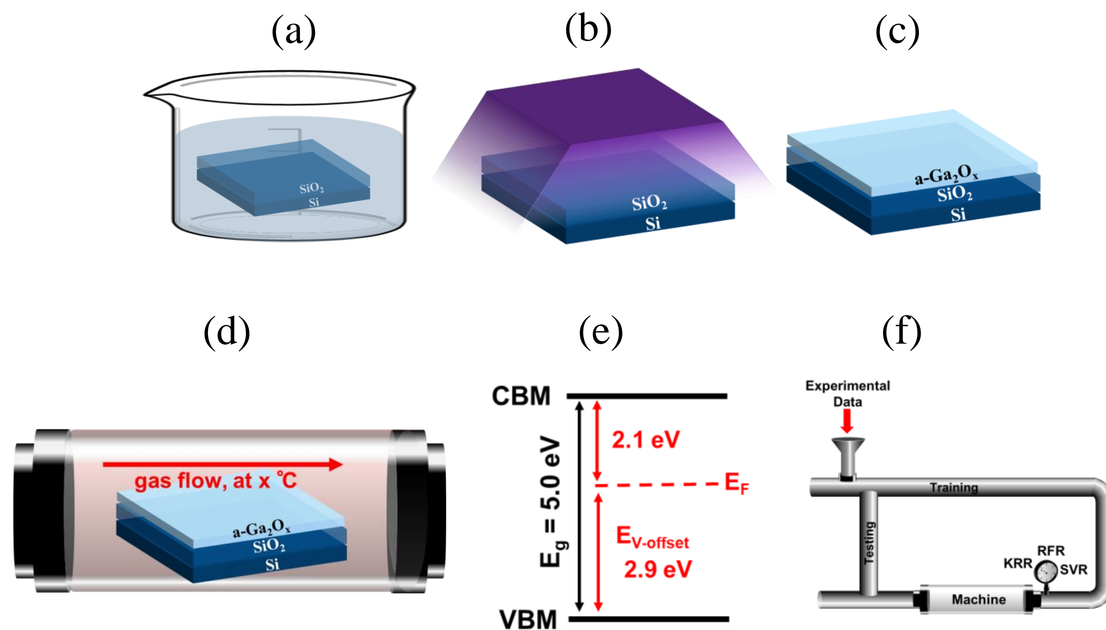

Figure 4.7. Schematic diagram for generating database of E_F value of a-Ga_2O_x films. Started by (a) substrate cleaning via SPM, (b) UV/O_3 treatment, (c) a-Ga_2O_x film formation, (d) H_2-annealing treatment, (e) Fermi level estimation, and (f) machine learning processing.

Table 4-2. Summary of E_F values of a-Ga_2O_x in various experimental conditions.

Sample	Thickness (nm)	Baking (°C)	H_2 (%)	N_2 (%)	Pure N_2 (%)	Eg (eV)	E_F (eV)
Train (E)	100	400	0	0	0	4.86	1.97
Train (E)	80	500	0	0	0	5.00	2.10
Train (E)	100	500	0	0	0	4.84	1.92
Train (E)	150	500	0	0	0	4.79	1.52
Train (E)	100	500	0	0	0	4.84	1.92
Train (E)	100	500	0.02	0.98	0	4.73	1.59
Train (E)	100	500	0.03	0.97	0	4.61	1.39
Train (E)	100	500	0	0	0	4.80	1.69
Train (E)	100	500	0	0.78	0	4.66	1.4
Train (E)	100	500	0.04	0.96	0	4.22	1.18
Train (L)	240	750	0	0	0	5.12	2.56
Train (L)	400	750	0	0	0	5.03	2.27
Train (L)	100	400	0	0	0	4.12	1.12
Train (L)	100	550	0	0	0	4.81	1.93
Train (L)	100	700	0	0	0	4.81	1.95
Train (L)	100	1000	0	0	0	4.9	2.13
Train (E)	80	500	0.04	0.96	0	4.73	1.61
Train (E)	80	500	0.04	0.96	0	4.69	2.1
Train (E)	80	500	0.025	0.975	0	4.46	1.57
Train (E)	80	500	0.035	0.965	0	4.39	0.73
Train (E)	80	700	0	0	0	4.79	2.09
Train (E)	80	800	0	0	0	4.69	1.64
Train (E)	80	900	0	0	0	4.81	2.00
Test (E)	100	300	0	0	0	4.98	1.66
Test (E)	100	500	0	0	0	4.84	1.92
Test (E)	120	500	0	0	0	4.83	1.9
Test (E)	100	500	0.04	0.96	0	4.54	1.36
Test (E)	100	500	0	0	1	4.60	1.72
Test (L)	800	750	0	0	0	4.91	2.46
Test (E)	80	500	0.04	0.96	0	4.66	1.69
Test (E)	80	600	0	0	0	4.89	1.79

4.5.2 Materials characterization

Material characterization is used to determine the E_g, $E_{V\text{-offset}}$, and to estimate the E_F as well. The E_g values were estimated by ultraviolet-visible spectroscopy (UV-Vis; JASCO ILN-472) Tauc plot. Whereas the $E_{V\text{-offset}}$ values were estimated by X-ray photoemission spectroscopy

(XPS; ULVAC-PHI 5000 VersaProbell). Afterwards, the E_F of each sample was obtained by subtracting the E_g and $E_{V-offset}$ as explained in section 4.3.1. The E_F of 24 data samples were obtained within 1.5-2 months of consecutive experiments. By considering the experimental time consumption, E_F prediction via machine learning will drastically accelerate the E_F prediction.

4.5.3 Experimental result

In term of thin-film transistor (TFT) devices, the thickness of the semiconductor channel film is a critical parameter since it has a strong correlation with the trap states inside the bulk film. A thinner film has more bulk traps and interface trap states which indicate lower carrier concentration. Otherwise, thicker film has excess carriers which contribute to negative shift of the threshold voltage (V_{th}) of the TFT devices [37][38][39]. Thus, determining an appropriate thickness of active channel material is crucial. Typically, a-Ga_2O_x-based devices have a semiconductor channel thickness of around 50 – 200 nm [6][5][40]. In particular, for ultra-wide bandgap material such as a-Ga_2O_x, electron conduction is difficult to obtain in a thicker film.

In this study, the thickness was varied from 80 – 150 nm and its correlation to the optical properties (E_g, film transparency and E_F) were further evaluated. As shown in ***Figure 4.8***a, the E_g and E_F were decreased as the thickness increased. Which suggests an improvement of carrier concentration as the E_F-CBM distance decreased. Moreover, similar trend was also observed in the previously reported work of β-Ga_2O_3 where the film thickness is inversely proportional to the E_g and E_F [41]. Furthermore, a-Ga_2O_x is well known for its excellent transparency (> 95%) due to its ultra-wide bandgap (E_g > 4.0 eV). Therefore, the reduction in the film transparency will significantly observed as the reduction in the E_g. **Figure 4.9**a displayed that the film transparency in the UV region (350 nm) was reduced from 99% to 90% as the thickness increased. The thicker film has lower film transparency which further expands the absorbance and implies E_g narrowing. Likewise, the reduction in film transparency might be attributed to free carrier absorption which is related to the improvement of the film carrier density [14]. The thicker film has more electron carrier concentration which implies more n-type semiconductor behavior [37]. This behavior was reflected as the reduction in the E_F-CBM distance.

Moreover, the E_g narrowing phenomena was also observed as the temperature increased (***Figure 4.8***b). At high temperature, many-body interactions between carriers in the conduction

band (CB) and valence band (VB) were increased which further reduced the E_g. This phenomenon is also known as bandgap renormalization [19].

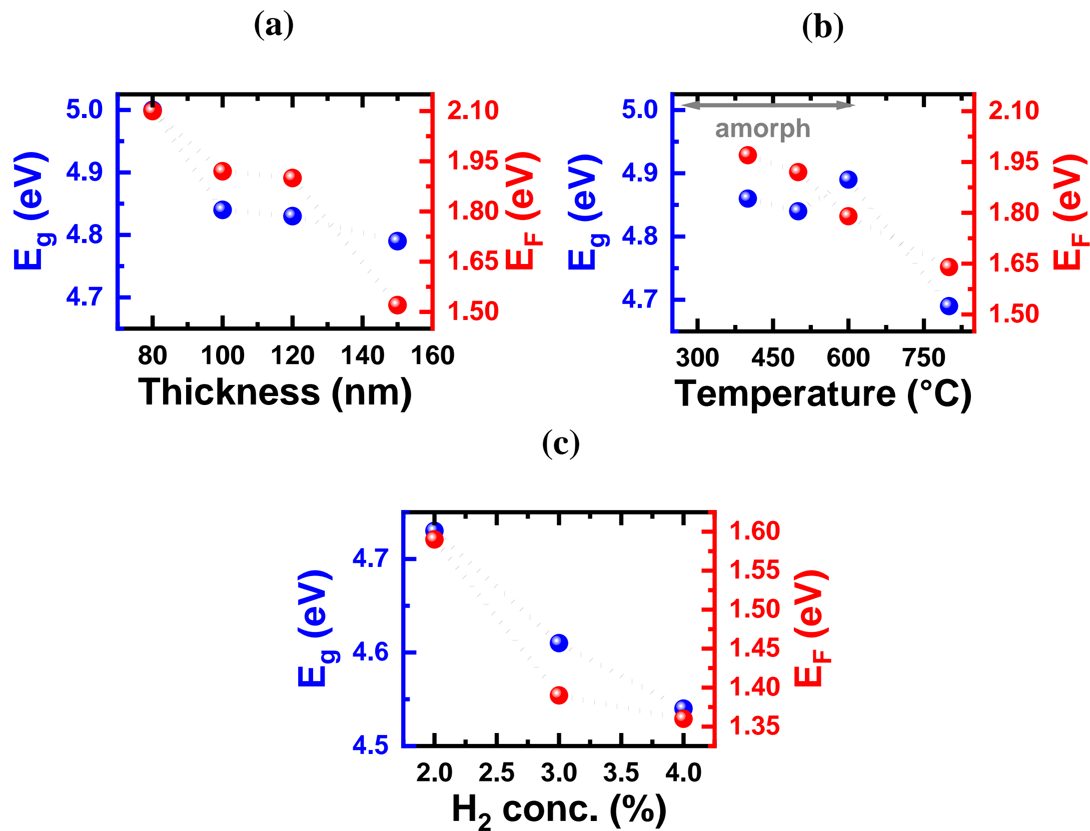

Figure 4.8. Relationship of experimental parameters to the E_g and E_F. (a) Film thickness, (b) baking temperature, and (c) H_2 gas concentration during annealing.

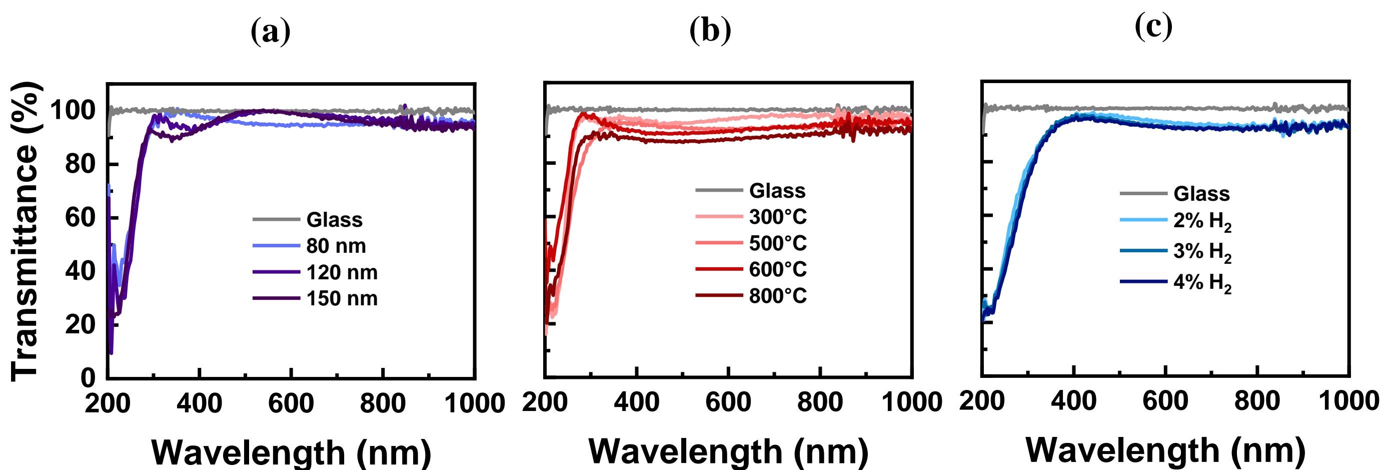

Figure 4.9. Transmittance of a-Ga_2O_x film at various experimental parameters. (a) Film thickness, (b) baking temperature, and (c) H_2 gas concentration during annealing.

Interestingly, the E_g rises abruptly at a temperature of 600 °C as the film started to transform its phase from amorphous to crystalline, and has a lower E_g at 700 °C owing to the crystalline phase. The TG-DSC shows that metal-oxide formation, film densification, and crystallization temperature occurred at temperatures of ~200 °C, ~380 °C, and ~680 °C respectively (***Figure 4.10***). At a temperature of 500 °C, the a-Ga_2O_x film phase was confirmed to be still amorphous by X-ray diffraction (XRD) measurements (***Figure 4.11***). Thus, it suggests that the film phase started to transform to crystalline phase at a temperature of ~600 °C.

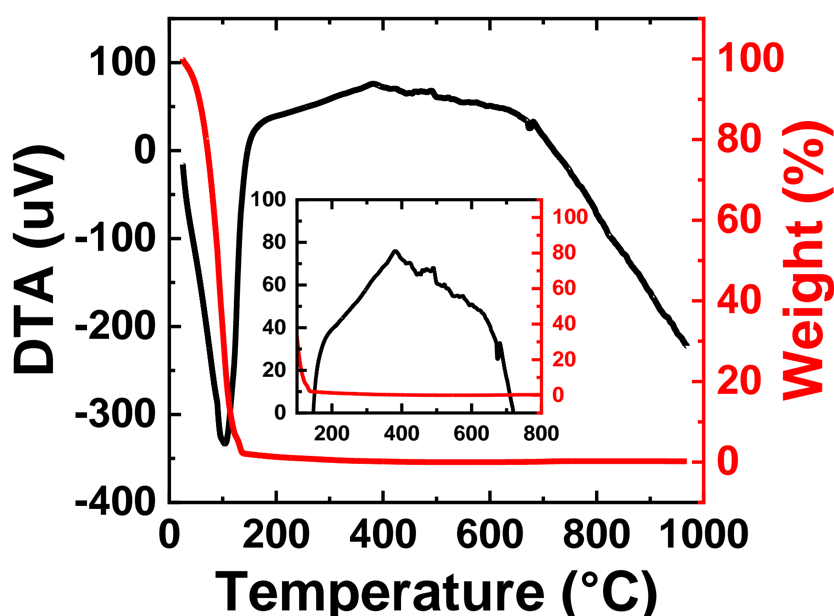

Figure 4.10. TG-DSC thermograph of Gallium oxide precursor.

Likewise, bandgap renormalization contributed to promoting excess carriers which further improve the electrical properties. This improvement was reflected in the reduction in E_F relative position (***Figure 4.8***b). Furthermore, the reduction in film transparency indicates the improvement of the film carrier density [14]. Thus, the film transparency reduction as temperature increases which is shown in **Figure 4.9**b suggests the improvement of the electrical properties of the film which agrees with the previous reported work [18]. Nonetheless, it needs to be highlighted that at high temperatures, the film tends to form a crystalline phase which leads to other problems such as structural defects and interfacial traps [3][42]. Thus, a baking temperature of < 600 °C is advisable since the film starts to crystallize

at ~600 °C.

Furthermore, as the H_2 gas concentration during annealing increased, the E_g also narrowed (***Figure 4.8***c). The reduction in the E_g was mainly due to carrier concentration induced by hydrogen doping. The hydrogen acts as a shallow donor which occupied donor level. Those electron carriers create additional states below CBM and further shift E_F close to the CBM [3][43]. The E_F shift, which is also supported by the reduction in film transparency (**Figure 4.9**c), implies electrical properties improvement. Thus, the E_F shifted closer to the CBM as the H_2 gas concentration increased. However, the H-incorporated needs to be implanted at considerable amount since excess H-incorporated tends to create interstitial defects [3][43].

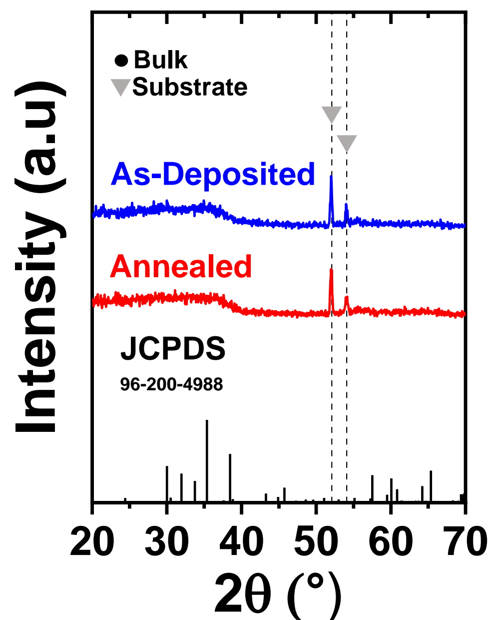

Figure 4.11. XRD spectra of a-Ga_2O_x film as-deposited film and annealed film at 500 °C.

Apparently, the E_F relative position to the CBM is a key strategy in enhancing the electrical properties of *n*-type semiconductors. Nevertheless, the E_F shifting phenomena has a complex relationship with experimental parameters (features) and E_g. Meaning, it is possible that 2 materials with exactly the same E_g have different E_F level values depending on many factors. Likewise, it is possible that cross interaction between features occurs during film fabrication. For instance, when depositing 80 nm-thick a-Ga_2O_x film, the precursor was deposited on a substrate and subsequently baked at 130 °C (pre-bake) and 500 °C (post-bake) multiple times until an 80 nm-thick film was formed. In this case, cross interaction between thickness and

temperature occurred. Both of these features not only affected the film formation and film properties but also E_F as well. Moreover, there is a more complex cross interaction for the H_2-annealed a-Ga_2O_x film since it involves thickness, baking temperature, annealing temperature, and H_2 gas concentration parameters. This cross interaction will further complicate the analysis of E_F shifting. Therefore, a study on E_F prediction via supervised machine learning will be useful and powerful.

4.5.4 Data set pre-processing

Machine learning simulation was started by determining the features and predicted variable. The feature variables are specific attribute values of a data sample, such as thickness, temperature, and other experimental parameters. On the other hand, the predicted variable is the corresponding target value of a set of features, which the model will try to predict. In this study, the predicted variable is E_F, while the features are film thickness, baking temperature and gas concentration as summarized in ***Table 4-2***. Since this study focused on solution-deposited film, controlling the film thickness is quite challenging. Therefore, several parameters are controlled to obtain a consistent film quality such as: number of layers, precursor volume per drop (30 μL), and spin rate (2,000 rpm, 15 seconds). Therefore, I assume that those films have same film quality as well as the film thickness.

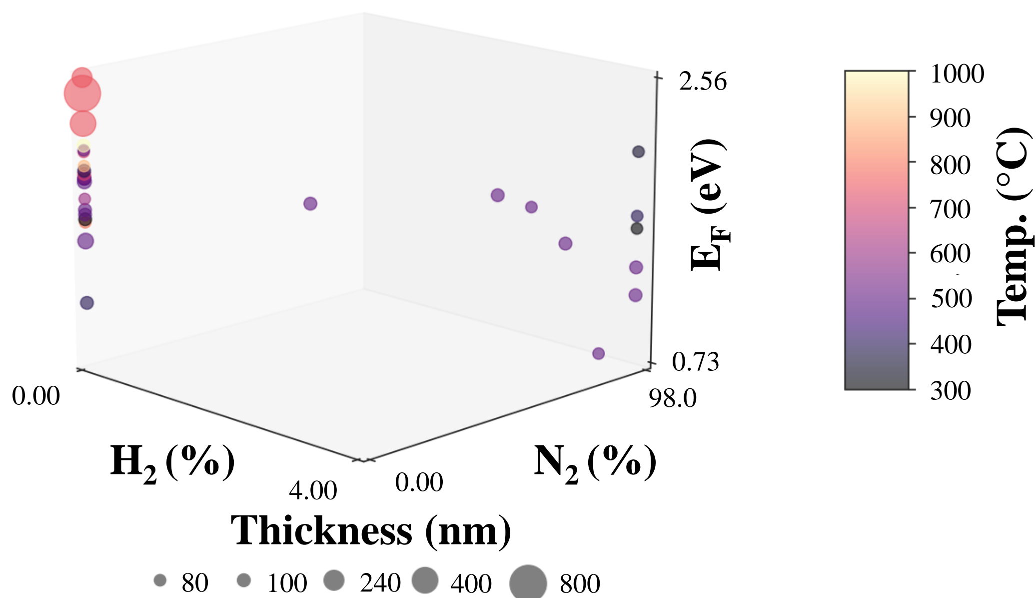

Figure 4.12. Datasets distribution.

The E_F data set of different fabrication parameters which are shown in ***Table 4-2*** were used as the main data source. The data set distribution can be seen in ***Figure 4.12***. The features–predicted correlation was evaluated by plotting the data set in Pearson and Spearman correlation plot as shown in ***Figure 4.13***. In this plot, the highest features–predicted correlation was indicated with a score value of 1 (proportional) and -1 (inversely proportional). Features with higher correlation (either 1 or -1) may imply higher probability of obtaining the best machine learning model performance. ***Figure 4.13*** showed that in both correlation plot, it has ~0.5 correlation value which implies that the data set is a good candidate for further training *via* machine learning.

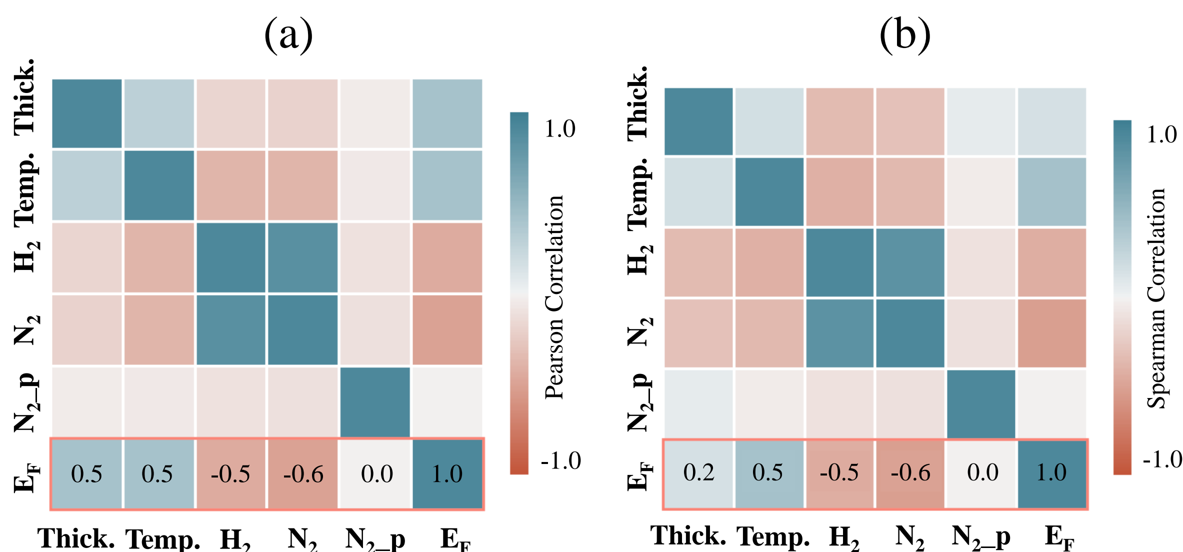

Figure 4.13. (a) Pearson and (b) Spearman correlation of features and predicted value (E_F).

4.5.5 Machine learning pipeline

The data set was introduced into machine learning pipeline and subsequently separated as 75% training and 25% testing to avoid bias during calculation. It should be noted that this step is important because unclear separation of training and testing data set will result in biased calculation and questionable model performance as explained in section 4.3.2. As illustrated in **Figure 4.14**, the training data was trained to obtain the hyperparameters of each machine learning model (***Table 4-3***). Hyperparameters control the learning process of a model. Different models may have unique hyperparameter configurations that need to be optimized on the

context of the data. Ideally, the hyperparameter optimization step is performed during the machine learning cross-validation step, which uses a separate data from the training and testing sets. However, since this study has a limited data set, LOOCV was used, which takes one sample at a time out of the training set to be used for cross-validation.

Herein, the following machine learning regression models were used: Kernel Ridge Regression (KRR), Support Vector Regression (SVR), and Random Forest Regression (RFR). Upon optimizing the hyperparameters of each model, the models were retrained on the entire training set. Then, each model was evaluated separately on the same testing data set. Three model performance metrics were used in this study: coefficient of determination (R^2), root mean square error (RMSE), and mean absolute error (MAE). The R^2 expresses the variation in the testing data set that the model can predict well. A high R^2 value (max value of 100%) means that the model perfectly fits the data. RMSE and MAE express the average magnitude of error of the model. A low error value (min value of 0) means that the model prediction is close to each testing sample. Since this is the first attempt in predicting Fermi level of solution-processed ultra-wide bandgap material, our target is to obtain R^2 = 90%, RMSE and MAE around ≤ 0.1.

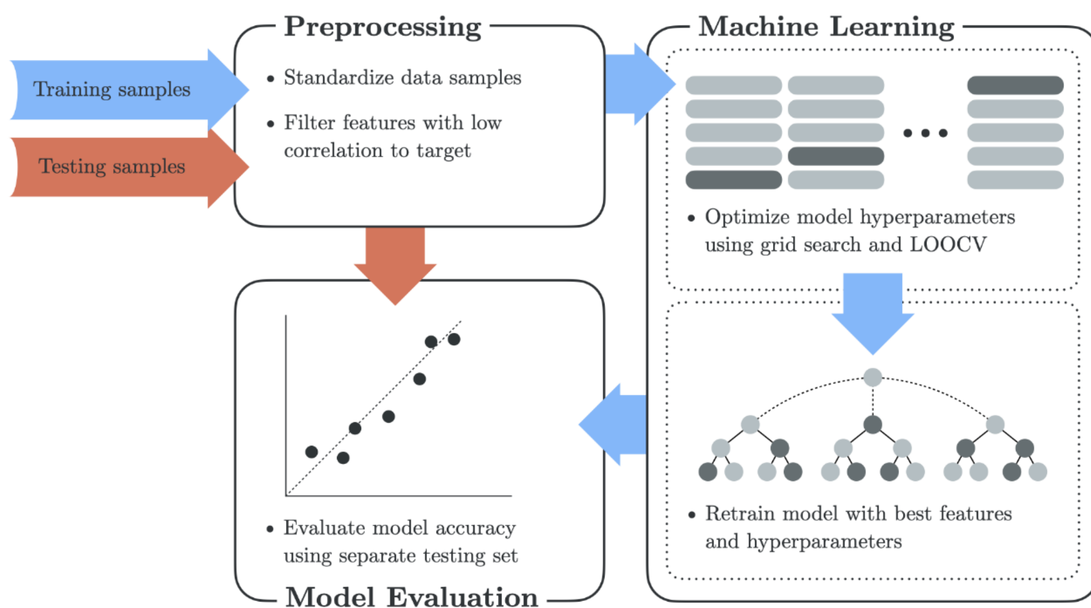

Figure 4.14. Machine learning pipeline for E_F prediction.

Table 4-3. Summary of hyperparameters of each machine learning regression model.

Hyperparameters	*KRR*	*SVR*	*RFR*
KRR_alpha	0.21		
KRR_gamma	0.10		
SVR_C		3.59	
SVR_gamma		0.02	
RFR_bootstrap			True
RFR_max-depth			5
RFR_n-estimators			100

The model performance scores are shown in ***Figure 4.15*** and summarized in ***Table 4-4***. ***Figure 4.15*** showed that RFR has the best regression model performance over 3 regression models. RFR successfully predicted E_F at ± 0.09 eV with 87% prediction model accuracy which is close with our target. As mentioned in section 2.5.3, the E_F has a complex combination with the E_g as well as the experimental parameters. Therefore, a complex regression model is preferred rather than simpler regression model. Herein, RFR is a more complex model than KRR and SVR. It uses ensemble learning methods that combines prediction from multiple machine learning decision trees, which makes it more robust than a singular model such as KRR. Evidently, KRR had the worst performance possibly due to underfitting, which happens when the model is too simple for the problem. In addition, SVR exhibit considerable performance of 72% accuracy, MAE of 0.13 and RMSE of 0.15. This indicates that SVR can be an alternative regression model aside from RFR.

Table 4-4. Summary of model performance of each machine learning regression model.

Regression	*RMSE*	*MAE*	R^2
KRR	0.26	0.16	0.19
SVR	0.15	0.13	0.72
RFR	0.10	0.09	0.87

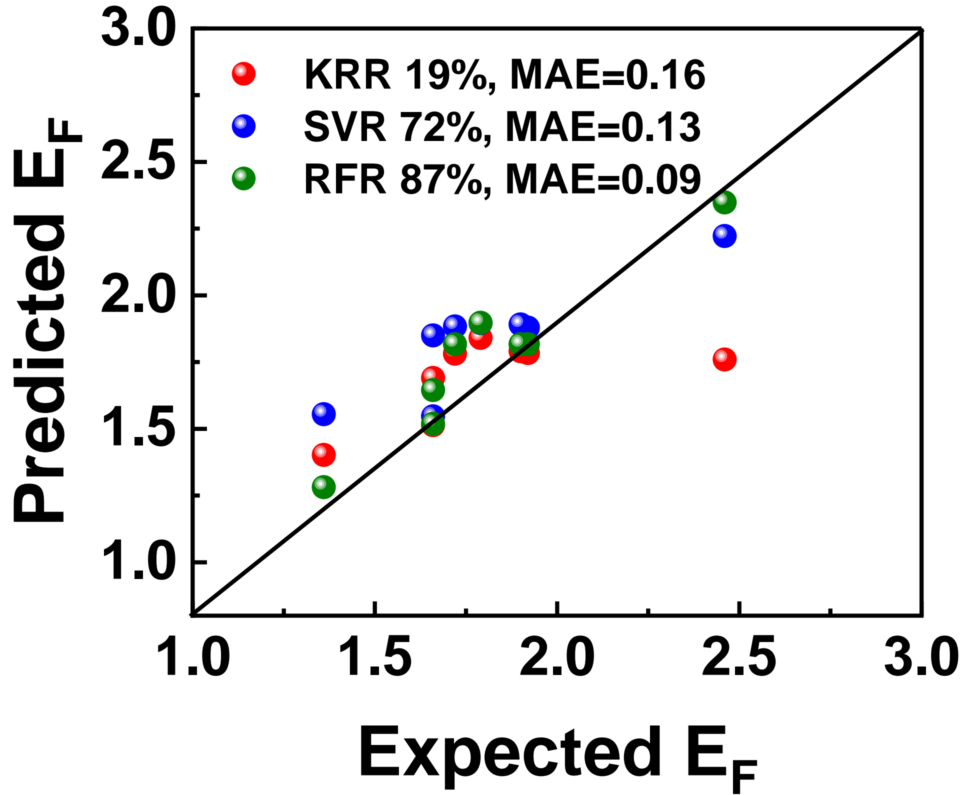

Figure 4.15. Summary of machine learning regression model performance.

To simulate the model on various experimental conditions, the best model (RFR) was retrained on the whole data set and then tested on a wider range of thickness, temperature, and H_2 gas concentration to obtain E_F predictions as illustrated in a slice plot in ***Figure 4.16***. The optimal E_F was searched in each range within 80 – 200 nm of thickness (700 steps), 300 – 1000 °C of annealing temperature (700 steps), and 0 – 4% H_2 percentage (700 steps). The N_2 percentage and N_2 pure were excluded during the simulation due to redundancy. The N_2 percentage is related to the H_2 concentration through the equation

$$N2\,\% + H2\,\% = 100\% \quad \textbf{(4.4.)}$$

$$N2\% = 1 - H2\% \quad \textbf{(4.5)}$$

Moreover, in material science perspective, the H_2 takes an important role in improving the electron carrier concentration. Thus, the "H_2" feature was remained, while the "N_2 pure" and "N_2" features were excluded.

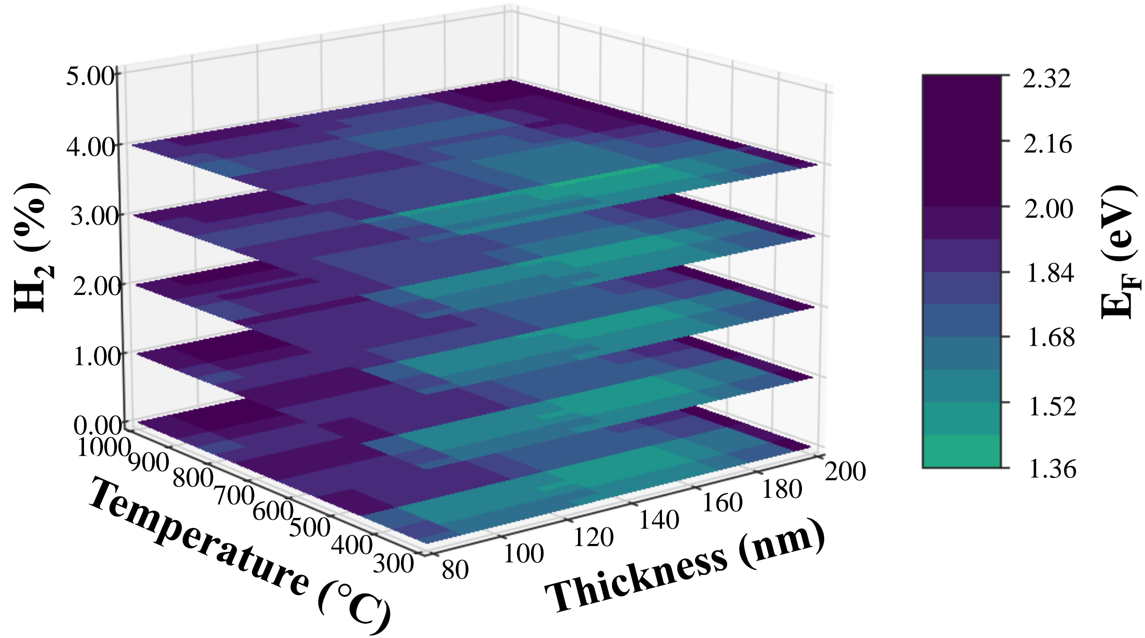

Figure 4.16. Wider E_F prediction range.

The E_F values were obtained in a range of 1.36 – 2.32 eV. The minimum E_F of 1.38 eV was successfully obtained with the best fabrication parameters of 90 nm-thick film deposited at 425°C under 4% H_2 gas-flowed during annealing (***Table 4-5***). In chapter 2, it was reported that the best experimental parameters for obtaining the minimum E_F are 100 nm film thickness, 500°C, and 4% H_2 gas to obtain an E_F of 1.18 eV. Thus, it suggests that the machine learning output result is quite near to the experimental result. Obtaining the minimum E_F is crucial for solution-processed UWB a-Ga_2O_x since it is related to the electron carrier concentration. For *n*-type semiconductor, especially a-Ga_2O_x, the electron carrier concentration tends to increase as the E_F shifts closer to CBM as explained above. In other words, lowest E_F will exhibit better device performance.

4.5.6 Experimental cross-validation

To further validate the machine learning output model performance, I subjected the best experimental parameters to further cross-validate via additional experimental approach (***Figure 4.5***). Note that the additional experimental cross-validation step (performed after testing) is different from the machine learning cross-validation step (performed during training).

Two additional films were deposited using the designated condition which had the best parameters in ***Table 4-5***. The film characteristics were further investigated by UV-Vis spectrometer and XPS to estimate the E_F of the film as explained in section 4.3.1.

The experimental cross-validation results were summarized in ***Table 4-5***. It showed that the experimental data were close to the machine learning output with an error of ~ 0.02 eV.

Table 4-5. Summary of experimental cross-validation.

Classification	Parameter	Test 1	Test 2
Data set	Total features	4	5
	Excluded features	-	Pure N_2
	Redundant features	N_2	Pure N_2, N_2
Output model performance	RFR R^2	75%	87%
	RFR RMSE	0.15	0.10
	RFR MAE	0.12	0.09
Output best parameters	Thickness	90 nm	135 nm
	Annealing	425 °C	425 °C
	H_2 percentage	4%	4%
	E_F output	1.38 eV	1.44 eV
Experimental cross-validation (CV)	E_F CV	1.40 eV	1.41 eV
	E_F CV error	0.02 eV	0.03 eV

These results show that machine learning regression models can be used to predict the E_F of solution-processed UWB a-Ga_2O_x film. By inputting fabrication parameters, it can predict the resulting E_F of the film and can also be used to identify which parameters will achieve the minimum E_F. Moreover, I expect that this approach will be useful in accelerating material design and device fabrication

4.6 Summary

In summary, E_F prediction *via* supervised machine learning approach has been successfully demonstrated for solution-processed UWB a-Ga_2O_x material. The results suggest that the minimum E_F can be obtained by training the experimental data set *via* machine learning. The

best model performance was exhibited by RFR with an RMSE of 0.10, MAE of 0.09, and model accuracy of 87%. The optimized E_F of 1.38 eV can be obtained with fabrication parameters of 90 nm film thickness, and 425°C annealing temperature under 4% H_2 gas concentration. The obtained E_F prediction values are meet the credibility in both experimental and machine learning simulation with a relatively low error of ~0.02 eV. Furthermore, the results of this work will be beneficial for the realization of a rapid and cost-effective optimization method of fabricating solution-processed UWB a-Ga_2O_x-based device.

In general, machine learning is a powerful method. Nonetheless, it has 2 critical issues that need to be considered. First, the machine tends to learn the data points and giving an output predicted data as an average value. In other words, the data points with high mode or repeatability will have a high change to be selected as an output. Second, the machine will search the predicted-value within a specific given range. In case of the minimum predicted value is out of range, the machine can not extrapolate to find the extreme value (minimum and maximum). Despite those issues, machine learning is beneficial for rapid estimation rather than experimental approach with excellent experiment-machine learning error of ~0.02 eV.

4.7 References

[1] J. Shi, J. Zhang, L. Yang, M. Qu, D. C. Qi, and K. H. L. Zhang, "Wide Bandgap Oxide Semiconductors: from Materials Physics to Optoelectronic Devices," *Adv. Mater.*, vol. 33, no. 50, pp. 1–30, 2021, doi: 10.1002/adma.202006230.

[2] H. Liang, Z. Han, and Z. Mei, "Recent Progress of Deep Ultraviolet Photodetectors using Amorphous Gallium Oxide Thin Films," *Phys. Status Solidi Appl. Mater. Sci.*, vol. 218, no. 1, p. 2000339, Jan. 2021, doi: 10.1002/pssa.202000339.

[3] D. Purnawati, J. P. Bermundo, and Y. Uraoka, "Insulator-to-semiconductor conversion of solution-processed ultra-wide bandgap amorphous gallium oxide via hydrogen annealing," *Appl. Phys. Express*, vol. 15, no. 2, p. 24003, 2022, doi: 10.35848/1882-0786/ac466a.

[4] Z. Han, H. Liang, W. Huo, X. Zhu, X. Du, and Z. Mei, "Boosted UV Photodetection Performance in Chemically Etched Amorphous Ga2O3 Thin-Film Transistors," *Adv. Opt. Mater.*, vol. 8, no. 8, Apr. 2020, doi: 10.1002/adom.201901833.

[5] Y. Qin, S. Long, Q. He, H. Dong, G. Jian, Y. Zhang, X. Hou, P. Tan, Z. Zhang, Y. Lu, C. Shan, J. Wang, W. Hu, H. Lv, Q. Liu, and M. Liu, "Amorphous Gallium Oxide-Based Gate-Tunable High-Performance Thin Film Phototransistor for Solar-Blind Imaging," *Adv. Electron. Mater.*, vol. 5, no. 7, Jul. 2019, doi: 10.1002/aelm.201900389.

[6] J. Kim, T. Sekiya, N. Miyokawa, N. Watanabe, K. Kimoto, K. Ide, Y. Toda, S. Ueda, N. Ohashi, H. Hiramatsu, H. Hosono, and T. Kamiya, "Conversion of an ultra-wide bandgap amorphous oxide insulator to a semiconductor," *NPG Asia Mater.*, vol. 9, no. 3, 2017, doi: 10.1038/am.2017.20.

[7] S. J. Pearton, J. Yang, P. H. Cary IV, F. Ren, J. Kim, M. J. Tadjer, and M. A. Mastro, "A review of Ga2O3 materials, processing, and devices," *Appl. Phys. Rev.*, vol. 5, p. 011301, 2018.

[8] X. Hou, X. Zhao, Y. Zhang, Z. Zhang, Y. Liu, Y. Qin, P. Tan, C. Chen, S. Yu, M. Ding, G. Xu, Q. Hu, and S. Long, "High-Performance Harsh-Environment-Resistant GaOX Solar-Blind Photodetectors via Defect and Doping Engineering," *Adv. Mater.*, vol. 34, no. 1, pp. 1–11, 2022, doi: 10.1002/adma.202106923.

[9] J. J. Dong, X. W. Zhang, J. B. You, P. F. Cai, Z. G. Yin, Q. An, X. B. Ma, P. Jin, Z. G. Wang, and P. K. Chu, "Effects of hydrogen plasma treatment on the electrical and optical properties of ZnO films: Identification of hydrogen donors in ZnO," *ACS Appl. Mater. Interfaces*, vol. 2, no. 6, pp. 1780–1784, 2010, doi: 10.1021/am100298p.

[10] E. Chikoidze, A. Fellous, A. Perez-Tomas, G. Sauthier, T. Tchelidze, C. Ton-That, T. T. Huynh, M. Phillips, S. Russell, M. Jennings, B. Berini, F. Jomard, and Y. Dumont, "P-type β-gallium oxide: A new perspective for power and optoelectronic devices," *Mater. Today Phys.*, vol. 3, pp. 118–126, 2017, doi: 10.1016/j.mtphys.2017.10.002.

[11] S. I. Oh, G. Choi, H. Hwang, W. Lu, and J. H. Jang, "Hydrogenated IGZO thin-film transistors using high-pressure hydrogen annealing," *IEEE Trans. Electron Devices*, vol. 60, no. 8, pp. 2537–2541, 2013, doi: 10.1109/TED.2013.2265326.

[12] K. Nomura, T. Kamiya, H. Yanagi, E. Ikenaga, K. Yang, K. Kobayashi, M. Hirano, and H. Hosono, "Subgap states in transparent amorphous oxide semiconductor, In-Ga-Zn-

O, observed by bulk sensitive x-ray photoelectron spectroscopy," *Appl. Phys. Lett.*, vol. 92, no. 20, 2008, doi: 10.1063/1.2927306.

[13] Y. Li, X. Hu, Z. Liu, and J. Ren, "Power and gas pressure effects on properties of amorphous In-Ga-ZnO films by magnetron sputtering," *J. Mater. Sci. Mater. Electron.*, vol. 23, no. 2, pp. 408–412, 2012, doi: 10.1007/s10854-011-0467-x.

[14] A. Takagi, K. Nomura, H. Ohta, H. Yanagi, T. Kamiya, M. Hirano, and H. Hosono, "Carrier transport and electronic structure in amorphous oxide semiconductor, a-InGaZnO4," *Thin Solid Films*, vol. 486, no. 1–2, pp. 38–41, 2005, doi: 10.1016/j.tsf.2004.11.223.

[15] Y. S. Lee, Z. M. Dai, C. I. Lin, and H. C. Lin, "Relationships between the crystalline phase of an IGZO target and electrical properties of a-IGZO channel film," *Ceram. Int.*, vol. 38, no. SUPPL. 1, pp. S595–S599, 2012, doi: 10.1016/j.ceramint.2011.05.105.

[16] C. J. Moon and H. S. Kim, "Intense Pulsed Light Annealing Process of Indium-Gallium-Zinc-Oxide Semiconductors via Flash White Light Combined with Deep-UV and Near-Infrared Drying for High-Performance Thin-Film Transistors," *ACS Appl. Mater. Interfaces*, vol. 11, no. 14, pp. 13380–13388, 2019, doi: 10.1021/acsami.8b22458.

[17] B. R. Tak, S. Dewan, A. Goyal, R. Pathak, V. Gupta, A. K. Kapoor, S. Nagarajan, and R. Singh, "Point defects induced work function modulation of β-Ga 2 O 3," *Appl. Surf. Sci.*, vol. 465, no. June 2018, pp. 973–978, 2019, doi: 10.1016/j.apsusc.2018.09.236.

[18] M. K. Yadav, A. Mondal, S. Das, S. K. Sharma, and A. Bag, "Impact of annealing temperature on band-alignment of PLD grown Ga2O3/Si (100) heterointerface," *J. Alloys Compd.*, vol. 819, p. 153052, 2020, doi: 10.1016/j.jallcom.2019.153052.

[19] J. W. Jeon, D. W. Jeon, T. Sahoo, M. Kim, J. H. Baek, J. L. Hoffman, N. S. Kim, and I. H. Lee, "Effect of annealing temperature on optical band-gap of amorphous indium zinc oxide film," *J. Alloys Compd.*, vol. 509, no. 41, pp. 10062–10065, 2011, doi: 10.1016/j.jallcom.2011.08.033.

[20] A. Mannodi-Kanakkithodi, M. Y. Toriyama, F. G. Sen, M. J. Davis, R. F. Klie, and M. K. Y. Chan, "Machine-learned impurity level prediction for semiconductors: the example of Cd-based chalcogenides," *npj Comput. Mater.*, vol. 6, no. 1, pp. 1–14, 2020, doi: 10.1038/s41524-020-0296-7.

[21] T. Kamiya, K. Nomura, and H. Hosono, "Subgap states, doping and defect formation energies in amorphous oxide semiconductor a-InGaZnO 4 studied by density functional theory," *Phys. Status Solidi Appl. Mater. Sci.*, vol. 207, no. 7, pp. 1698–1703, 2010, doi: 10.1002/pssa.200983772.

[22] A. Talapatra, S. Boluki, T. Duong, X. Qian, E. Dougherty, and R. Arróyave, "Autonomous efficient experiment design for materials discovery with Bayesian model averaging," *Phys. Rev. Mater.*, vol. 2, no. 11, pp. 1–18, 2018, doi: 10.1103/PhysRevMaterials.2.113803.

[23] M. Mohamad, B. Ul, R. Ahmed, A. Shaari, N. Ali, and R. Hussain, "Materials Science in Semiconductor Processing A density functional study of structural , electronic and optical properties of titanium dioxide : Characterization of rutile , anatase and brookite polymorphs," *Mater. Sci. Semicond. Process.*, vol. 31, pp. 405–414, 2015, doi: 10.1016/j.mssp.2014.12.027.

[24] F. Aryasetiawan and O. Gunnarsson, “The GW method,” *Reports Prog. Phys.*, vol. 61, no. 3, pp. 237–312, 1998, doi: 10.1088/0034-4885/61/3/002.

[25] J. Heyd, J. E. Peralta, G. E. Scuseria, and R. L. Martin, “Energy band gaps and lattice parameters evaluated with the Heyd-Scuseria-Ernzerhof screened hybrid functional,” *J. Chem. Phys.*, vol. 123, no. 17, 2005, doi: 10.1063/1.2085170.

[26] P. R. Regonia, C. M. Pelicano, R. Tani, A. Ishizumi, H. Yanagi, and K. Ikeda, “Predicting the band gap of ZnO quantum dots via supervised machine learning models,” *Optik (Stuttg).*, vol. 207, no. January, p. 164469, 2020, doi: 10.1016/j.ijleo.2020.164469.

[27] M. Fernandez, H. Shi, and A. S. Barnard, “Geometrical features can predict electronic properties of graphene nanoflakes,” *Carbon N. Y.*, vol. 103, pp. 142–150, 2016, doi: 10.1016/j.carbon.2016.03.005.

[28] A. Mannodi-Kanakkithodi, G. Pilania, T. D. Huan, T. Lookman, and R. Ramprasad, “Machine Learning Strategy for Accelerated Design of Polymer Dielectrics,” *Sci. Rep.*, vol. 6, no. January, pp. 1–10, 2016, doi: 10.1038/srep20952.

[29] R. Ramprasad, R. Batra, G. Pilania, A. Mannodi-Kanakkithodi, and C. Kim, “Machine learning in materials informatics: Recent applications and prospects,” *npj Comput. Mater.*, vol. 3, no. 1, 2017, doi: 10.1038/s41524-017-0056-5.

[30] M. Fernandez, A. Bilic, and A. S. Barnard, “Machine learning and genetic algorithm prediction of energy differences between electronic calculations of graphene nanoflakes,” *Nanotechnology*, vol. 28, p. 38LT03, 2017, doi: https://doi.org/10.1088/1361-6528/aa82e5.

[31] D. R. Baer, K. Artyushkova, H. Cohen, C. D. Easton, M. Engelhard, T. R. Gengenbach, G. Greczynski, P. Mack, D. J. Morgan, and A. Roberts, “XPS guide: Charge neutralization and binding energy referencing for insulating samples,” *J. Vac. Sci. Technol. A*, vol. 38, no. 3, p. 031204, 2020, doi: 10.1116/6.0000057.

[32] Y. Chen, Y. Lu, M. Liao, Y. Tian, Q. Liu, C. Gao, X. Yang, and C. Shan, “3D Solar-Blind Ga2O3 Photodetector Array Realized Via Origami Method,” *Adv. Funct. Mater.*, vol. 29, no. 50, pp. 1–8, 2019, doi: 10.1002/adfm.201906040.

[33] V. F. Rodriguez-Galiano, M. Sanchez-Castillo, J. Dash, P. M. Atkinson, and J. Ojeda-Zujar, “Modelling interannual variation in the spring and autumn land surface phenology of the European forest,” *Biogeosciences*, vol. 13, no. 11, pp. 3305–3317, 2016, doi: 10.5194/bg-13-3305-2016.

[34] K. P. Murphy, *Machine Learning: A Probabilistic Perspective*, vol. chapter 14. 2012.

[35] K. Fawagreh, M. M. Gaber, and E. Elyan, “Random forests: From early developments to recent advancements,” *Syst. Sci. Control Eng.*, vol. 2, no. 1, pp. 602–609, 2014, doi: 10.1080/21642583.2014.956265.

[36] M. Schonlau and R. Y. Zou, “The random forest algorithm for statistical learning,” *Stata J.*, vol. 20, no. 1, pp. 3–29, 2020, doi: 10.1177/1536867X20909688.

[37] S. Y. Lee, D. H. Kim, E. Chong, Y. W. Jeon, and D. H. Kim, “Effect of channel thickness on density of states in amorphous InGaZnO thin film transistor,” *Appl. Phys. Lett.*, vol. 98, no. 12, 2011, doi: 10.1063/1.3570641.

[38] E. N. Cho, J. H. Kang, and I. Yun, “Effects of channel thickness variation on bias stress instability of InGaZnO thin-film transistors,” *Microelectron. Reliab.*, vol. 51, no. 9–11, pp. 1792–1795, 2011, doi: 10.1016/j.microrel.2011.07.018.

[39] Y. Li, Y. L. Pei, R. Q. Hu, Z. M. Chen, Y. Zhao, Z. Shen, B. F. Fan, J. Liang, and G. Wang, “Effect of channel thickness on electrical performance of amorphous IGZO thin-film transistor with atomic layer deposited alumina oxide dielectric,” *Curr. Appl. Phys.*, vol. 14, no. 7, pp. 941–945, 2014, doi: 10.1016/j.cap.2014.04.011.

[40] T. Wang, H. Liang, Z. Han, Y. Sui, and Z. Mei, “Integrated Flexible Ga2O3 Deep UV Photodetectors Powered by Environmental Electromagnetic Radiation Energy,” *Adv. Mater. Technol.*, vol. 6, no. 3, Mar. 2021, doi: 10.1002/admt.202000945.

[41] B. R. Tak, S. Dewan, A. Goyal, R. Pathak, V. Gupta, A. K. Kapoor, S. Nagarajan, and R. Singh, “Point defects induced work function modulation of β-Ga 2 O 3,” *Appl. Surf. Sci.*, vol. 465, no. September 2018, pp. 973–978, 2019, doi: 10.1016/j.apsusc.2018.09.236.

[42] L. Yuan, S. Li, G. Song, X. wen Sun, and X. Zhang, “Solution-processed amorphous gallium oxide gate dielectric for low-voltage operation oxide thin film transistors,” *J. Mater. Sci. Mater. Electron.*, vol. 32, no. 7, pp. 8347–8353, Apr. 2021, doi: 10.1007/s10854-021-05408-5.

[43] J. Kim, S. Bang, S. Lee, S. Shin, J. Park, H. Seo, and H. Jeon, “A study on H 2 plasma treatment effect on a-IGZO thin film transistor,” *J. Mater. Res.*, vol. 27, no. 17, pp. 2318–2325, 2012, doi: 10.1557/jmr.2012.199.

Chapter 5 Summary

5.1 Conclusions

The field of TFT technology has been rapidly growing and unceasingly demanding for innovation. In line with innovation, the future electronic trends require highly transparent, cost-effective, large-area scalability, and harsh-environment-resistant material. However, the challenge is to improve the performance of those materials to be suitable with the current advance technology. Some of the important considerations to meet the future electronic devices lie in proper material selection, material design approaches, and interdisciplinary collaboration to resolve issues.

In this dissertation, a semiconducting solution-processed ultra-wide bandgap amorphous oxide material is developed via Fermi level engineering. The main findings and contributions of this research are summarized as follows:

I achieved semiconducting behavior of solution-processed a-Ga_2O_x material in Chapter 2. By utilizing Fermi level engineering as an attractive approach, insulating a-Ga_2O_x has been successfully conversed into its semiconducting state. Fermi level engineering is a technique for material design which rely on the Fermi level shifting phenomena. For n-type semiconductor such as a-Ga_2O_x, the E_F shifting phenomenon implies an increase in the electron carrier concentration which further improve the film conductivity and the TFT device as well. By varying experimental condition including: annealing ambient gases and temperature, E_F-CBM distances were minimized. Interestingly, semiconducting a-Ga_2O_x were successfully obtained as shown by TFT switching behavior which was achieved by performing annealing under 4% hydrogen ambient. E_F estimation via UV-Visible spectra and XPS reveal the Fermi level shifting phenomena which is mainly affected by the hydrogen doping.

I achieved semiconducting behavior of as-deposited solution-processed a-Ga_2O_x material in Chapter 3. One key to enhance the solution-processed oxide TFT is by minimizing the defects and impurities which comes from the deposition process. In Chapter 3, the effect of relative humidity on solution-processed a-Ga_2O_x thin film transistors was further evaluated. The water vapor (relative humidity) plays an important role in precursor hydrolysis, changing the decomposition pathway, the metal-oxide formation, the film thickness and device

performance as well. By monitoring and controlling relative humidity during thin film deposition, decent performance of as-deposited a-Ga_2O_x TFTs were achieved. Aside from the water vapor, the result also showed that the hydrogen annealing tends to enhance the device performances in selected cases. Finally, the result showed that hydrogen doping which drive the electron doping, might have originated from either hydrogen annealing or water vapor (humidity). Those hydrogen doping are vital factors to achieve the semiconducting behavior of as-deposited a-Ga_2O_x TFTs

I achieved an excellent Fermi level prediction of 87% accuracy by Machine Learning method in Chapter 4. To realize rapid and cost-effective optimization method in material design, Fermi level engineering *via* supervised Machine Learning was proposed in Chapter 4. In this chapter, machine learning approach was used for Fermi level prediction of a-Ga_2O_x films. By using regression models, experimental data was used as an input to further train the algorithm. The results show that machine learning models can be used to predict the E_F of ultra-wide bandgap a-Ga_2O_x film. Likewise, it can identify optimized fabrication parameters to achieve the minimum E_F value. This method will be beneficial for rapid and cost-effective optimization of UWB material design for future electronic applications.

In this study, Fermi level engineering through experiment and machine learning approaches is evaluated to obtain the target value of E_F ~0.4 eV. Despite the targeted value is not yet achieve, this study has been successfully achieved the minimum Fermi level value of 1.18 ~ 1.36 eV. This result is 1 order magnitude lower compare than the previous reported work of ultra-wide bandgap material [1]. It suggests that, our material is promising for electronic devices particularly optoelectronic devices.

5.2 Suggestions for future work

This work has shown the potential application of solution-processed a-Ga_2O_x which is modified *via* Fermi level engineering. Both experimental and simulation approaches were combined for a comprehensive study of solution-processed a-Ga_2O_x material. Nevertheless, there are still issues that need clarification and challenges that need to be overcome:

1. *Investigation of High-pressure Hydrogen Annealing (HPHA) of solution-processed a-Ga_2O_x material*

Ultra-wide bandgap amorphous material can attain electronic conduction only with difficulty because its ultra-wide bandgap leads to low electron carrier concentration and its amorphous structure lead to high electron trap density. By improving the film density, the electron trap density will significantly suppress. The hydrogen annealing has successfully converted an insulating a-Ga_2O_x to its semiconducting counterpart. We expect that by applying HPHA, the film density can be improved, and further improving the electrical properties of a-Ga_2O_x.

2. *Investigation of precursor aging time dependency of solution-processed a-Ga_2O_x film characteristics*

Precursor and solvent engineering apparently can significantly reduce the baking temperature of oxide material film by changing the decomposition pathway. Since there is a limited study on solution-deposited a-Ga_2O_x, a deep investigation of chemical reaction which might occur during precursor aging is interesting to investigate. Another solution deposition route to lowering the baking temperature is also interesting to be studied, such as solution combustion synthesis or aqueous solvent synthesis.

3. *Demonstration of density functional theory (DFT) for solution-processed a-Ga_2O_x material*

For a comprehensive understanding, a collaborative research which combine experimental and simulation approaches is highly recommended. An excellent result was successfully obtained by combining experimental-machine learning or DFT-machine learning separately. There is limited report which combine experimental-DFT-machine learning. Those combination will be a powerful method for material design and device application. However, the DFT simulation for solution-processed amorphous material is still extremely challenging. A breakthrough of a demonstration of experimental-DFT-machine learning approaches for solution-deposited amorphous material will be fascinating.

4. *Demonstration of Bayesian optimization for solution-processed a-Ga_2O_x material*

Solution-processed a-Ga_2O_x is immature material which has numerous parameters to be addressed. We found that there are many experimental parameters that needs to be optimized to obtain an excellent solution-processed a-Ga_2O_x film. Therefore, to further accelerate the material design, Bayesian optimization will be helpful. Bayesian optimization is widely used for material design by optimizing several experimental parameters [2][3]. We expect that by using this method, we can easily find the optimized experimental parameters to obtain the best film quality as well as the TFT performance.

5.3 References

[1] Y. Chen, Y. Lu, X. Yang, S. Li, K. Li, X. Chen, Z. Xu, J. Zang, and C. Shan, "Bandgap engineering of Gallium oxides by crystalline disorder," *Mater. Today Phys.*, vol. 18, p. 100369, 2021, doi: 10.1016/j.mtphys.2021.100369.

[2] A. Talapatra, S. Boluki, T. Duong, X. Qian, E. Dougherty, and R. Arroyave, "Autonomous efficient experiment design for materials discovery with Bayesian model averaging", *Phys. Rev. Materials* 2, 113803, 2018, doi: 10.1103/PhysRevMaterials.2.113803.

[3] S. Harada, M. Uenuma, T. Miyao, and Y. Uraoka, "Bayesian optimization of PECVD process for SiO_2/GaN interface", presented at IMFEDK 2021.

Research Achievements

List of Publication

A. Academic Journals

1. **<u>Diki Purnawati</u>**, Juan Paolo Bermundo, and Yukiharu Uraoka, "Impact of Precursor Aging and Relative Humidity on the Electric Performance of Solution-deposited Amorphous Gallium Oxide Thin Film Transistors", *(In Preparation)*.

2. **<u>Diki Purnawati</u>**, Paul Rossener Regonia, Juan Paolo Bermundo, Kazushi Ikeda, and Yukiharu Uraoka, "Machine-learned Fermi level prediction of solution processed Ultra-wide Bandgap amorphous Gallium Oxide (a-Ga_2O_x)," *(Under Review)*.

3. **<u>Diki Purnawati</u>**, Juan Paolo Bermundo, and Yukiharu Uraoka, "Insulator-to-Semiconductor Conversion of Solution-processed Ultra-wide Bandgap Amorphous Gallium Oxide via Hydrogen Annealing," *Appl. Phys. Express*, **15 (2)**, 024003 (2022). (Selected as Spotlight in APEX Journal).

B. Peer-reviewed conference proceedings

1. **<u>Diki Purnawati</u>**, Paul Rossener Regonia, Juan Paolo Bermundo, Kazushi Ikeda, and Yukiharu Uraoka, "Fermi Level Prediction of Solution-processed Ultra-wide Bandgap a-Ga_2O_x *via* Supervised Machine Learning Models", *SID Symposium Digest of Technical Papers*, **53 (1)**, 369 – 372 (2022).

2. **<u>Diki Purnawati</u>**, Juan Paolo Bermundo, Yasuaki Ishikawa, and Yukiharu Uraoka, "Photo-assisted Processing of Amorphous Gallium Oxide Thin Film for Flexible and Transparent Device Application", *2022 27th International workshop on Active-Matrix Flat Panel Displays and Devices (AM-FPD)*, 131 – 132 (2020).

Research Grant

1. Grant-in-Aid for PhD Students – Nara Institute of Science and Technology

Presented Works

A. Presentations at international conference

1. **Diki Purnawati**, Juan Paolo Bermundo, and Yukiharu Uraoka, "Impact of Precursor Aging and Relative Humidity on the Electric Performance of Solution-deposited Amorphous Gallium Oxide Thin Film Transistors", The 22nd International Meeting on Information Display, Aug. 23 – 26, 2022 (Virtual)

2. **Diki Purnawati**, Paul Rossenser Regonia, Juan Paolo Bermundo, Kazushi Ikeda, and Yukiharu Uraoka, "Fermi Level Prediction of Solution-processed Ultra-wide Bandgap Amorphous Gallium Oxide *via* Supervised Machine Learning", SID Display Week 2022, May. 8 – 13/ 2022 (Virtual).

3. **Diki Purnawati**, Juan Polo Bermundo, and Yukiharu Uraoka, "Insulator-to-Semiconductor Conversion of Solution-processed Amorphous Gallium Oxide Insulator to Semiconductor through Hydrogen Incorporation", The 21st International Meeting on Information Display, Aug. 25 – 27, 2022 (Virtual).

B. Presentation at domestic conference

1. **Diki Purnawati**, Paul Rossener Regonia, Juan Paolo Bermundo, Kazushi Ikeda, and Yukiharu Uraoka, "Fermi Level Prediction of Solution-processed Ultra-wide Bandgap Amorphous Gallium Oxide *via* Supervised Machine Learning", The 69th Japan Society of Applied Physics Spring Meeting, March 22 – 26, 2022, Aoyama Gakuin Sagamihara Campus, Sagamihara, Japan.

2. **Diki Purnawati**, Juan Polo Bermundo, and Yukiharu Uraoka, "Conversion of Solution-processed Amorphous Gallium Oxide Thin Film Transistor through Hydrogen Annealing", The 82nd Japan Society of Applied Physics Autumn Meeting, Sept. 19 – 23, 2021 (Virtual).

Acknowledgements

Accomplishing doctoral degree is never easy and never done alone. I never lose hope of believing in Allah and the Qur'an as my life pathway. Once Allah said, *"Allah will raise those who have believed among you and those who were given* ***knowledge****, by degrees. And Allah is Acquainted with what you do"* [QS 58:11]. Raise degree of who were given knowledge in contextual, textual, and even philosophical meaning. I would rather love the philosophical meaning, where I have grown through the learning process during my doctoral degree. When I learn how to deal with failure, and how to stand and be confident in myself.

Hereinafter, I would like to express my sincere gratitude to Prof. Yukiharu Uraoka for giving me the opportunity to continue my graduate studies in Information Device Science Laboratory. I am thankful for the kind encouragement, patience, understanding, continuous support, and trust.

I am also very thankful to Assist. Prof. Juan Paolo Soria Bermundo, who has been a great mentor for the past three years. I have received valuable comments and points that helped me improve in a lot of aspects as a researcher. I am also thankful for the patience, understanding, and support at my lowest point when I dealing with failure.

I would also like to thank Prof. Yasuaki Ishikawa, Assist. Mami Fujii, and Assoc. Prof. Mutsunori Uenuma for their constructive criticisms and helpful comments and suggestions which assisted me in understanding more clearly the research I have been doing.

I am thankful for my advisors, Prof. Kazushi Ikeda, Prof. Hiroharu Ajiro, and Assoc. Prof. Tomoyuki Miyao, for sharing their expertise and for the meaningful discussions which helped me in my analyses and in improving my dissertation.

I am also thankful for Assist. Prof. Michael Paul Aquisay Jallorina for being my mentor, big brother, and friend as well. I am thankful for his support and meaningful insight which helped me in understanding live and research.

I am thankful for Dr. Paul Rossener Regonia for being my data science mentor and collaborator which assisted me in understanding the machine learning part in my research. I am thankful for his patience and understanding in assisting me.

I also want to express my appreciation to the intelligent and considerate technical staff of Division of Material Science, Mr. Yasuo Okajima, Mr. Shouhei Katao, Mr. Noritake Koike,

Mr. Kazuhiro Miyake, and Mr. Masahiro Fujihara, and of a Information Device Science Laboratory, Mr. Akio Watakabe, Mr. Hirotoshi Kawahira, Ms. Ryoko Miyanaga, and Ms. Sachiyo Aoyagi, for being patient in trainings and in consultations which greatly helped me finish all that was needed for my research.

I am also thankful to Ms. Yukiko Morita for being accommodating, approachable, and flexible with my research and student demands. Her thoughtfulness has helped me a lot during my stay in Japan. I am thankful for her kindness as a mother and friend as well.

I would also like to thank the former and current members of the TFT group, Ms. Arisa Nishibu, Mr. Takanori Takahashi, Mr. Kohei Fujimoto, Ms. Ployrung Kesorn, Mr. Muhammad Arif Razali, Ms. Dianne Cabrejas Corsino, Ms. Aimi Syairah Safaruddin, Ms. Umu Hanifah, Ms. Candell Grace Quino, Mr. Shunsuke Omae, Mr. Tomohito Tsutsui, Mr. Satoshi Takayama, Mr. Ando Taisei, Mr. Pongsakorn Sihapitak, Ms. Dian Kastian, Mr. Chuanjun Wu, and Mr. Rikuto Sasai, for the enlightening research discussions during trainings and meetings.

I would also like to acknowledge the Indonesian community in NAIST (NAISTER), specifically Dr. Liliany Noviyanty Pamasi for being my big sister and mentor who helped me a lot during my stay in Japan. As beautiful as her name, Kak Lily is an awesome ‘present’ that God sent to me.

Finally, I would like to express my special gratitude to my parents, brother, sister, and to my beloved one dr. Lucky, for their encouragement, understanding, love and support.

August, 2022

Diki Purnawati